UNIVERSITÀ DELLA CALABRIA

UNIVERSITA' DELLA CALABRIA

Dipartimento di Fisica

Dottorato di Ricerca in

Scienze e Tecnologie Fisiche, Chimiche e dei Materiali

CICLO

XXX

Development of new sensor technologies for ambient Mercury and comparison with conventional methods/systems

Settore Scientifico Disciplinare Chimica

CHIM/12 Chimica dell'ambiente e dei beni culturali

Coordinatore: Ch.mo Prof. Vincenzo Carbone

Firma Vincenzo Carbone

Supervisori: Ch.mo Prof. Vincenzo Carbone

Firma Vincenzo Carbone

Dott.ssa Francesca Sprovieri

Firma Francesca Sprovieri

Dottoranda: Dott.ssa Jessica Castagna

Firma Jessica Castagna

"Our greatest weakness lies in giving up. The most certain way to succeed is always to try just one more time."
Thomas Alva Edison

Sommario

Negli ultimi decenni l'ecosistema globale risulta essere sempre più minacciato da problematiche legate sia ai cambiamenti climatici che all'inquinamento atmosferico a causa del massiccio incremento di emissioni inquinanti che stanno alterando l'equilibrio dei gas atmosferici. In tale contesto il Mercurio (Hg) ricopre un ruolo significativo per la sua tossicità e le ripercussioni negative su ambiente e salute. L'Hg viene immesso in atmosfera da una varietà di sorgenti puntuali e diffuse, di origine sia naturale che antropica, per poi essere ridistribuito verso recettori terrestri ed acquatici attraverso un complesso ciclo biogeochimico che coinvolge tutti i comparti naturali quali l'atmosfera, l'idrosfera e la geosfera. Sebbene siano stati compiuti molti progressi, l'attuale conoscenza sui diversi processi chiave che influenzano il ciclo dell'Hg in ambiente, come i processi chimico-fisici che influenzano la mobilità dell'Hg in terreni e sedimenti, o lo scambio di Hg gassoso all'interfaccia aria-acqua, risulta essere non completa né per una descrizione quantitativa, né per una corretta modellazione. Il ciclo cui è sottoposto l'Hg ha inoltre carattere transfrontaliero e pertanto il controllo dei processi che lo caratterizzano ha richiesto negli ultimi anni sforzi congiunti a livello globale, confluiti solo di recente nella Convenzione Internazionale di Minamata che tra gli obiettivi principali propone una riduzione drastica delle emissioni di Hg. A supporto di tale convenzione e al fine di studiare al meglio il ciclo del Mercurio, oltre che per colmare la mancanza di dati in aree del globo dove essi risultano tuttora scarsi o del tutto assenti, nel 2010 è stato promosso il Progetto europeo GMOS - Global Mercury Observation System (FP7). Tale progetto, coordinato

dalla UOS di Rende del CNR-IIA, ha supportato lo sviluppo di una rete di monitoraggio per il Mercurio comprensiva di 40 stazioni a terra finalizzate al campionamento in continuo del Mercurio in atmosfera e nelle deposizioni. In aggiunta e ad integrazione di tali osservazioni su terra ferma il progetto ha previsto specifiche esplorazioni effettuate nel corso di adeguate campagne oceanografiche e voli opportunamente svoltesi in mare aperto e nell'alta troposfera.
In tale contesto è stato sviluppato il presente lavoro di dottorato di ricerca la cui prima parte è stata volta alla comprensione di alcuni processi legati all'Hg attraverso due diversi e specifici casi studio: il primo relativo ad una stazione di monitoraggio inclusa nella rete GMOS e ubicata a Bariloche (Argentina); il secondo relativo ad una campagna oceanografica effettuata, a bordo della nave di ricerca "Minerva Uno" del CNR, nel bacino del Mar Mediterraneo.
In entrambi i casi studio sono stati impiegati sistemi convenzionali di misura per l'Hg, in accordo con la strumentazione di riferimento attualmente impiegata all'interno della rete globale di osservazione per la determinazione di Hg in aria ambiente. Si è tuttavia osservato che tale tipo di strumentazione presenta costi di gestione estremamente elevati e il suo impiego non sempre risulta agevole, soprattutto nelle regioni remote. Le suddette difficoltà hanno pertanto fatto nascere l'esigenza di sviluppare tecnologie e nuovi sistemi di rilevamento per la misura di Hg a costi operativi inferiori e auspicabilmente caratterizzati da robustezza, facile rintracciabilità, indipendenza da forniture significative di gas o di energia oltre che da semplicità nell'impiego. Con tali premesse, la seconda parte della presente tesi di dottorato, si è posta come obiettivo generale lo sviluppo di nuovi sensori per il monitoraggio dell'Hg, sia in aria che nelle deposizioni umide.
Per l'Hg in aria si è preso parte allo sviluppo di campionatori passivi Hg, testati dapprima nei laboratori CNR-IIA, e successivamente sperimentati su campo, nel corso di due campagne di misura stagionali effettuate in cinque siti di monitoraggio GMOS, di cui tre nell'emisfero settentrionale (Italia, Russia e Cina) e due nell'emisfero meridionale (Argentina e Sudafrica). I risultati preliminari di comparazione tra i nuovi sistemi passivi e quelli attivi convenzionalmente impiegati nelle

reti regionali e globali sebbene abbiano evidenziato alcuni problemi, sembrano tuttavia essere abbastanza promettenti.
Per la messa a punto di nuovi sensori per Hg in deposizioni umide, è stato approfondito il principio di funzionamento che si basa sulla spettroscopia ad impedenza elettrochimica di una cella a tre elettrodi che è stata poi opportunamente funzionalizzata per renderla sensibile alle misurazioni di proprio interesse. L'analisi di quest'ultimo tipo di sensore è stata svolta tramite soli test di laboratorio che hanno mostrato una adeguata risposta.
Attraverso lo studio di ricerca effettuato nel corso del dottorato si è avuto pertanto modo di approfondire i processi fisico-chimici dell'Hg arricchendoli con le risultanze dei due specifici casi studio qui presentati. Inoltre, si è avuto modo di partecipare allo sviluppo di sensori di nuova generazione, che ad oggi rappresentano un punto di partenza ottimale per il monitoraggio dell'Hg, sia in aria che nelle deposizioni. Il loro impiego consentirà facilmente di misurare l'Hg in più aree del globo, comprese quelle remote, riuscendo così a fornire un quadro più dettagliato ed esaustivo sulla conoscenza del ciclo del Mercurio.

Summary

In the last decades, the global ecosystem has been increasingly threatened by problems, like as, climate change and air pollution, due to the increasing of pollutant emissions that are altering the balance of atmospheric gases. Among the pollutants, Mercury (Hg) plays a significant role due to its toxicity and negative consequences about the environmental and human health. Hg is released in the atmosphere through punctual or diffuse sources, which could be of natural and/or anthropogenic origins. In the atmosphere, Hg could be redistributed towards terrestrial or aquatic receptors, through a complex biogeochemical cycle that involves all natural areas such as the atmosphere, hydrosphere, and geosphere. Although the Hg's knowledge is improving, the current comprehension about several processes that influence the Hg cycle in the environment, such as chemical-physical processes that affect the mobility of Hg in soils and sediments, or the exchange of Hg gaseous to the air-water interface, is incomplete for both a quantitative description and a proper modeling. The Hg cycle is cross-border, therefore, in recent years, the need to control its processes persuaded to join efforts at a global level. The principal result of the international policies is represented by the Minamata International Convention, of which, its main objective proposes is to reduce drastically the Hg emissions. In 2010, the European Project GMOS - Global Mercury Observation System (FP7) has been approved, in order to support the Minamata Convention, as well as, to examine in deep the Hg cycle, improving the data coverage around the globe, especially in areas where datasets were absent or scarce. The GMOS-Project, coordinated by the UOS

of Rende of the CNR-IIA, supported the development of a monitoring network for Hg, with 40 ground-based stations that have to monitor in continuous Hg in the atmosphere and in depositions. Moreover, within the GMOS-project, oceanographic campaign and aircraft measurements, exploring respectively the open sea and the troposphere, had been performed.
In this context, the following work of PhD research had been developed. The first part of this work concerned with the comprehension of some Hg processes through two different case-studies: the first regarding the monitoring station of GMOS-network set in Bariloche (Argentina), while the second one, was about the oceanographic campaign, performed on board the research vessel "Minerva Uno" of the CNR, into the basin of the Mediterranean Sea.
In both the case-studies, the conventional systems for Hg measurements were employed, according to the reference instruments used within the global network. However, these instruments require an excessive cost of maintenance, and present difficulties in using, especially in pristine areas. These are the motivations of the need of development of new technologies and systems for Hg, which should be cheaper, robust, transportable, with no energy supply, and user-friendly. For this reasons, the main objective proposal of the second part of this PhD thesis is the development of new sensors for the Hg monitoring in the air and wet deposition.
Regard the Hg in air, I was involved into the development of passives samples, tested first into laboratories, and then, on field during two seasonal campaigns, performed in five monitoring GMOS stations, three in the Northern Hemisphere (Italy, Russia, China), and two in the Southern Hemisphere (Argentina and South Africa). The preliminary results of comparison between the new passive system and the active conventional system, although have shown some problems, seem to be very promising.
To develop new sensors for Hg in wet deposition, the Electrochemical Impedance Spectroscopy (EIS) of a functionalized gold three-electrode has been investigated. The analysis of this sensor, performed in laboratories, showed a good response.

The work of research carried out during the PhD has allowed examining in deep the chemical-physical processes for Hg thanks to the results of the two case studies treated. Furthermore, I was involved into the development of new sensors, which could represent a good start point for the Hg monitoring, in both air and wet deposition. The employment of new sensors will allow measuring Hg over the whole globe, including the pristine areas, and will provide an improvement of Hg cycle's knowledge.

Acknowledgements

I would like to express my deep gratitude to Prof. Vincenzo Carbone, Coordinator of the PhD course and relator of this thesis, and to Prof. Ing. Nicola Pirrone, Director of the CNR-IIA, to have given me the opportunity to live this unique experience of formation that enriched my cultural baggage about both the scientific knowledge and the human relationships, allowing my growth first as a researcher, as well as a person.
Moreover, I am thankful to my supervisor, Dr. Francesca Sprovieri, which has judiciously managed my research course, involving me in various activities that were different for contents and approaches, which extended from the data analysis, the laboratory research, until the measurements campaigns on-field.
A great thankfulness is for Dr. Ing. Mariantonia Bencardino, my inexhaustible source of passion for research, which has continuously offered me new ideas for work, and moral support in our moments of negative results.
Furthermore, I would give thanks many tireless CNR-IIA technicians that have taught me all that I know about the instruments, but especially Valentino Mannarino that supported my work requests continuing to attempt also when things didn't go, Giulio Esposito for his endless patience showed in teaching and in the management of unforeseens, and Stefano Dalla Torre for his availability.
A further thank is for all the team about sensors of the CNR-IIA in Rome, first of all, the leader Dr. Antonella Macagnano, following Dr. Andrea Bearzotti, Dr. Emiliano Zampetti, Dr. Paolo Papa, and Dr.

Viviana Perri, for the pleasant reception showed during the my involvement in their activities about the development of sensors for Hg in air, and the Dr. Roberto Pilloton that has followed me during the research about the development of sensors for Hg in wet deposition.
Finally, I would like to thank everyone that gratuitously helped me during my activities with suggests and solutions, like as, Dr. Francesco De Simone, Dr. Ing. Francesco D'Amore, and all other colleagues, and everyone of the research team and of the crew of the two oceanographic campaigns.

Contents

List of Tables

List of Figures

Introduction

Mercury (Hg) is a troubling global pollutant due to its toxicity, which can cause damages to both human health and ecosystems. To deal with these problem, in the last decades the scientific community and the policymakers had been focused on the Hg monitoring, in the area where data are limited or do not exist, as well as on the Hg investigation to gain an in depth knowledge on Hg chemical transformation, processes, and source emissions. In order to limit the Hg negative impact on the global environment, the main address by policymakers had been to cut the Hg emissions by the anthropogenic activities, even if Hg is also emitted from both natural sources. Among the natural sources, there is the Hg amount present in the terrestrial crust in the Cinnabar form (HgS), its emissions from wildfires, volcanic eruptions, and its release from water basins (lakes, seas, and oceans). In addition, the anthropogenic activities, such as coal combustion, could release significant amounts of Hg. The most famous case of Hg poisoning was the "Minamata Disaster" in Japan, where an industry released Hg into the bay, reaching a very high concentration of Hg in water. Entered in water, Hg could bioaccumulate into fishes and biomagnificate through the food web. Fishes are consumed as food by also other animals and people, hence they could poison them. The case of Minamata Disaster caused the death or health problems for thousands of people.
In 2010, a Global Monitoring Network was created within an European Project, the Global Mercury Observation System (GMOS), coordinated by the UOS of Rende of the CNR-IIA. The GMOS Network, made of 40 ground-based stations, plus *ad-hoc* oceanographic

campaigns and aircraft measurements, is providing additional Hg data and key information in filling the actual gaps in the Hg knowledge. In this thesis work, two different case-studies were conducted: the first at the ground-based station in Bariloche (Argentina); and the second one during an oceanographic campaign.
The actual conventional systems to reveal Hg in air show expensive costs of maintenance, high energy supply, and highly qualified technicians. These problems represent an obstacle for the monitoring in remote areas, such as polar regions, remote islands, or high summits. In this regard, the scientific community is working toward the development of new technologies or sensors for the Hg monitoring. Although the sensors will be less accurate than the actual analyzers, they will be favorable since they will be at low cost, transportable and user-friendly. These needs are the motivations for which, in my research work, I studied and developed new sensors for Hg monitoring both in air and in wet deposition.
My PhD thesis consists of 8 chapters.
In Chapter 1, I reported an in deep discussion on the species of Mercury in air and its sources, both natural and anthropogenic. Moreover, I dealt on the chemical proprieties of Mercury and its processes of oxidation and reduction. Finally, I discussed the gaps of knowledge about Mercury's species, the amounts of emissions from the several sources, and its processes of transformation.
In Chapter 2, I presented the need to constitute a global network with the comparable conventional systems to give a homogeneous spatial recovering and a comparable dataset from different monitoring stations. In addition, I dealt with the acquisition as well as with the quality assurance and control (QA/QC) system of Hg monitoring data, which was implemented to support the identification of errors in the measurement systems, and hence, the invalid data.
In Chapter 3, I reported a case-study of Mercury monitored in a ground-based station set in Bariloche, Patagonia (Argentina). The study of the GEM dataset recorded from 2012 until 2016, represent the first investigation of Mercury in Patagonia. A discussion about

the levels of GEM and its seasonal and daily patterns has been conducted. Sources of GEM, thanks to the Backward Trajectory Analysis, have been also investigated.
In Chapter 4, I reported a case-study of Mercury recorded during an oceanographic campaign performed in the Mediterranean Sea in 2015. The Mercury behavior in light of other chemical parameters, such as O_3, NO_x, and SO_2, has been analyzed to identify five events encountered during the route. The events regarded both natural and anthropogenic sources.
In Chapter 5, I discussed the operation of the passive dispositives developed in the CNR-IIA lab. The Passive Air Samplers (PASs) were based on an absorbing material of nanofibers of titanium oxide functionalized with gold nanoparticles. I reported the results obtained in the laboratory.
In Chapter 6, I reported discussion about the comparison between the Hg conventional systems and those ones (PASs) developed in our lab. The comparison was conducted on two seasonal campaigns performed in 5 GMOS sites: Mount Curcio (Italy), Mount Ailao (Cina), Listvyanka (Russia), Bariloche (Argentina), and Cape Point (South Africa). I performed some statistical analysis in relation to the validity of the new technologies proposed.
In Chapter 7, I described the development of new sensors for Hg in wet deposition. Two different functionalized systems, which were sensitive to Hg, have been proposed. The first system was Poly-Thymine based, while the second one was Limonene-based.
Finally, in Chapter 8, I discussed the principal key findings obtained during the research work, including the analysis of cases-studies on Mercury, as well as the results of the sensors developed. Moreover, I suggested the future potential investigations for the research on Mercury, especially that regarding the further validation of the new sensors.

Chapter 1

Mercury: chemical-physical characteristics and processes

1.1 Mercury as Global Pollutant and International Actions

Mercury is a global pollutant concern due to its toxicity and its transport and deposition mechanisms to terrestrial and aquatic receptors, but especially for its chemical transformations of elemental mercury to more toxic species (i.e., methylmercury) and for the bioaccumulation of mercury in the aquatic food web (Nriagu et al. [1988], Iverfeldt [1991], Mason et al. [1994], Pirrone et al. [1996, 2001], Schroeder and Munthe [1998]). Moreover, mercury is characterized by a high ability to distribute globally via the atmosphere. In the last years, both the scientific and political communities are focusing on the need for a global perspective in research, monitoring and policy making. Therefore, since 2002, several initiatives, aimed to reduce the impact of mercury pollution on the environment and human health, have been taking place at national and international levels (une [a]). In 2005, the United Nations Environment Programme - Global Partnership for Mercury Air Transport and Fate Research (UNEP-MFTP) was adopted to better understand the processes of emissions and transport, deposition, and

evasion from terrestrial and aquatic ecosystems. Furthermore, several international Programs and Conventions, such as the UNEP Mercury Program, the Minamata Convention, and the United Nation Economic Commission for Europe - Long-Range Transboundary Air Pollution (UNECE-LRTAP), as well as, on-going regional networks, like the European Monitoring and Evaluation Programme (EMEP), the Arctic Monitoring and Assessment Programme (AMAP), and the Canadian Atmospheric Mercury Measurement Network (CAMNet), have encouraged the expansion of long-term data coverage around the world. However, to guarantee an adequate protection of human health and environment on global scale, the consideration of coordinated initiatives at global level was necessary. The GEO (Group of Earth Observation)-Task HE-02 "Tracking Pollutants" as part of the work plans (2009-2011 and 2012-2015) aimed to the developing of a global observation system for mercury in addition to that for POPs (Persistent Organic Pollutants) in order to support the overarching goals of Global Earth Observation System of Systems (GEOSS) and the challenges of the above on-going programmes and conventions. The Global Mercury Observation System (GMOS) Project established a global network for Hg, involving more than 40 ground-based stations, plus coordinated *ad-hoc* oceanographic campaigns and aircraft measurements. The goal of the global network for Hg is to increase the availability and quality of Hg information on global scale. Moreover, the network is supporting the Minamata Convention which aims to decrease the Hg emissions. The Minamata Convention was adopted and ratified in 2013 by 50 nations.

1.2 Mercury in the Atmosphere: Sources, Speciation, and Chemistry

Mercury (Hg) is a unique natural metal for its peculiarities. In fact, among the others metals, it shows some anomalies, like as its liquid state at ambient temperature, its boiling point below $650°C$, its characteristic to be quite inert chemically, with a high ionization potential,

and its ability to exist in both the elemental state (Hg^0) and oxidation states of 1 (Hg^+) and 2 (Hg^{2+}). Moreover, it is the unique metal with a high volatility that allows to find it in the gas phase at the elemental state, at ambient temperature and pressure. Hg has two chances to enter the atmosphere, the first is through discharge to natural ecosystems, while the second one is through a direct emission into the air. The release in the air can happen in both forms, elemental and oxidized. Furthermore, the oxidized form implies the Hg contamination close to point sources (Nriagu et al. [1988], Pirrone et al. [1996, 2001, 1998]), while the elemental form is able to travel on global scale during its long lifetime.

1.2.1 Emission Sources

Mercury enters into the environment from both natural and anthropogenic sources. The annual estimations of mercury emission are about 2700 and 2250 tonnes, respectively, for natural sources (volcanoes, surface waters, soil, and vegetation) and industrial sources. If the estimations include the amount of Hg concentration re-emitted from the reserves (ocean and soil), where previously it had been accumulated, the natural emission amounts until 5207 tonnes. The total annual emissions estimated are nearly 7527 tonnes per year, although the calculations are still uncertain (Lindberg et al. [2007], Pirrone et al. [2009]). In nature, mercury is found into the earth crust, where the concentration is about 80 $\mu g kg^{-1}$, and in seawater with a concentration of about 0.3 ngl^{-1} (Fergusson [1990], Jonasson et al. [1970], Gworek et al. [2016]). The main mineral form of mercury is cinnabar (HgS), although there are other minerals in a minor quantity, like as livingstonite ($HgSb_4S_8$) and corderoite ($Hg_3S_2Cl_2$). The richest mine of mercury is in Almadén (Spain), from which, since the Roman Empire, mercury was extracted. Indeed, mercury was used into the gold extraction due to its propriety to form an amalgam with gold. During volcanic emissions, mercury coming from deep geologically enriched deposits get in the atmosphere. However, the contribution of volcanic emission depends largely on the characteristic of each volcano. The estimation is

measured by the Hg/SO_2 ratio that is extremely variable. Moreover, there are Mercury emissions also from calderas, such as, the Phlegrean fields (Pozzuoli, Italy) that show fluxes of mercury, as Hg-S complexes, in the range of 0.9 to 19 $gday^{-1}$ (Ferrara et al. [2000], Bagnato et al. [2011]). The estimation for volcanoes and geothermal activities for Hg release results about 90 $Mgyr^{-1}$ (Mason [2009]), which represents the 2% of the total contribution from natural processes. On the other hand, another way to increase naturally mercury concentration in air is through the forest wildfires, after its previous accumulation in the foliage. The release from the forest or soil depends on the meteorological conditions, on the historical atmospheric deposition and on the type of vegetation and topsoil. Recent studies showed that the emission from the biomass burning on the global scale is estimated nearly 675 Mg (Pirrone et al. [2009]), which represents about 13% of the total contribution from natural sources (Friedli et al. [2003a]). Other sources of re-emission are the water basins, where the flux of evasion depends on the concentration gradient of mercury between the top-water microlayer and air above the surface water, on solar irradiation which is responsible for the photo-reduction of oxidized mercury in the top-water microlayer, and on the temperature of the top-water microlayer and air above the surface water (Pirrone et al. [2003], Pirrone and Mahaffey [2005], Hedgecock et al. [2006]). The principal anthropogenic emissions are due to combustion, such as utility and industrial boilers, hazardous waste combustors, crematories, and manufacturing, as well as, chlor-alkali, cement, batteries, byproduct coke, and refineries, moreover, other sources are agricultural burning, landfills, and mobile sources (epa). The major contribution of anthropogenic mercury emission comes from Asian countries (China, India, etc.), due to industrial activities based mainly on combustion of fossil fuels (especially coal) and to incineration of waste material. Therefore, Asian mercury emission is estimated about 40% of global total, while North America and Europe emissions amount to less than 25%. The Hg species released into the atmosphere depends on the source. In fact, generally, the natural sources emit Hg in its elemental source, while the anthropogenic source could be emitted in all three forms, Hg^0, Hg^{2+}, and Hg(p)

(Particulate Buond Mercury). Moreover, the result of combustion is mainly the emission of GOM. Furthermore, the Hg elemental form can be oxidized in both the phases, gaseous and aqueous, by hydroxyl radicals, ozone, and reactive halogen compounds (Sprovieri et al. [2005b], Hynes et al. [2009]). At reverse, Hg^{2+} can be reduced in the aqueous phase by sulfite, halogen species, and hydroperoxyl radicals (Lin and Pehkonen [1999], Hynes et al. [2009]), as well as, through photochemical reactions and heterogeneous reactions in cloud droplets (Lin and Pehkonen [1997], Seigneur et al. [1994]).

1.2.2 Mercury Speciation

The Mercury present in the environment is subject to physical, chemical and biological processes. Once released to the atmosphere, it can travel on different scales, from local to global, depending on the chemical and physical form. The most abundant form (99 % of total mercury) is the Gaseous Elemental Mercury (GEM or Hg^0) that is relatively inert to chemical reactions, therefore, it has a long atmospheric half-life (0.8 months to 1.7 years Ariya et al. [2015]) and can travel on global scale. The GEM background concentration in the Northern Hemisphere is around 1.5-1.8 ngm^{-3}, a bit higher than the concentration in the Southern Hemisphere that amounts around 0.9-1.5 ngm^{-3} Wängberg et al. [2001], une [a]. Further characteristics of GEM are: a high vapor pressure (0.24 Pa at 25°), insolubility in water (60 μgl^{-1}), and a low deposition velocity (0.05 - 0.01 cms^{-1}) (Mason and Sheu [2002], Sanemasa [1975], Schroeder et al. [1991]). When GEM is oxidized, the new chemical form is called Reactive Gaseous Mercury or Gaseous Oxidized Mercury (RGM, GOM, or Hg^{2+}), which has different principal proprieties. In fact, GOM has a lower vapor pressure, is water soluble (66 gL^{-1}) and has a deposition velocity on the order of 1-5 cms^{-1}. The sum of GEM and GOM is indicated as Total Gaseous Mercury (TGM). GEM and GOM can interact with particulate matter, like as dust, soot, and sea salt aerosol, through mechanisms of sorption and desorption. The Particulate Bound Mercury (PBM or Hg(p)) has a deposition velocity, which is particle size dependent, and

ranges from $0.1 - 1 cms^{-1}$. Both GOM and PBM have a short lifetime (1-7 days) and are transported on a local scale (at about 50 km).
In the following paragraphs, I refers to GEM and GOM in terms of Hg^0 and Hg^{2+}, more appropriate for the discussion of chemical processes.

1.2.3 Chemistry of elemental mercury

Mercury has atomic number equal to 80 (Fig. 1.1), and show itself like a silver liquid at ambient temperature. Its melting temperature

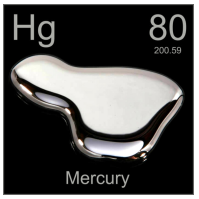

Figure 1.1: Chemical element: Mercury.

is very low, about $-38.83°C$, due to electronic configuration, relativistic effects, and lanthanide contraction. The electronic configuration is $[Xe]4f^{14}5d^{10}6s^2$, where the last orbital, 6s, has two electrons, which is the maximum number of electrons that can have. This configuration obstructs the formation of a Hg-Hg chemical bond because to form it, two electrons have to accommodate in the bonding molecular orbital (σ), while other two electrons have to be in the antibonding molecular orbital (σ^*) (Fig. 1.2). The full antibonding orbital is destabilizing, hence the only possible interaction Hg-Hg are weak. Thanks to the temporary dipole inducted by the fluctuation of electron density, van der Walls interactions have occurred. Furthermore, the bond dissociation energy of Hg-Hg is 8.1 $kJmol^{-1}$. This explanation is not sufficient for the liquid state of Hg, because also other metals have a similar configuration, like as zinc and cadmium, respectively, $[Ar]3d^{10}4s^2$ and $[Kr]4d^{10}5s^2$, but are in a solid state at ambient temperature. The further reason for the liquidity of mercury is the relativistic effect. Due to the very high velocity of electrons moving in 6s orbital ($10^8 ms^{-1}$),

the electron's relativistic mass increases, and as a consequence, there is an orbital contraction. In this way, a bond for electrons in 6s orbital is unfavorable. Finally, there is the lanthanide contraction in the 4f orbital, hence the electrons in this orbital are spread out and the nucleus remains not shielded. Moreover, electrons in 6s orbital are more attracted by the nucleus, and so, are not able to form a bonding.

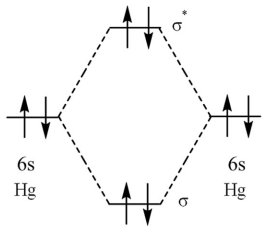

Figure 1.2: Molecular orbital diagram of Hg-Hg.

Formation of amalgam

Since the Empire's Roman is known the ability of Hg to form an amalgam with metals like as alkali metals, Cu, Ag, and especially Au. The alkali metals have only an electron in the orbital ns^1. The bonding Hg-metals is possible because two electrons are in the bonding orbital and one in the antibonding orbital, which makes weaker this bond, but remains stronger than Hg-Hg bond (Fig. 1.3). The type of interaction Hg-metals is the van der Waals, and the bond dissociation energy is less than 13 $kJmol^{-1}$. As a consequence, it is useful to use mercury to extract metals like gold, because, after the formation of amalgam, it is sufficient to apply heat to separate them.

Formation of mercury halides and chalcogenides

Mercury can establish a chemical bond formation with halides (e.g. F, Cl, Br, and I). The type of interaction is depending on the covalent contribution, if there is an overlap of orbitals, and on the ionic contribution, according to the electronegative difference between Hg

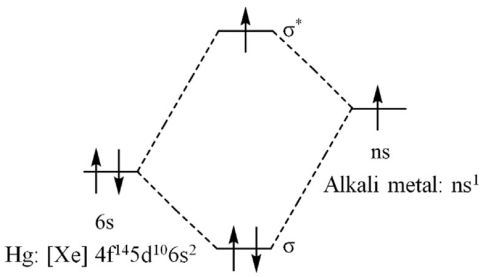

Figure 1.3: Molecular orbital diagram of Hg-metal.

and halide. For example, iodine (I) has more a covalent bonding character because the orbitals, 6s for Hg, and $p\sigma$ for I, are close, while the electronegative difference is little (Fig. 1.4). On the other hand, fluorine (F) is more electronegative, hence, the ionic bond is stronger. Furthermore, chalcogens (O, S, and Se) can establish a chemical bond

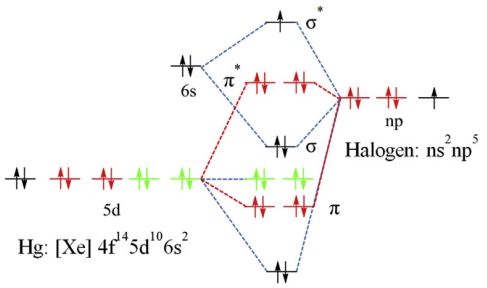

Figure 1.4: Molecular orbital diagram of Hg-halogen.

with Hg. Chalcogens are elements of 16^{th} group with molecular configuration ns^2np^4. Electrons can distribute to originate a singlet or a triplet state. In singlet state, the antibonding orbital is not occupied, hence, the bonding is not destabilized (Fig. 1.5). On the other hand, in the triplet state, an electron is in the antibonding orbital which makes weaker the covalent bonding. The covalent bonding, due to this molecular configuration, is weak also for Hg^0 . In fact, Hg^0 reacts with BrO to produce an unstable molecule, Hg^0 , which will have a fast dissociation.

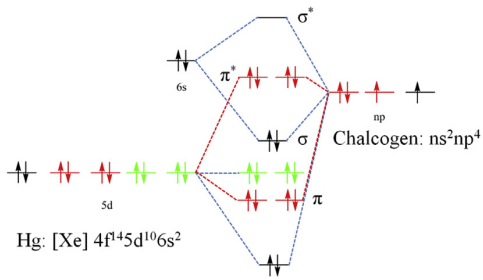

Figure 1.5: Molecular orbital diagram of Hg-chalcogen.

Oxidation processes

Gaseous Elemental Mercury (Hg^0) is involved in oxidation reaction with species like O_3, OH, NO_3, Br, Cl, etc. However, the most important mechanism to oxidize Hg^0 in Hg^{2+} is through reactions with halogen species like Cl_2, Br_2, I_2, but also with atoms of Br and Cl. A possible way to occur the oxidation between Hg^0 and halogen is through the transfer of an electron in 6s orbital of Hg^0 in the p orbital of halogen. This charge transfer can be schematized in the following way:

$$Hg^0 + X \rightarrow Hg^{\delta+} - X^{\delta-}$$

$$Hg^{\delta+} - X^{\delta-} + X \rightarrow HgX_2.$$

At the state of the art, among the halogen species, iodine (I_2) plays a minor role in the Hg^0 oxidation due to the very fast thermal dissociation (at 200 K). In fact, the bonding between I_2 and Hg^0 is very weak, because of the weak interaction involved, like London dispersion forces. Moreover, the rate of oxidation of Hg^0 by I_2 decreases with an increase in temperature. Furthermore, iodine and iodine compounds may indirectly influence Hg^0, because they react with OBr^- and OCl^-, increasing the availability of Br and Cl. Experiments had conducted to investigate the Hg chemical reactions. For the slow reactions, the loss of one reactants in presence of Hg had been monitored, instead, for fast reaction, a laser or flash lamp had been used.

The halogen Cl is believed as one of the main reactants for Hg^0. The reaction involves the three-body recombination of atoms in the following way:

$$Hg^0 + Cl + M \rightarrow HgCl + M$$

The molecule formed is into the energized state (HgCl*). It can release the extra energy through collisions with other molecules, otherwise, it will dissociate to reactants.

$$Hg + Cl \rightarrow HgCl$$

$$HgCl + M \rightarrow HgCl + M$$

The reaction is pressure dependent at low pressures, while becomes independent at high pressure. The efficiency in deactivating HgCl* through collisions increases if increases the number of atoms in the molecules involved. At lower temperature, the rate coefficient will increase, because the reactants motion decreases, and so, less energy has to be removed from the excited state, HgCl*, to the stable molecule HgCl. Further reactions with the excess of Cl atoms and HgCl were supposed (Balabanov and Peterson [2003]).

$$HgCl + Cl \rightarrow HgCl_2$$

$$\rightarrow Hg + Cl_2$$

This secondary reaction could underestimate the rate coefficient calculated during experiments. Moreover, another complication in the calculation of the rate coefficient is the reaction between Cl and O_2.

$$Cl + O_2 + M \leftrightarrow ClO_2 + M$$

$$Cl + ClO_2 \rightarrow Cl_2 + O_2$$

$$\rightarrow 2ClO$$

During the Hg observation in Polar region, it was noted that mercury

depletion is involved with bromine. As a consequence, the Br is believed the most important halogen species for the oxidation of Hg^0, also due to the fast kinetic reaction rate. The reaction proposed for this oxidation is a standard three-body recombination, hence it could be divided into two-steps. During the first step, Hg^0 establish a bonding with Br, producing HgBr. The rate coefficient depends linearly on pressure, while experiments showed a negative dependence on temperature. If the created molecule will be in an excited state (HgBr*), it could release the energy in plus by collisions with other molecules. The rate coefficient calculated was $2.07 \cdot 10^{-12} cm^3 molecule^{-1} s^{-1}$ (Goodsite et al. [2004]). In the second step, HgBr can be dissociated in Hg and Br through thermal energy, or alternatively, and especially at warmer temperatures, it can be oxidized thanks to the action of NO_x and HO_2. Moreover, modeling studies showed that after the first step, in which HgBr is produced, Br does not have a significant role for a further reaction (Martín [2014]).

$$Hg^0 + Br \leftrightarrow HgBr$$

$$HgBr + X \rightarrow HgX_2$$

where X can be NO_2 or HO_2.
BrO was investigated to understand its role in the Hg reactions. The proposed rections are:

$$Hg + BrO \rightarrow HgBr + O, \Delta H^0 = 166 kJmol^{-1}$$

$$\rightarrow HgO + Br, \Delta H^0 = 219 kJmol^{-1}$$

Three experiments were conducted, hence the rate coefficient ranged from $3.0 - 6.4 \cdot 10^{-14} cm^{-3} molecule^{-1} s^{-1}$. An additional difficulty in the calculation of the rate coefficient, is to estimate the Br atoms, which are subject to secondary chemistry.
The reaction between Hg^0 and O_3 had been largely investigated. Experiment performed showed that in presence of ozone, there is a decrease of Hg^0 corresponding to an increase of Hg^{2+} (Hall et al. [1995]). The gas phase rate coefficient was calculated and resulted equal to

$3 \pm 2 \cdot 10^{-20} cm^3 molecule^{-1} s^{-1}$. The rate coefficient increases with temperature, on the other hand it does not depend on relative humidity. Other studies supposed that the reaction with O_3, produced OH radicals that play a role in a secondary chemistry (Pal and Ariya [2004]). The entropy and free energy for HgO were calculated using the bond distance of 1.91 Å. The standard entropy resulted equal to 239.0 $JK^{-1}mol^{-1}$, close to the JANAF value of 239.3 $JK^{-1}mol^{-1}$. On the other hand, the free energy obtained was $\Delta G^0 = 84 kJmol^{-1}$. Using this values, the rate coefficient was calculated, resulting equal to $3.1 \cdot 10^{-4} cm^3 molecule^{-1} s^{-1}$. This value confirmed the rate coefficient estimated by Pal et al. (Pal and Ariya [2004]). Furthermore, this coefficient rate was examined by Seigneur et al. (Seigneur et al. [2006]), deducing that, according to it, the Hg surface concentrations should range between 0.3-1.2 ngm^{-3}, while the half-life of Hg^0 should be reduced from 9 months to approximately 11 days. This conclusions are unrealistic. Ozone is photochemically active, but it does not show strong diurnal variation, although during daylight it increases. On the other hand, GOM shows a diurnal pattern, with a typical increase during the daylight.
Another molecule which seems to react with Hg^0 is OH. The reaction proposed is the following:

$$Hg + OH \rightarrow HgO + H \Delta H^0 = 415 kJmol^{-1}$$

$$Hg + OH + M \leftrightarrow HgOH + M \Delta H^0 = -40 kJmol^{-1}.$$

The binding of HgOH is weak, hence, the calculated binding energy is about 30 or 40 $kJmol^{-1}$ (Tossell [2003], Goodsite et al. [2004]). This weak binding allows a rapid dissociation. According to the binding energy for HgO, reaction with O_2 is energetically favorable.

$$HgOH + O_2 \rightarrow HgO + HO_2 \Delta H^0 = 210 kJmol^{-1}$$

This reaction was investigated by three different experiments. Further reactants for HgOH could be OH (Pal and Ariya [2004]) or a sum of potential molecules, like OH, HO_2, RO, RO_2, NO, NO_2 (Sommar

et al. [2001]).
Finally, just an experiment was conducted on the reaction between NO_3 and Hg.

$$Hg + NO_3 \rightarrow HgO + NO_2, \Delta H^0 = 195 kJmol^{-1}$$

According to the "old" HgO thermochemistry, the exothermicity is of -12 $kJmol^{-1}$, on the other hand, using the "new" thermochemistry, this reaction could be dismissed.

Reduction processes

Hg^{2+} is more water soluble than Hg^0 because it has a lower Henry's constant. Therefore, it could be found in the aqueous - phase of clouds, where it will be reduced mainly through sulfite reduction, photochemical reduction, and reduction by hydroperoxyl radical (HO_2).
During the sulfite reduction, a strong donor- acceptor complex between Hg^{2+} and the sulfite ion SO_3^{2-} is formed. The two electrons of the sulfite ion are transferred to Hg^{2+}, hence it will be reduced to Hg^0 (Van Loon et al. [2000]).

$$Hg^{2+}_{(aq)} + SO_3^{2-} \leftrightarrow HgSO_3 \rightarrow Hg^0_{(aq)} + S(VI)$$

This mechanism does not play a strong role in the reduction (rate constant equal to 0.0106 s^{-1}), due to the short lifetime of sulfite in clouds, which reacts with H_2O_2, O_3, and OH.
The photochemical reaction is based on a ligand-to-metal charge transfer mechanism. The solar radiation brings the Hg^{2+} compound in an excited state, hence, electron from ligand will go into the 6s orbital of Hg^{2+} reducing it to Hg^0. The rate constant for this reaction allows to deduce that it is negligible.

$$Hg(OH)_2 \rightarrow [Hg(OH)]^* \leftrightarrow Hg(OH)_{aq} + OH$$

$$Hg(OH)_{aq} + H^+ + e^- \rightarrow Hg^0 + H_2O$$

Another mechanism of reduction induced photochemically is by dicarboxylic acids, like oxalic, malonic, and succinic acid. The reaction

occurs in two-step: first an organic complex between Hg^{2+} and dicarboxylic acid is formed, and successively the reduction to Hg^0 will occur through the transfer of two electrons.

$$Hg^{2+} + nR(CO_2)_2^{2-} \rightarrow (Hg((OOC)_2R)_n)^{(2-2n)}$$

$$(Hg((OOC)_2R)_n)^{(2-2n)} \rightarrow h\nu HORCO_2H + Hg^0 + CO_2 + (n-1)RCO_2^{2-}$$

Finally, HO_2 seems to be responsible of Hg^{2+} reduction in a two-step reaction. In the first step, it will be reduced to Hg^+ thanks to the reaction with HO_2, successively, in the second step, it reacts newly with HO_2 which will complete the reduction to Hg^0.

$$Hg^{2+} + HO_2^{\cdot} \rightarrow Hg^+ + HO_2^{\cdot} \rightarrow Hg^0$$

1.3 Mercury in Water: Wet Deposition and Air/Sea exchange in the Marine Boundary Layer

1.3.1 Mercury in water

Elemental mercury (Hg^0) can enter into the aquatic systems through wet and dry deposition, where it can be sorbed and desorbed onto suspended particulate matter (SPM) or interact with dissolved organic matter (DOM). Suspended particulate matter includes both organic matter and inorganic particles (clay and hydrous metal oxides), while dissolved organic matter consists of humic substances, carbohydrates, sugars, amino acids, proteins, etc. The binding between Hg^0 and SPM or DOM is the van der Walls interaction. Moreover, Hg^0 seems to interact mainly with SPM than with DOM. When SPM concentration in water increases, Hg^0 in the dissolved phase will decrease due to the sorption of Hg^0 to SPM. The binding between Hg^0 and SPM or DOM is the van der Walls interactions. Once Hg^0 is entered in the aquatic system, it could be subject to chemical and photochemical reactions. Hg^0 oxidized to Hg^{2+}, could participate to methylation. Several mechanisms of oxidative reactions had been investigated. Oxygen

in saline waters oxidizes Hg^0, but this reaction depends on the solar light conditions, hence, the oxidation in the dark was disadvantaged. Other pathways for oxidation involves $\cdot OH$, and $CO_3^{\cdot -}$ radicals and ligand-induced complexation. Hg^{2+} in the aquatic system is reduced through microorganisms, such as algae, cyanobacteria, and diatoms. Furthermore, other reduction processes involve $O_2^{\cdot -}$ radicals and photochemical reaction of DOM. Elemental mercury (Hg^0) in marine environment could become Methylmercury (CH_3Hg^+ or MeHg) through abiotic and biotic processes. The abiotic methylation occurs thanks to methyl iodide (CH_3I) and dimethylsulfide (DMS). The CH_3I is produced by organisms such as cyanobacteria, seaweed, algae, and fungi, while the DMS is produced by marine phytoplankton. On the other hand, the biotic methylation occurs through an anaerobic bacteria, like Desufovibrio desulfuricans ND 132. Methylmercury enters in the food web through fish, which bioaccumulate and biomagnicate it. The bioaccumulation is due to the unability to eliminate methylmercury from the organism. Moreover, the fish food web originates the biomagnification when the bigger fish eats the methylmercury polluted smaller fish. Fishes with high concentrations of MeHg are tuna and swordfish. High concentrations of methylmercury ingested affect the immune system, alter genetic and enzyme systems and damage the nervous system. Moreover, methylmercury is also a teratogen, which means it is particularly damaging to developing embryos, which are 5 to 10 times more sensitive than adults.

1.3.2 Air-sea exchange and dynamic processes in the Marine Boundary layer

The water system, such as oceans and seas, is an important sink for Hg which is deposited by wet and dry deposition. Successively, the Hg accumulated will be released into the air. The Hg evasion from the oceans is greater than the wet and dry deposition, and so, oceans could be regarded as a Hg source. This complex process represents a critical pathway for global Hg cycling. In surface waters, mercury

could be found as elemental (Hg^0) and reactive (Hg^{2+}) state. Hg^{2+} could be in both dissolved phase and attached to particulate matter ($Hg(p)$), wherein this case, the particulate matter is not only detritus but also living species like phytoplankton and zooplankton. The evasion of dissolved gaseous Hg (DGHg), which consists of elemental Hg (Hg^0) and dimethylmercury (DMHg), allows the oxidation in gas phase by hydrogen peroxide (H_2O_2), albeit slowly (Tokos et al. [1998]), the nitrate (NO_3) radical (Sommar et al. [1997]), ozone (O_3) (Hall et al. [1995]), and the hydroxyl (OH) radical (Sommar et al. [2001]). Moreover, the halogen atoms and molecules (Cl, Br, Br_2, Cl_2, Lin and Pehkonen [1999], Sliger et al. [2000], Ariya et al. [2002]) and halogens compounds (e.g., BrCl, BrO) are responsible for the gas phase oxidation. In the Marine Boundary Layer (MBL), the precursors of the reactive halogen species (Br, Cl, BrO, and ClO), such as Br_2, BrCl, and Cl_2, are liberated by sea salt particles (Mozurkewich [1995]). At the state of the art, the Hg flux from water surfaces to air is not clear. It seems strongly dependent on the site. For example, the equatorial Pacific has shown low values of flux (0.7-7 $\mu gm^{-2}mht^{-1}$), while the North and South Atlantic has shown a higher flux (12 and 36 $\mu gm^{-2}mht^{-1}$ respectively).

1.4 Current Uncertainties and Gaps in Our Understanding of Atmospheric Mercury

In the last decades, our understanding of the global atmospheric cycle was improved by research studies. However, the actual knowledge leaves several open questions that the scientists are trying to answer. The most important question regards the nature of the oxidized gas phase mercury, which is collected on KCl-coated denuders. In fact, the Hg compounds that are monitored are not clear. Gaseous Oxidized Mercury (GOM) is operationally defined by the method with which it is sampled. Recent studies demonstrated in fact, that the

principal instrument used until today, the Tekran analyzer, underestimates GOM in some particular environmental conditions, like as high levels of ozone and high relative humidity (Gustin et al. [2016]). Hence, the chemical models have used an incorrect partition of gaseous mercury, between elemental and reactive part. Consequently, the chemical reactions deduced from models could be invalid. Therefore, knowing the precise chemical composition of GOM and/or PBM would immediately allow box, regional and global models chemical mechanisms to be verified and provide impetus to refine rate constants and reaction mechanisms. In addition, the actual modeling applications and related estimates are based on limited long-term time series of data, and from limited areas. There are yet few sites which give long-term mercury data in ambient air and/or precipitation and the existing ones are extremely heterogeneously distributed. While the Northern Hemisphere was supplied by numerous monitoring stations, until the last decade, the Southern Hemisphere was a bit deficient. With the establishment of the GMOS global network this problem is partially solved; however, more ground-based sites, especially in the Southern Hemisphere and tropical areas are needed to better represent different meteorological and geographical conditions. Thanks to the monitoring data, the models could be validated deducing the emissions from different land and water surfaces. In addition, the scarce measurements exploring some processes, like as the wet and dry deposition and/or abiotic and biotic transformations of Hg on the surface and in the water column which represents a big reservoir and source of organic Hg (methylation processes). Further investigations are needed to better evaluate the role of sea spray and formation of Dissolved Gaseous Mercury (DGM) in the top water micro-layer which both drive the gaseous mercury exchange mechanisms at the air-water interface. Although the Minamata Convention recommends the monitoring of the key taxa (i.e. fishes, sea turtles, birds, marine mammals), continuous measurements in time and space are not feasible. However, a biomonitoring program should be designed using bioindicators, time of the year, habitats, and geographic location. Finally, another important problem is lack of a unified and advanced global emission inventory, to allow the models

application for regional and global scale. In the last years, the results of the comparison between the modeled and observed concentrations of Hg are discrepant. The reason for these differences is primarily due to the following gaps: (a) current emission inventories for anthropogenic sources do not account properly for the contribution from biomass burning, artisanal small-scale gold mining, and open coal bed fires, and (b) the uncertainty associated with the estimated contribution from natural sources is still high; very little progress has been made in recent years on understanding the role of climate change in affecting the cycling of mercury between the atmosphere and terrestrial and aquatic compartments.
In conclusion, the scientific community is trying to fill existing gaps in our understanding of the cycle of mercury, such as different chemical and physical mechanisms, as well as, the dynamics of mercury within and between atmospheric, marine and terrestrial ecosystems.

Chapter 2

Monitoring and Analytical Methods

2.1 Mercury Measurements in the framework of the Global Mercury Observation System (GMOS)

To increase the knowledge of the impact of Hg pollution on the environment is essential a long-term monitoring of data of ambient mercury(Hg) on a global scale. In the past two decades, several Hg monitoring sites have been established, especially in the Northerh Hemisphere (i.e. Europe, Canada, USA, and Asia) thanks to the regional networks and/or European projects, such as, "Mediterranean Atmospheric Mercury Cycle System" (MAMCS), "Minamata Convention on Mercury" (MOE), and "Integrated Approach to Assess the Mercury Cycle into the Mediterranean Basin" (MERCYMS). However, due to the global transport of Mercury, international initiatives on global scale were need. Consequently, on November 2010, the Global Mercury Observation System (GMOS) project, funded by the European Commission, started with the proposal to develop a coordinated global observing system to monitor Hg on a global scale. The GMOS Project's

network consists of more than 40 ground-based monitoring stations, distributed globally, and predicts *ad hoc* periodic oceanographic cruises and aircraft measurement in the lower and upper troposphere, as well as, in the lower stratosphere. The monitoring stations' sites had been chosen to obtain a uniform distribution on both hemispheres, and at both high altitude and high sea level locations, as well as in climatically diverse regions. The principal monitoring stations at sea level are: Mace Head (Ireland), Calhau (Cabo Verde), Cape Point (South Africa), Amsterdam Island (southern Indian Ocean). For the high altitude locations, stations such as the Everest-K2 Pyramid station (Nepal) at 5050 m a.s.l. and the Mt. Walinguan (China) stationat 3816 m a.s.l., have been chosen. Finally, the polar areas have been included with Villum Research Station (VRS), Station Nord (Greenland), Pallas (Finland) and Dome Concordia and Dumont d'Urville stations in Antarctica. The monitoring sites are classified as master (M) and secondary (S). The master monitoring stations have to perform the measurements of speciated mercury (GEM, GOM, and PBM), while the secondary stations have to monitorate just the TGM or GEM species. Both the types of stations collect the precipitation samples to measure mercury in wet deposition. Hence, the investigations about meterological influences, long-range atmospheric transport and atmospheric emissions on a global scale, are now possible. Within GMOS, high-quality observations are also guaranteed, in line with international quality assurance/quality control (QA/QC) standards. Moreover, the measurements from these sites have been used to validate regional- and global-scale atmospheric Hg models in order to improve our understanding of global Hg transport, deposition and re-emission, as well as to provide a contribution to future international policy development and implementation (Gencarelli et al. [2017], De Simone et al. [2016]).

2.2 Existing Standard Operating Procedures (SOPs) in Regional and Global Network (GMOS)

During the implementation of the GMOS global network, one of the focal points was the integration and harmonization of the GMOS measurement network with external network to allow the exchange and joint evaluation of data. Integration of GMOS with other existing programs included the arrangement of intercomparisons regarding measurement methods and involved collaboration with the external regional networks. However, one of the overall goals was the development of common protocols regarding how the instruments should be necessarily used and maintained in the field, to assure that measurements from different sites within GMOS and associated networks are comparable. A central part in integrating GMOS with other existing measurement programs was therefore the GMOS Standard Operational Procedures (SOPs). Harmonized Standard Operating Procedures (SOPs) as well as common Quality Assurance/Quality Control (QA/QC) protocols have been developed (Munthe et al. [2011]) according to measurement practices and methods followed within existing regional monitoring networks and based on the most recent literature (Brown et al. [2010], Steffen et al. [2012], Gay et al. [2013]) to achieve a high degree of harmonization. In respect to data collection and management, the worldwide configuration of the GMOS network poses a challenge for Hg scientists because traditional approaches to quality assurance and quality control (QA/QC) are no longer practical when compared with the size of datasets coming from different monitoring stations across the globe, also in near-real time way.

2.2.1 Methods for the determination of TGM and GEM

Within the GMOS, the Standard Operational Procedure (SOP) has been established according to the European standard (NEN-EN 15852

(en)) for TGM and GEM measurements and the Canadian Atmospheric Mercury Measurement Network (CAMNet) / Canadian Air and Precipitation Monitoring Network (CAPMoN) SOP for TGM measurements (sop [c]). It describes the methods, the operating procedure, and the maintenance of instruments, to detect GEM or TGM in air, using the Tekran 2537 or the Lumex RA-915-AM. The Tekran system is based on the Cold Vapor Atomic Fluorescence Spectrometry (CVAFS), while the Lumex system uses the Cold Vapor Atomic Fluorescence Spectrometry (CVAAS), with the Zeeman background corrections. Moreover, it contains quality control protocols to validate TGM and GEM measurements in the field.
GEM/TGM instruments are based on the amalgamation technique. GEM is collected on an adsorbent, a gold surface, from which is successively thermally desorbed and detected by CVAFS or CVAAS, respectively by Tekran or Lumex RA-915-AM. The accuracy of the measurements is due to the automatic or manual calibration with a known amount of Hg^0 vapour. The analytical technique of CVAFS requires pure Ar or He gas during the desorption and the detection step, while CVAAS based instruments could use mercury-free air or nitrogen. The concentrations of instruments are expressed as ngm^{-3} at temperature and pressure standard. Moreover, the instruments measure the temperature and pressure of the sample of air to calculate the concentration at the corresponding standard values.
Both the techniques, CVAFS and CVAAS, are based on the detection of mercury as GEM by UV radiation at 253.7 nm. The fluorescence signal (F) obtained with CVAFS is (after baseline correction) directly proportional to the excitation intensity (I_e) times the concentration of GEM,

$$F \propto I_e C_{Hg^0}.$$

Measurement with CVAAS, requires determination of the total UV-intensity in absence of Hg^0 (I_0) and in the presence of Hg^0 (I),

$$A = ln(\frac{I_0}{I}) \propto C_{Hg^0}.$$

2.2.2 Methods for the determination of speciated Hg (GEM, GOM, and PBM)

The species of Mercury (GEM, GOM, and PBM) are detectable using the Tekran 2537/1130/1135 automated system (Fig. 2.1) (sop [b]). The PBM detected is concerning to the particulate bound mercury less than 2.5 μm. The ambient air is pulled into the Tekran speciation system through a glass elutriator inlet, which removes particulate matter that is $>2.5\mu m$, realizing a laminar flux. The GOM species is collected on the first system, the coated quartz annular denuder (Tekran-1130), while the PBM is collected on the Regenerable Particulate Filter (RPF) (Tekran-1135), leaving to pass the GEM species until the gold cartridges (Tekran-2537). The GEM collection on the two gold traps (A and B) is alternated after 5 minute. Moreover, GEM is thermally desorbed and the UHP argon gas transports it until the detection cell, where it is quantified using CVAFS. After the sampling of the species, GOM and PBM are released thermally respectively at $800°C$ and $500°C$ and are converted into GEM to be directed with a mercury free air stream towards Tekran Model 2537A CVAFS, where it is detected. The sampling time for GOM and PBM is longer than the GEM measurements, which are in continuos. The SOPs proposed by GMOS suggested the using of the sampling time of 5 minutes for GEM and 2 hours for GOM and PBM. However, some exceptions could be accepted according to the difficulties of the stations. The volumetric flow rate through the inlet should be 10 lpm, moreover, the Tekran 2537 should pull at 1 lpm for GEM sampling, while the 1130 pump module, as support for the Tekran 1130 and 1135, pulls at 9 lpm. However, in some atmospheric conditions, such as, low pressure at high altitude, the flow rate could be reduced. The sampling cycle of 2-hour of GEM detection, is followed by a 1-hour desorption cycle in which GOM and $PBM_{2.5}$ are quantified. The 1-hour desorption cycle should be programmed as follows, with each step requiring 5 minutes:

- 3 zero air flushes;
- 1 pyrolyzer heat cycle;

- 3 particulate heat cycles;
- 3 GOM denuder heat cycles;
- 2 zero air flushes (while the furnaces cool).

The concentration of $PBM_{2.5}$ is calculated as the sum of the concentration of the three particulate heat cycles minus 3 times the value of the third zero air flush ark L. Olson and Rhodes, while the concentration of GOM is similarly calculated as the sum of the concentration from the three denuder heat cycles minus 3 times the value of the third zero air flush ark L. Olson and Rhodes.

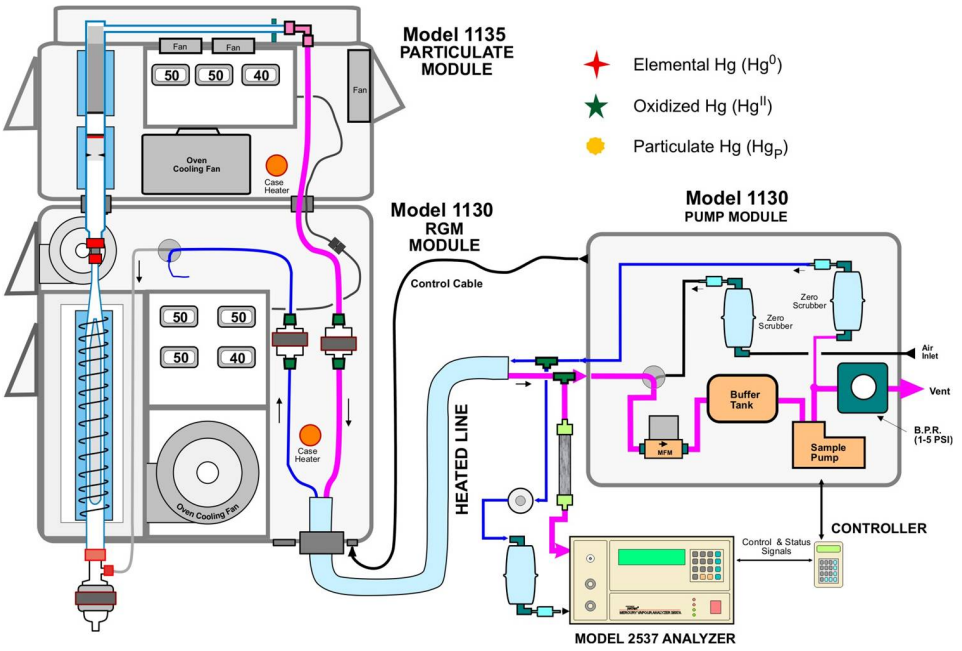

Figure 2.1: Tekran automatic speciated ambient mercury analyzer.

2.2.3 Methods for the determination of Total Hg in Precipitation

Within the GMOS, the Standard Operational Procedure (SOP) has been established also for the determination of total mercury in precipitation using wet-only and/or bulk precipitation collectors (sop [a]). The SOP is based on the standards for the measurement of mercury in precipitation set forth by the European Monitoring and Evaluation Programme (EMEP) and the North American Atmospheric Deposition Program (NADP) Mercury Deposition Network (MDN). The SOP explains the preparation of sampling materials, the collection of sample in the field, and the analysis of samples. However, the GMOS network organized that the preparation of samples and the following analysis should be performed in few laboratories (Istituto sull'InquinamentoAtmosferico (CNR-IIA), the IVL Swedish Environmental Research Institute, and the Institut "Jozef Stefan" (JSI)), while the monitoring stations should occupy of just the collection of precipitation samples. The sampling is performed by the wet-only or bulk collector. Although the wet-only collector is suggested, sometimes its using becomes not easy, like as insufficient power supply, the absence of a regular site operator, and extreme weather conditions, hence the using of the bulk collector is permitted. Wet-only collectors collect only particles and dissolved constituents during precipitations, in fact, they present an automated system with a wetness sensor that open the collector only while the precipitation is occurring. The efficiency of wet-only collection depends on several factors, such as, the wind speed, the type of precipitation (rain or snow), and the aerodynamic properties of the sampler. Moreover, when the collector is opened, it is possible that also some dry particles, non-sedimenting particles, and gases could enter into it. On the other hand, the bulk collector is designed for the collection of wet and dry gases and particles, because it is always open, independently from the precipitation. In this way, the bulk collector captures the total deposition of mercury from the atmosphere. Moreover, with the bulk collector is not possible to distinguish the part of wet deposition from the dry. Additionally, another problem

of the bulk collector may be the Hg volatilization, the adsorption to the walls of the funnel while there is no precipitation, and the contamination with insects, bird droppings or other material in the sampling vessels, especially when using extended sampling periods.
The materials involved into the mercury collection and analysis have to be borosilicate glass or fluorocarbonpolymers. The precipitation collector consists of a cylindrical funnel with a circular horizontal opening of at least 8 - 10 cm inner diameter. Moreover, the funnel has a capillary or vapor lock connected to the bottle to realize the precipitation sampling (Fig. 2.2). The funnel shall should be positionated at least 1.5 m above the ground level to avoid the contamination from heavy rain, and should be housed in a suitable container or cabinet that protects the sample from sunlight and moderates the temperature of the sample, avoiding the evaporation under high temperatures or to freezing during low temperatures. After the sampling, the precipitations are analyzed by using thermal desorption and dual gold trap amalgamation with CVAFS.

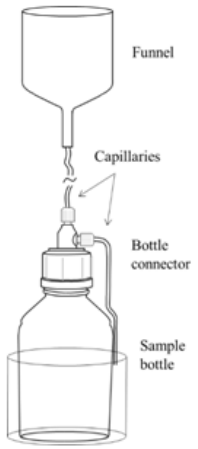

Figure 2.2: Example of a precipitation collector.

2.3 Quality assurance and quality control (QA/QC) procedures

One of the major outcomes of GMOS network has been an interoperable e-infrastructure developed following the Group on Earth Observations (GEO) data sharing and interoperability principles which allows to provide support to UNEP for the implementation of the Minamata Convention (i.e., Article 22 to measure the effectiveness of measures). Within the GMOS network, Hg measurements were harmonized according to the Standard Operating Procedures (SOPs). Moreover, the quality assurance and quality control (QA/QC) have been established and implemented assuring the comparability of data. The acquisition of atmospheric Hg data in near real time is centralized in a online system (termed GMOS Data Quality Management, G-DQM). Successively, they are harmonized by the QA/QC protocol. The quality assurance and control (QA/QC) procedures check some parameters about the calibration, and measurements, for example for Tekran, they check: if the calibration factor (Response Factor) is included in a established range, if the noise of instruments is acceptable, the differences between the signal coming from the couple of traps, if the concentrations appear anomalies, with very high or very low values, the percentage of release of the speciated Hg (GEM, GOM, and PBM) for each step (the main concentration, about 70%, should be released at the first step) et cetera (Cinnirella et al. [2014], D'Amore et al. [2015]).

Chapter 3

Case Study: EMMA Station measurements

3.1 Introduction

Several [1] investigations in different locations of South America (SA) support the idea that Hg may pose a problem at a regional scale (une [b,c]). However, global Hg models have large uncertainties about Hg levels in this region since estimates are mostly extrapolated from regional grouping not always reflecting local situations because measurements or statistical information are not available (AMAP/UNEP [2015], Evers [2016], Kwon and Selin [2016]). In general, in some countries of SA Hg pollution has been attributed mostly to sustained artisanal gold mining (Cooke et al. [2009]). However, in pristine remote areas of the region the occurrence of moderate to high Hg levels has been related with 30 eventual inputs from geogenic sources, biomass

[1] Most of the contents of this chapter is extracted by the article: Diéguez, M. C., Garcia, P. E., Bencardino, M., D'Amore, F., Castagna, J., Ribeiro Guevara, S., and Sprovieri, F., "Four years of atmospheric mercury records in Northwestern Patagonia (Argentina): potential sources, concentration patterns and influence of environmental variables observed at the GMOS EMMA (Estaciòn de Monitoreo de Mercurio Atmosfèrico) station ", DOI:10.5194/acp-2016-1076, 2017.

burn and atmospheric transport and deposition (Nriagu and Becker [2003], Ribeiro Guevara et al. [2010], Daga et al. [2014, 2016a,b], Hermanns and Biester [2013a,b], Higueras et al. [2014]). In Patagonia, the southernmost area of SA comprised in the Southern Volcanic Zone (Naranjo and Stern [2004]), there is increasing evidence arising from lake sediment studies reporting high Hg levels corresponding with volcanic events in the region, and also sustained Hg contributions through atmospheric transport and deposition (Ribeiro Guevara et al. [2010], Hermanns and Biester [2013a,b], Daga et al. [2014, 2016a, 2010]). In particular in Nahuel Huapi National Park (NHNP, Northwestern Patagonia, Argentina), a well-protected natural reserve, several investigations have highlighted the occurrence of Hg in air and freshwater bio-indicators (Guevara et al. [2004a,b]), and moderate to high Hg levels in lake biota (Arribére et al. [2010], Rizzo et al. [2011, 2014]). The presence of high Hg levels in different ecosystem compartments has been attributed alternatively to eventual inputs from several active volcanoes aligned in the Andean stretch and to biomass burn (wild fires) (Ribeiro Guevara et al. [2010], Daga et al. [2016a, 2010, 2016b]). However, the fact that most total dissolved Hg in freshwater ecosystems of the area is in the inorganic form (97%) (Rizzo et al. [2014]), suggests that atmospherically transported Hg and deposition in catchments sustain baseline Hg levels, coinciding with evidence from lake sediment records (Daga et al. [2016a, 2010] and references therein). In contrast with the increasing evidence of Hg occurrence within ecosystem compartments of the Patagonian region, the identification and measurement of the potential sources of Hg, such as precipitation and atmospheric transport, is at its starting point. Until recently, atmospheric Hg levels in the region were derived from point measurements performed in Northwestern Patagonia, reporting a mean GEM concentration of $7.5 \pm 1.4\ ngm^{-3}$ (Higueras et al. [2014]). In 2012, the GMOS EMMA station was established inside Nahuel Huapi National Park, as part of the Global Mercury Observation System (www.gmos.eu), which has expanded the coverage of atmospheric Hg measurements by establishing Hg monitoring stations around the globe and in strategic remote locations of the SH, including different sites in SA (Sprovieri

et al. [2016b,a]). New stations such as the EMMA in Patagonia, are providing insight into the concentrations and patterns of Hg levels in remote regions not previously covered in other networks. In particular, the EMMA station is one of the five GMOS sites spotted in Central and South America and the southernmost Hg monitoring site of the continent, providing novel regional information of Hg levels useful for Hg global models (Sprovieri et al. [2016a], Travnikov et al. [2017]). The present work provides the first continuous records of GEM concentrations measured from October 2012 to May 2016 at the GMOS EMMA station in Northwestern Patagonia. High frequency GEM concentration data recorded under the standard operational procedures of the GMOS project has been analyzed to provide a description and to discuss: i- GEM concentrations and seasonal and daily patterns observed during the sampling period; ii- the influence of local environmental parameters on GEM behavior, and, iii-the potential sources of the atmospheric Hg transported by air masses using backward trajectory analysis.

3.2 Experimental

3.2.1 Site description

The EMMA Station is located at $41°7'43.33"S, 71°25'12.03"O$; 800 m a.s.l, in the central area of the natural reserve Nahuel Huapi National Park (NHNP; $40.145 - 41.592°S$; $71.028 - 71.966°W$) within the lake district of Northwestern Patagonia (Argentina) (Fig. 3.1). The station was established as a GMOS site in 2011 in the field research station of the Photobiology Laboratory (INIBIOMA-CONICET), starting its operation in October 2012. The whole stretch corresponding to North Patagonia is included in Southern Volcanic Zone of the Andean Volcanic Belt (Naranjo and Stern [2004]), including several active volcanoes aligned in the latitudinal range from $33°S$ to $46°S$. NHNP limits at its western side with the active volcanic formation Puyehue Cordón Caulle. In recent years, major eruptions of the volcanoes Chaitén

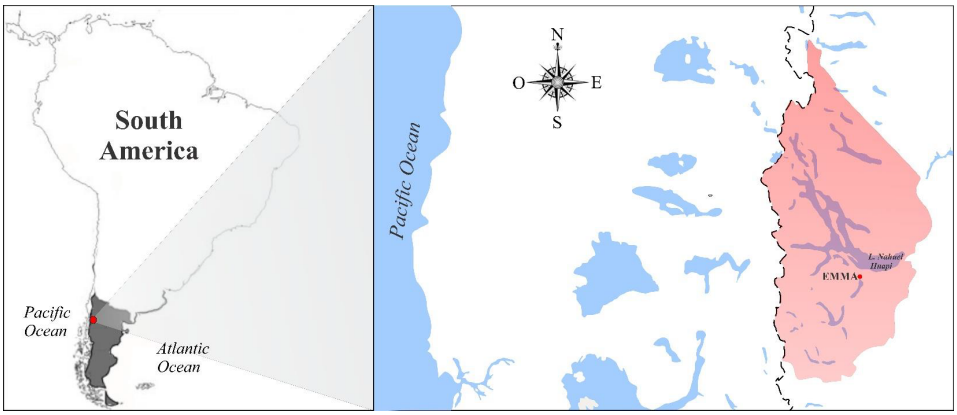

Figure 3.1: Map of Argentina, with EMMA Station.

(2008-2010), Puyehue Cordón Caulle (2011) and Calbuco (2015) impacted the region (Ribeiro Guevara et al. [2010], Daga et al. [2010, 2016b,a]). The climate of North Patagonia is strongly modulated by the presence of the Andes cordillera and has been characterized as cold-temperate with well-defined wet and dry seasons (Paruelo et al. [1998], Rusticucci et al. [2014], Bianchi et al. [2016]). The South Pacific westerly air current carries humid winds from the Pacific Ocean to the continent which discharge their humidity as they pass over the Andes, becoming dry in few kilometers and limiting the Atlantic influence (Garreaud et al. [2013]). Overall, these conditions result in a pronounced climatic contrast between the Pacific side of the Andes and the Atlantic side, and also in areas within the east Andean stretch, characterized as an extremely sharp altitudinal and climatic gradient, affecting particularly precipitation. These extremes are represented in the area of Nahuel Huapi National Park within a longitudinal distance of about 70 km from the cordillera, with and altitudinal decline from about 3000 to 670 m a.s.l and precipitation grading from 3500 mmy^{-1} close to the Andes to 800 mmy^{-1} in the sierra and meseta stretches. Such environmental conditions echo on vegetation which grades from the deciduous and evergreen Nothofagus forests typical of Andean valleys to a shrub-graminous steppe at the lower side in the

sierra and meseta areas (Mermoz et al. [2009]). The Park includes the headwaters of the largest freshwater network of North Patagonia, encompassing high mountain lakes and streams and deep and shallow lakes at the piedmont, most belonging to the Nahuel Huapi catchment (Fig. 3.1). There are three population settlements in the Park on the shores of Lake Nahuel Huapi (557 km^2), San Carlos de Bariloche city (population ca. 115000), and the villages of Dina Huapi (ca. 4000 inhabitants) and Villa La Angostura (ca. 15000 inhabitants). The main economic activity within the Park is tourism which concentrates mostly in winter and summer.

3.2.2 Data acquisition and handling

The meteorological parameters, atmospheric pressure, air temperature, wind speed and direction, dew point, precipitation, and relative humidity were continuously recorded at the EMMA station by an integrated weather station (Davis Vantage Pro) located besides the Hg monitoring instruments. Ancillary meteorological data was uploaded periodically in the GMOS website (G-SDI) (http://www.gmos.eu/sdi). GEM concentrations have been continuously carried out using an automated Hg vapor analyzer Tekran 2537B (Tekran Instrument Corp., Ontario, Canada) located inside a shelter (room temperature $15° \pm 4°C$) which pumps ambient air from the outside through a Teflon sampling line. The detection limit is 0.1 ngm^{-3} at a flow rate of 1 $Lmin^{-1}$. The instrument performs automatic internal permeation source calibrations every 71 hours, and is regularly assisted to secure its performance following the standard operational procedures (SOPs) of the GMOS project (Sprovieri et al., 2016). Routinely, GEM data collected in the EMMA station is logged automatically into a computer using the software Tekcap (Tekran Instrument Corp.) and uploaded manually in the GMOS website. The raw GEM data obtained are then sorted out following the quality assurance and control (QA/QC) procedures in the GMOS data validation application G-DQM (Cinnirella et al. [2014], D'Amore et al. [2015]). All of the in situ measured parameters presented in this work are reported at local time (Bariloche Standard

Time: UTC - 4.00h), and all concentrations refer to STP conditions.

3.2.3 Statistical analysis

The diel pattern of GEM was assessed seasonally, considering the photoperiod (day-light hours) of the mid-season (summer: 07:00-20:30 h; fall: 9:00-18:30 h; winter: 09:00-18:30 h; spring: 07:00-20:30 h) to calculate day and night GEM concentrations between October 2012 and May 2016. The hourly-averaged GEM concentration was also computed for the study period. A multivariate exploratory study including a cluster analysis (CA; Ward's method and correlation as distance measure) and a principal component analysis (PCA; correlation matrices) was performed to determine the most influential meteorological variables relating with GEM concentration, using R framework (version 3.2.2) with packages pvclust (version 2.0-0) for CA and FactoMineR (version 1.31.4) for PCA. The CA is a statistical analysis that assembles a set of objects in some groups having similarities, while the PCA is among the most popular multivariate statistical technique used in order to reduce the dimensionality of data and to search correlation between variables. PCA analyzes data in a matrix arranged per rows: each row contains a different observation while the columns representing the observed variables. The independent variables are, in general, inter-correlated and the goal of PCA is to find a different representation of data using orthogonal variables called principal components. Using this new representation is more straightforward to find the intercorrelation between the original variables.
Two way analysis of variance (2-Way ANOVA) was performed to study the day-night differences in GEM concentrations among seasons, considering again the hourly-averaged value for the complete time series (October 2012-May 2016) and using the software SigmaStat. Post-hoc tests (Holm-Sidak) were performed to study day-time and night-time differences in GEM concentrations patterns among seasons. In order to determine the path of air-masses reaching the EMMA station, the hybrid single-particle Lagrangian integrated trajectory model

(HYSPLIT) available at the NOAA Air Resources Laboratory (Air Resources Laboratory 2010) was used to calculate GEM backward trajectories (BWT) (Draxler and Rolph [2003]). Specifically, the BWT were calculated in correspondence with the highest and the lowest GEM concentrations events, using the READY Website (http://www.arl.noaa.gov/ready.html). Calculations were performed for a total run time of 48 h, setting the start of a new BWT every 2 h, for a total number of 24 trajectories. The Global Data Assimilation (GDAS) set was used as meteorological input. The trajectory arrival height was established at the elevation of the EMMA station, 800 m above ground level, approximately the boundary layer height where pollutants are usually well mixed, thus allowing to discriminate the influence of atmospheric transport from local and regional sources. A label interval of 6 hours was also set.

3.3 Results and discussion

3.3.1 GEM concentration levels and seasonal pattern analysis

Figure 3.2 shows GEM levels from October 2012 to May 2016 with concentration ranging between 0.23 and 1.42 ngm^{-3} with an average of 0.87± 0.15 ngm^{-3}. Table 3.1 reports a statistical summary of GEM concentration for both, the whole sample period as well as for each of the four seasons, calculated from validated GEM observations. The general lack or limited availability of previous observational data of atmospheric Hg for SA and, in particular for Patagonia, hinders a direct comparison of the data obtained during the studied period. In spite of this, however, atmospheric Hg measurements performed at five GMOS sites located in the SH made a first comparison possible. The resulting mean GEM concentration recorded at the EMMA station is within the concentration boundaries reported for the SH (0.84-1.03 ngm^{-3}) (Sprovieri et al. [2010b,a], Slemr et al. [2015], AMAP/UNEP [2015], Angot et al. [2016]). However, they are closer to the mean

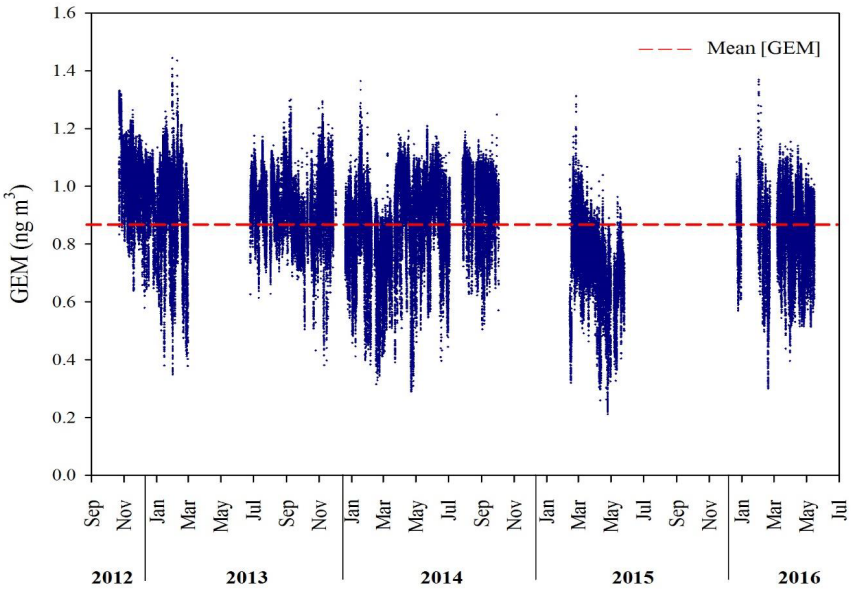

Figure 3.2: Temporal variability of GEM data recorded at the EMMA station.

values recorded at the Antarctic GMOS sites Dumont D'Urville and Concordia Station (Sprovieri et al. [2016b]). In a more general context, the median GEM concentration recorded in Northwestern Patagonia during the studied period (0.87 ngm^{-3}, ranging seasonally between 0.80 and 0.93 ngm^{-3}) falls in the lower extreme of the Northern-Southern Hemispheric gradient computed from records of 2013 and 2014 at GMOS sites. The hemispheric gradient encompasses median GEM concentrations 1.5 ngm^{-3} in the North Hemisphere, 1.2 ngm^{-3} in the Tropics and 0.93-0.97 ngm^{-3} in the South Hemisphere (Sprovieri et al. [2016b]), in line with previously described hemispheric trends (Lindberg et al. [2007], Sommar et al. [2010], Soerensen et al. [2010], Sprovieri et al. [2010b]). The mean GEM concentrations were higher in spring and winter, followed by summer and autumn levels (Table 3.1; Fig. 3.3). Concentration peaks in the hourly averaged GEM

Table 3.1: Statistics of meteorological variables [temperature (t), wind speed (ws), wind direction (wd) and relative humidity (rh)] and GEM concentration recorded at the EMMA Station are reported referring to both the whole data frame (October 23, 2012 - May 15, 2016), as well as to each seasons (Summer, Autumn, Winter and Spring).

Variable		Whole dataframe (2012-2016)	Summer (DJF)	Autumn (MAM)	Winter (JJA)	Spring (SON)
t (°C)	n	25700	7853	8537	4068	5242
	Min	-9.6	-2.4	-4.6	-9.6	-5.8
	1st Q	4.1	8.3	4.7	-0.3	2.9
	Median	8.5	13.4	8.6	2.2	6.7
	Mean	9.6	14.49	9.012	2.25	7.851
	3rd Q	14.2	19.8	12.6	4.8	12.2
	Max	37.7	37.7	33.1	16.2	30
ws (m s-1)	Min	0	0	0	0	0
	1st Q	0	0	0	0	0
	Median	1.6	3.2	1.6	1.6	3.2
	Mean	3.568	4.342	3.018	2.502	4.13
	3rd Q	6.4	6.4	4.8	4.8	8
	Max	22.5	19.3	16.1	22.5	19.3
wd (°)	Direction	315°(NW)	292.5°(WNW)	315°(NW)	315°(NW)	315°(NW)
	Frequency	15387	5080	3546	3279	4254
	Direction	292.5° (WNW)	315°(NW)	292°(WNW)	292°(WNW)	292°(WNW)
	Frequency	13503	4308	3361	2353	2710
rh (%)	Min	12	14	12	27	19
	1st Q	52	46	58	61	47
	Median	64	59	72	69	58
	Mean	64.73	58.9	71.4	71.45	57.4
	3rd Q	78	71	89	84	67
	Max	100	98	100	100	99
GEM (ng m-3)	Min	0.23	0.31	0.23	0.39	0.42
	1st Q	0.77	0.76	0.71	0.85	0.84
	Median	0.87	0.86	0.80	0.93	0.93
	Mean (SD)	0.87 (0.15)	0.86 (0.15)	0.81 (0.15)	0.92 (0.10)	0.93 (0.13)
	3rd Q	0.97	0.96	0.92	1.00	1.01
	Max	1.42	1.42	1.16	1.17	1.31

were recorded at different times of the day; around 11:00 in summer, between 12:00 and 15:00 in autumn, from 11:00 to 13:00 in winter and between 09:00 and 12:00 in spring (Fig. 3.3). Hourly averaged GEM concentrations were significantly higher during day-time (day-time and night-time hours defined by the local photoperiod at mid-season) than at night (ANOVA, F=532.82; p<0.001). This pattern was similar across seasons although the trend was more pronounced in both summer and autumn (F=1017.83; p<0.001; Fig. 3.4). Remarkably, mean day-time GEM concentrations in spring and winter were similarly higher (p>0.05) as compared to the lower mean levels found in summer and even lower in autumn (p<0.05). Night-time GEM concentrations were higher in spring followed by winter, decreasing towards summer and autumn when the lowest mean concentration was recorded (Fig. 3.4).

3.3.2 Meteorological data behavior at the EMMA station

During the study period temperature fluctuated between $-9.6°C$ and $37.7°C$, averaging $9.6°C \pm 7.8°C$. A marked thermal seasonality was observed which reflected in the contrasting mean summer and winter temperatures ($14.5 \pm 7.9°C$ and $2.2 \pm 4.4°C$, respectively) (Table 3.1). The relative humidity showed high values during autumn and winter (71%) compared to spring and summer (58%) (Table 3.1). Wind speed (ws) showed higher values during summer and spring ($4.3 \pm 4.09 ms^{-1}$ and $4.1 \pm 4.5 ms^{-1}$, respectively) (Table 3.1, Fig. 3.3). The predominant winds bring air masses from the Pacific as indicated by the high frequencies showed by the wind records from NW (31°; frequency=15387) and WNW (292.5°; frequency=13503) (Fig. 3.3). In spring, autumn and winter the predominant winds were from the NW, while in summer alternated between WNW (n = 5080) and NW (n=4308) (Fig. 3.3a-e). The NW winds were more frequent in spring and summer compared to autumn and winter, increasing during day-time from around 8:00 h up to 16:00 h to 19:00 h depending on the

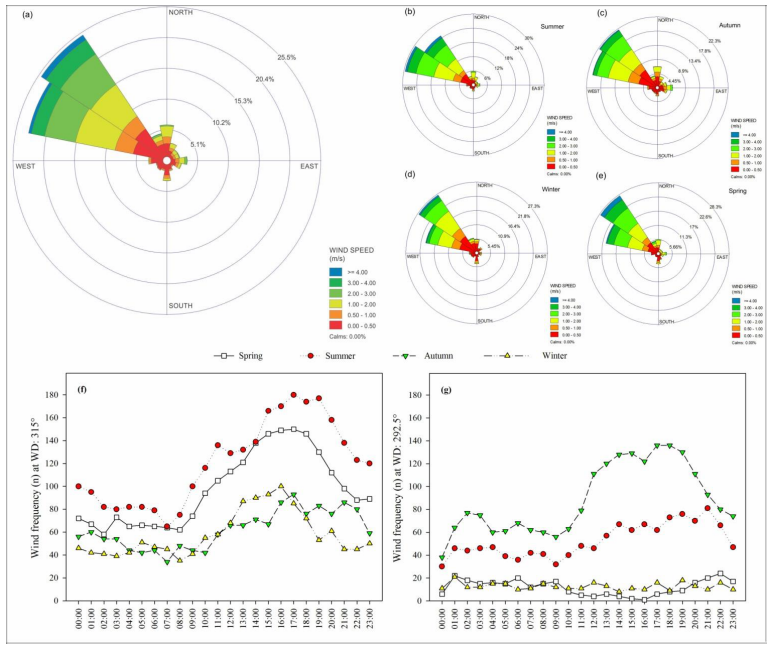

Figure 3.3: Prevailing wind direction at the EMMA Station (Nahuel Huapi National Park, Northwestern Patagonia) calculated as frequency for: a) the whole data frame (October 23, 2012 - May 15, 2016), b) summer, c) autumn, d) winter and, e) spring; f) daily frequency of the prevailing winds on a seasonal basis (315°), and g) daily frequency of the second prevailing winds in a seasonal basis (292.5°).

season and decreasing afterwards (Fig. 3.3f). In contrast, WNW winds were more frequent in summer and autumn, showing higher values around 12:00 and 20:00 h, whereas the influence of this wind direction was similarly low in winter and spring (Fig. 3.3g). The recorded wind pattern at the EMMA station resembles to generalized trends described for Andean Patagonia in the literature (Paruelo et al. [1998], Garreaud et al. [2013], Rusticucci et al. [2014]).

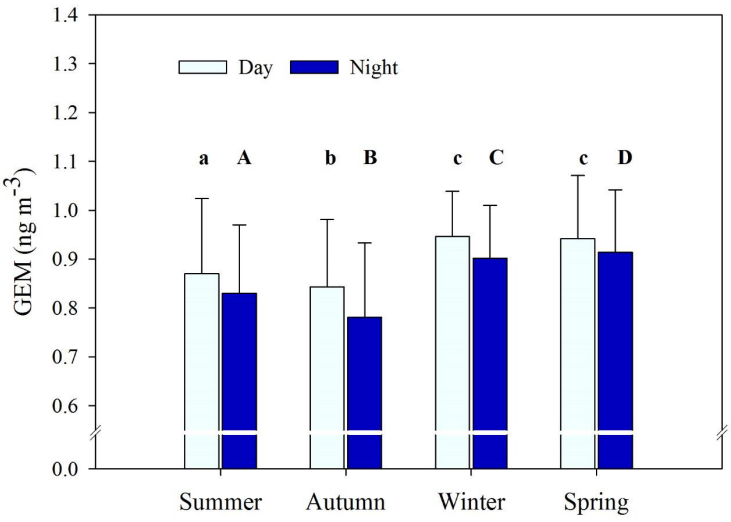

Figure 3.4: Seasonal variability of GEM data recorded at the EMMA station.

Table 3.2: Results of the Principal Component Analysis (PCA) performed to study the relationship between meteorological variables and GEM concentrations trends recorded at the EMMA Station (Nahuel Huapi National Park, Northwestern Patagonia). The values reported in the table are the contributions of the variables (based on correlations) to the main factors/components (Factors 1, 2, 3, Variance explained >15%).

Variable	Factor 1	Factor 2	Factor 3
Temperature	0.805	-0.381	-0.13
Wind speed	0.813	0.206	-0.135
Relative humidity	-0.814	0.33	0.029
Wind direction	0.267	0.821	-0.434
GEM	0.453	0.415	0.783
Variance explained (%)	44.97	22.85	16.73
Cummulative Variance explained (%)	44.97	67.82	84.56

3.3.3 Relationship between meteorological variables and GEM concentrations

The multivariate exploratory analyses performed to study the relationship between the meteorological variables and GEM, pointed out the strong influence of wind direction and, secondarily, of wind speed and temperature on GEM concentration. The cluster analysis (CA) showed four groups of variables, the first including relative humidity, the second with wind direction and GEM, the third grouping wind speed and temperature, and the last group gathering the second and the third ones (Fig. 3.5a). Therefore, it is apparent that wind direction is a driver of GEM concentration, while temperature and wind speed are also influential meteorological variables. The principal component analysis (PCA) performed including the same variables reinforced the pattern revealed by the CA. Two factors accounted to explained 68% of the variance, and the inclusion of a third factor increased the resolution of the model explaining 85% of the variability during the studied period (Fig. 3.5b; Table 3.2). Factor 1, explaining 45% of the variance, denotes the importance of the dispersion process as indicated by the direct contribution of the wind speed and, at a much lesser extent, of the wind direction to the component (Table 3.2). However, local meteorological conditions such as relative hu-

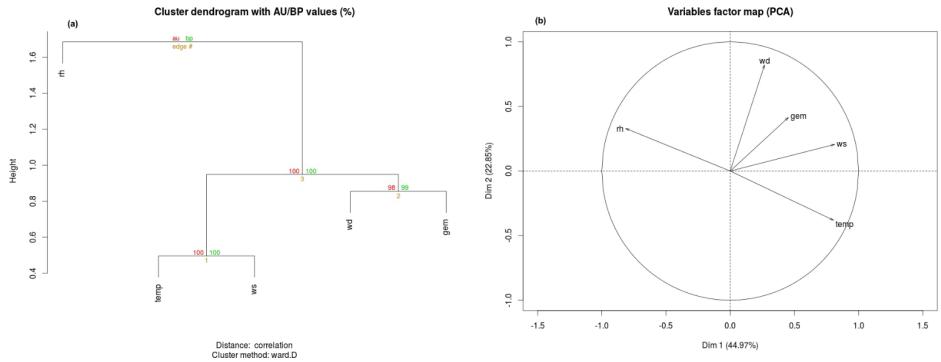

Figure 3.5: Results of application of the Cluster Analysis (CA).

midity and temperature are also relevant. Factor 2 explained 23% of the variability with the contribution of the variables wind direction, wind speed and temperature. Overall, the results of the multivariate exploration indicated the influence of the dispersion processes in controlling mercury levels recorded at the EMMA Station. To better understand the influence of wind, we correlated the wind frequency of the prevailing directions, NW and WNW, and GEM concentrations across the whole study period (October 2012-May 2016) and seasonaly. The results showed no significant correlation between the frequency of NW and WNW winds and GEM for the complete dataset ($p>0.05$) (Fig. 3.6). However, a direct correlation was found between the fre-

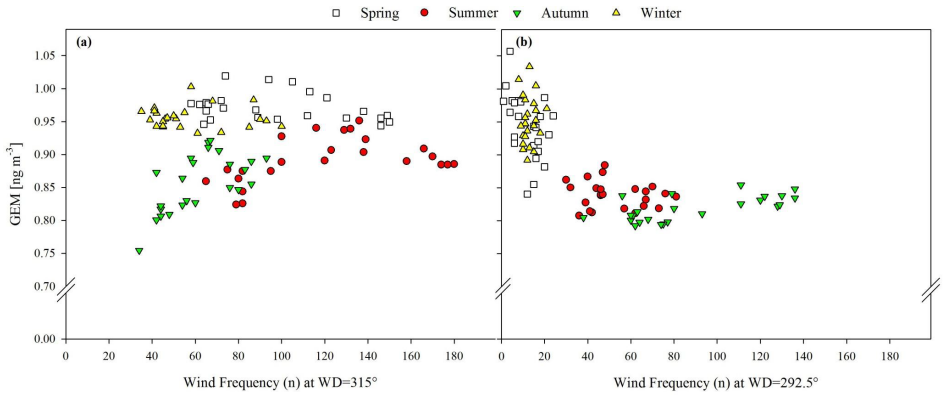

Figure 3.6: a) GEM concentration (ngm^{-3}) vs. frequency of the prevailing winds (WD=315°) and b) GEM concentration (ngm^{-3}) vs. frequency of the second prevailing winds (WD=292.5°), during the studied period (October 23, 2012 - May 15, 2016) at the EMMA station (Nahuel Huapi National Park, Northwestern Patagonia).

quency of NW and WNW winds and GEM concentration in the summer ($r=0.45$, $p=0.027$ and $r=0.46$, $p=0.02$, respectively) and autumn ($r=0.64$, $p=0.0007$ and $r=0.63$, $p=0.001$,respectively). Remarkably, considering the whole dataset, the GEM concentrations were found to

be directly and significantly correlated with the NW wind speed. However, the correlation factor was too low to allow describing a pattern ($r=0.13$, $p<0.001$). No clear relationship was found between WNW wind speed and GEM concentration ($p>0.05$). When the same analysis was performed seasonally, the correlation between NW wind speed and GEM was slightly stronger, particularly in spring ($r=0.37$, $p<0.0001$) and winter ($r=0.28$, $p<0.0001$); whereas the correlation between WNW wind speed and GEM was more apparent in autumn ($r=0.4$, $p<0.001$) than in any other season ($0.18 < r < 0.23$; $p<0.001$). Figure 3.7 summarizes the seasonal trend of GEM concentrations recorded at the EMMA station in Patagonia, highlighting: i-the marked influence of westerly winds, ii-the daily concentration pattern, with higher GEM levels during day-time than at night, and, iii-the lower GEM levels in autumn and a least contrasting day-night pattern. Finally, the direct relationship between GEM concentration and temperature computed for the whole data set resulted weak, although it was positive and significant ($r=0.132$, $p<0.001$).

3.3.4 Air mass back-trajectory analysis and potential influence of regional sources

The backward trajectory (BWT) analysis showed that, both high and low GEM periods occurred under the influence of air masses from westerly directions (Fig. 3.8). At low GEM levels, the BWT analysis pointed out the major influence of clean oceanic air masses coming from the west (W) and southwest (SW) (Fig. 3.8a-d). Low mercury concentration events were recorded during summer (February 2015 and 2016) and once in early autumn (April 2015). As highlighted in Figure 3.8a-d, these events were primarily related to air masses coming from the free troposphere (BWT starting from 2000-8000 m a.s.l) and resulting from a long range transport. Conversely, high Hg level events were recorded during spring (2012 and 2013) and summer (2013 and 2014), occurred concomitantly with air masses coming from not a common direction and characterized by a lower elevation of origin and

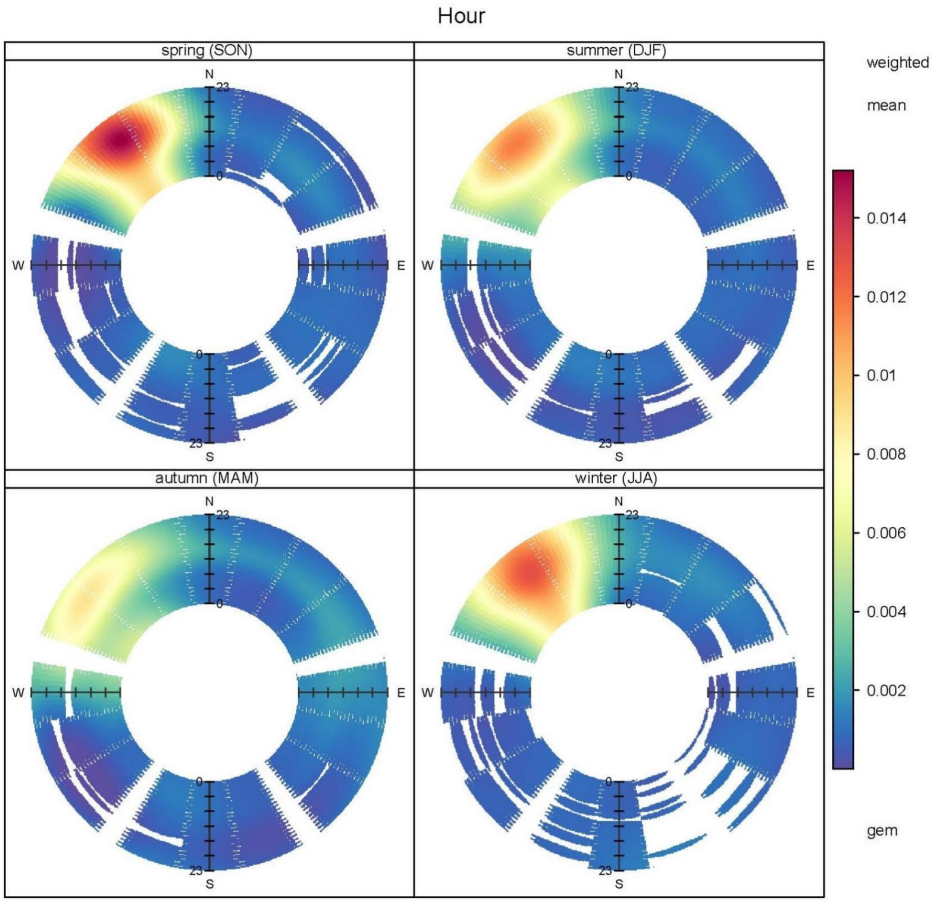

Figure 3.7: Rose Wind Pollution of Hg.

shorter range transport, thus involving a local/regional influence (see Fig. 3.8e-f). For all these trajectories a terrestrial influence can be further inferred, likely due to the effective barrier of the Andes cordillera that confront the westerly air masses changing their thermal and humidity properties as they cross the landmass (Garreaud et al. [2013]). This terrestrial contribution may likely include and reflect the influence of the several active volcanoes aligned in the cordillera which are

well known as sources of particulate and gaseous materials carried by the westerly winds that deposit in ecosystems at the eastern side of the Andes (Ribeiro Guevara et al. [2010], Bubach et al. [2012], Daga et al. [2014, 2016a,b]). At the particular geographic location of the EMMA station, the westerly winds arrive after discharging their humidity in the immediate west and east stretches surrounding the high altitudes, likely precipitating Hg in the stretch of the mountain range and piedmont coinciding with the westernmost limit of Nahuel Huapi National, at ca.55 km at the west of the EMMA station. Across this short longitudinal distance the pre cipitation grades from 3500 mmy^{-1} close to the Andes to ca. 1000-1200 mmy^{-1} at the EMMA Station (Mermoz et al. [2009], Bianchi et al. [2016]). It is worth mentioning that higher Hg levels recorded at the EMMA Station occurred during the austral dry season comprising the last part of the spring and the summer which may be related with the fact that the lower precipitation volumes in the area could prevent Hg precipitation in the boundaries of the cordillera and, thus, drier air masses could carry higher Hg levels to eastern locations of the Andean stretch.

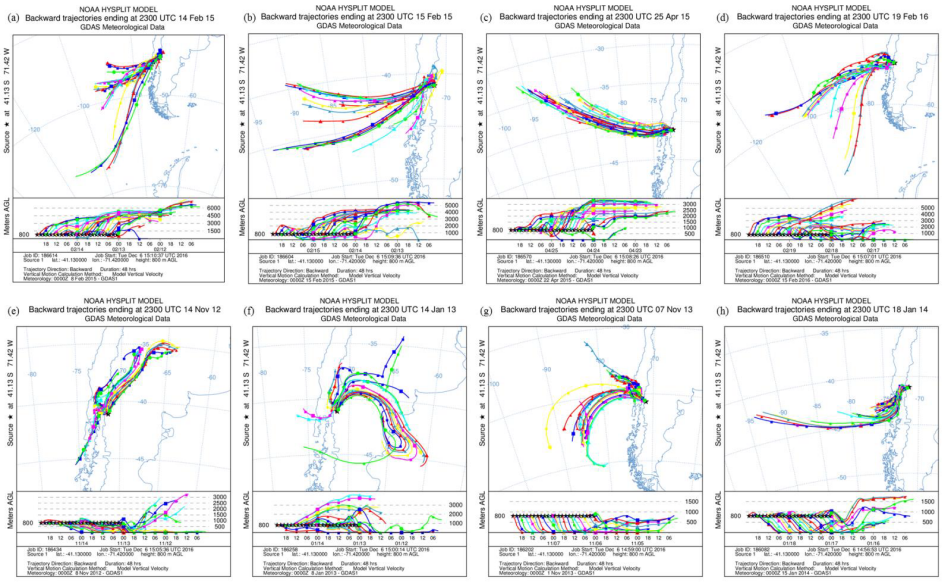

Figure 3.8: Backward trajectories of air mass reaching the EMMA station.

3.4 Conclusion

This work provides the first long-term records of gaseous elemental mercury (GEM) concentrations performed in Argentina at the GMOS EMMA monitoring station. The obtained results contribute to Hg knowledge in describing the current Hg levels in Nahuel Huapi National Park (Northwestern Patagonia), a remote area of South America with past and present records of Hg impact from natural sources. GEM showed concentrations ranging from 0.23 and 1.43 ngm^{-3} with an average of 0.865 $\pm$ 0.149 ngm^{-3}. These levels are in the lowest range within the concentration boundaries reported in the Northern-Southern hemispheric gradient resulting from GEM monitoring at the ground-based sites of the GMOS network. The local GEM concentration pattern showed significant seasonal and daily trends, characterized by higher GEM levels in spring and winter and a daily concentration pattern displaying higher GEM day-time concentrations and lower

night-time levels. Westerly winds showed up as the most influential variable directing GEM concentration and potentially contributing Hg. The BWT analysis, indicated that the influence of clean oceanic air masses coming from the west (W) and southwest (SW) likely determine low GEM periods. In contrast, high GEM periods are apparently driven by air masses from western and southern directions which likely receive inputs of Hg while blowing through the Andes, supplied by the numerous active volcanoes aligned in the cordillera. The results presented here portray to date the status of the atmospheric Hg fluxes in the Northwestern Patagonia. Currently, Hg monitoring networks cover several regions of the NH, however the coverage in the SH is by far lower. The new GMOS ground-based monitoring sites in different regions, including several stations in the SH, are expected to provide more comprehensive boundaries of Hg occurrence, and a better understanding of the environmental drivers interacting globally and regionally to help constraining the global biogeochemical cycle of this global pollutant.

Chapter 4

Case Study: Oceanographic campaign

4.1 Introduction

The Mediterranean[1] basin is an issue of growing concern for Hg due to the fact that the basin itself contains 65% of the world's cinnabar deposits (Sprovieri and Pirrone [2008], Sprovieri et al. [2010b]) and contains a number of active volcanos whose contribution to Hg emissions need to be better quantified (Pirrone et al. [2009]).
Higher Hg concentrations in this area are also expected due to solar radiation that initiates photochemical reactions (Sprovieri et al. [2003, 2010a]) in which one of the most important involved atmospheric gases is tropospheric ozone (O_3) (Volz-Thomas et al. [2003]). Ozone formation is driven by photo-chemically initiated reactions and is correlated to air temperature, so that elevated ozone levels are typically found in

[1]Most of the contents of this chapter is extracted by the article: Castagna, J., Bencardino, M., D'Amore, F., Esposito, G., Pirrone, N., Sprovieri, F., "Atmospheric mercury species measurements across the Western Mediterranean region: Behaviour and variability during a 2015 research cruise campaign", DOI:10.1016/j.atmosenv.2017.10.045.

the Mediterranean region in conjunction with high-pressure meteorological situations, clear skies and high temperatures (Simpson [1995]). Hence, the motivation that, since the last decades, has induced several research groups to investigate the link between atmospheric Hg and O_3 levels with emphasis on their driving mechanisms in the Marine Boundary Layer (MBL) (Weiss-Penzias et al. [2003], Holmes et al. [2010], Malcolm et al. [2003], Sprovieri et al. [2005b]). During the last 15 years several field and modelling studies, performed in the Mediterranean regions, have highlighted the complexity of the Hg cycle in the marine environment and the need to better understand chemistry and atmospheric interactions of Hg compounds in the MBL (Sprovieri et al. [2010b, 2003, 2010a], Hedgecock et al. [2003], Andersson et al. [2007], Kotnik et al. [2013, 2015], Gencarelli et al. [2015]). Once Hg enters the environment, its transport and fate is complex, influenced by chemical, physical, and biological factors (Mason et al. [2005], Harris et al. [2007], Selin [2009], Driscoll et al. [2013]).
In this context, and continuing the overall goal of the on-going MEDOCEANOR program, our research campaign aimed to collect and provide a new dataset of speciated mercury with concomitant meteorological and oxidant measurements within the Mediterranean basin (Sprovieri et al. [2003], Sprovieri and Pirrone [2008], Sprovieri et al. [2010a], Bencardino et al. [2014], Mastromonaco et al. [2017], Fantozzi et al. [2013]). Despite similar work has been done before in the same area, this study adds much needed data to the growing database regarding Hg speciation in the atmosphere, especially in the Mediterranean region, where Hg is an ubiquitous pollutant and temporal variation has an extremely important role in its cycling. Furthermore, the route of the 2015 oceanographic cruise campaign explored both natural stations, like as sites of deep sea or volcanoes, and anthropogenic sites close to the industrialized Italian coasts. The newly collected dataset will be presented and discussed in terms of spatio-temporal variability of the atmospheric Hg species. The variability of meteorological parameters and of air pollutant concentrations allowed to identify both anthropogenic and natural influences.

4.2 Experimental

4.2.1 Description of the monitoring campaign

During the summer of 2015, a set of continuous atmospheric measurements were performed to quantify concentrations of the three different atmospheric Hg species, to better understand the chemical-physical mechanisms occurring in the MBL and to observe Hg behavior under different meteorological conditions and emission source influences. The cruise was carried out in the Western Mediterranean sector on board the Research Vessel (RV) "Minerva Uno" of the CNR along the cruise path reported in Fig. 4.1. Atmospheric Hg and O_3 measurements along with other trace constituents, such as NO_x, SO_2, and meteorological parameters, were continuously performed during the cruise path, and at a number of selected monitoring sites, chosen both on-shore (coastal) and off-shore (open sea). The cruise campaign consisted of scheduled Stops (S) and Route legs (R) at, and along which, measurements have been made continuously during the sampling periods reported in Table 4.1. The track started in Palermo (Sicily) on the 26^{th} of June, northwards passing near Sardinia and Corsica islands, up to the Gulf of Genoa, then back southwards along the peninsula coast and docked at the Palermo harbour on the 13^{th} of July.

4.2.2 Sampling and Analytical Methods

Speciated Hg measurements

Speciated atmospheric Hg measurements were performed using Tekran Hg speciation system units (Models 1130 and 1135) coupled with a Tekran 2537A mercury vapor analyzer, which allows the simultaneous determination of GEM, GOM and PBM. During the cruise campaign the speciation units were located on the rooftop of the RV and connected to the Tekran 2537A analyzer through a heated PTFE line ($50°C$, 10 m in length). The integrated Tekran speciation system was configured to collect 2 hr GOM and PBM samples, while GEM is detected at each 5 min. During our monitoring campaign, the speciation

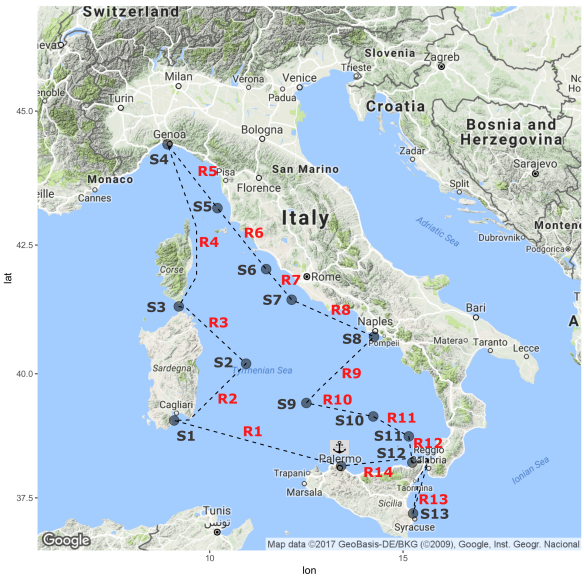

Figure 4.1: Oceanographic campaign route in Western Mediterranean Basin (the anchor shows the departure and arrival harbour).

measurements were performed following the Standard Operating Procedures (SOPs) of the Global Mercury Observation System (GMOS) Project, as described elsewhere (Landis et al. [2002], D'Amore et al. [2015], Sprovieri et al. [2016b]). However, to avoid that KCl-coated denuder became passivated with time, we re-coated and replaced a new denuder on a weekly basis. To limit RH influence, an high-flow and temperature controlled manifold, set at 100°, was additionally adopted. A soda lime trap just upstream of the Tekran 2537 sample filter inlet was further placed to extend the life of the gold cartridges. Soda lime, in fact, leaves to pass elemental mercury but scrubs deleterious compounds such as acid gases and halogen compounds (EPA [2002]). The Tekran 2537A analyzer was calibrated on a 71 h basis using the internal permeation tubes, to be consistent with SOPs established and still adopted within the GMOS network (D'Amore et al. [2015]). The permeation tube in each of the Tekran 2537A instruments was calibrated

just prior to the study as described in Landis et al. (2002) using a Tekran model 2505 primary calibration unit. The detection limit for GEM was lower than 0.1 ngm^{-3}, on the other hand, the method detection limit (MDL) for GOM and PBM, based on standard deviation of field blanks (3σ), was equal to 0.9 pgm^{-3}. For our convention we do not report Hg values below MDL in figures.

Chemical Parameters (O_3, NO_x and SO_2) and Meteorological measurements

O_3 measurements were carried out by an absorption method using the automatic UV Teledyne Photometric Ozone Analyzer (API Model 400E) on the top deck (about 10 m a.s.l.) that was calibrated by the UV photometric calibration procedure based on a UV (photolytic) O_3 generator device. A sampling flow rate of 0.8 $lmin^{-1}$ was used to measure O_3 concentrations with a time resolution of 1 min. NO_x observations were performed by a Teledyne Nitrogen Oxides Analyzer (API Model 200E) with a sampling flow rate of 0.5 $lmin^{-1}$ and a time resolution of 1 min. The instrument uses chemiluminescence detection, coupled with state-of-the-art microprocessor technology to provide the sensitivity and stability of use needed for ambient requirements of nitric oxide (NO), nitrogen dioxide NO_2 and the total nitrogen oxides NO_x. SO_2 measurements were performed using the fluorescence method by a Teledyne UV Fluorescence SO_2 Analyzer (API Model 100E) with a sampling flow rate of 0.6 $lmin^{-1}$ and a time resolution of 1 min. All these detectors were calibrated at the beginning of the measurement campaign and regular zero and span checks were performed every 2-3 days. Meteorological data (Air Temperature (Air-Temp), Wind Speed (Wind Spd), Wind direction (Wd), and Atmospheric Radiation (Atm-Rad)) were performed by an automatic meteorological station placed on the RV. In addition, data about navigation, such as coordinates of the vessel position, navigation direction, and the ship speed, were supplied with 1 min time resolution.

Backward Trajectory/NAAPS/FIRMS analysis

To establish the path of air masses collected aboard the RV as well as to discriminate possible source influences, the following complementary tools have been usefully adopted. The Hybrid single-particle Lagrangian integrated trajectory model (HYSPLIT), available at the NOAA Air Resources Laboratory (air), was used to calculate 48 hr backward trajectories to check the origin and pathway of the air masses crossing the ship, at midday, at midnight and when the RV was stopped at each station. The analysis were performed using the READY website (Draxler and Rolph [2003]), with the GDAS meteorological dataset, characterized by a grid scale of 1 degree.
The PSCF (Potential Source Contribution Factor) calculates the probability that a source is located at latitude i and longitude j, due to the passing of the air mass parcel. The PSCF is defined as follows:

$$PSCF = \frac{m_{ij}}{n_{ij}}$$

where n_{ij} is the number of times that the trajectories passed through the cell and m_{ij} is the number of times that a source concentration was high when the trajectories passed through the cell (i, j). The PSCF maps were realized by R software.
The Navy Aerosol Analysis and Prediction System (NAAPS), developed by the Naval Research Laboratory (nrl), analyzes satellite data and supports the interpretation of the aerosol size spectra by predicting the distribution of tropospheric aerosol and its surface concentration in terms of dust, sulphate or smoke concentration, through a model (Christensen [1997]).
The NCEP (National Centre for Environmental Prediction) maps, support a geo-potential picture showing the air mass circulation (cyclone or anticyclone). Daily maps at a geo-potential height equal to 850 mbar and 1000 mbar were used. The extension area we considered, includes the Mediterranean region, and is delimited by the following coordinates: 15° - 70° N and 15° W - 50° E (nce).
Finally, the Fire Information for Resource Management System (FIRMS)

(fir), which integrates remote sensing and Geographical Information System technologies to deliver global Moderate-Resolution Imaging Spectro-radiometer hot-spot/fire locations, was used to localize the active fires in the areas of interest along the route. Daily maps were downloaded to establish periods with a significant number of wildfires and to assess the biomass burning impact on measurement results.

4.2.3 Data Treatment

The whole cruise campaign consisted of periods when the ship rested on selected stations, and periods during which the ship travelled along specific routes (see Fig. 4.1). The full data-set with our observational measurements has been filtered in the way that measurements done during shipping have been excluded from the measurements done at stations and their nearest surroundings (the last two hours before arrival and the first two hours after departure) and treated separately in the following discussion. Measurements where a comparison of wind speed and direction with the speed and course the position of the ship showed that smoke from the stack of the ship might reach the monitoring station (ship speed smaller than wind speed, difference between wind direction and course of ship less than 30° have been excluded as well). We verified that only the 1% of our measurements data was potentially influenced by our ship plume.
When the R/V stayed at the stations, to avoid the contaminant from the ship plume the ship was anchored in the opposite direction of wind. In condition of wind calm (< 1 m/s), which occurred for the 14% over the total campaign, little transepts were conducted around the site, moving at low velocity (< 1 knot) in such a way that the ship's movement induced the plume to fall beyond the vessel.
All measurement data collected by automatic instruments has been processed for quality issues. Special care has been done to data on Hg species. Hg data have been screened with the GMOS-Data Quality Management (G-DQM) system, a tool developed within the GMOS project, able to quality check Hg data coming from Tekran (D'Amore et al. [2015]). G-DQM system was implemented on the basis of the

specific Standard Operating Procedures (SOPs) (Munthe et al. [2011]) developed within the GMOS project. We used automated feedback on Hg data quality assurance obtained from the G-DQM tool, with special care to calibration and speciation issues. The G-DQM results were also supervised in such a way that in the case that the automatic results from G-DQM are not appropriate the Quality Manager has the possibility to re-evaluate them. The resulting, quality-assured and quality-controlled, final Hg data-set consists of GEM, GOM and PBM concentrations where GEM values have been averaged over the corresponding 2 hr during which both GOM and PBM have been collected. Generally, in our discussion we often refers to the mean values recorded, for our variables, in a selected observing period. As error for the mean values we reported the associated Standard Deviation (SD) value.

4.3 Results and discussion

4.3.1 Overview of the measurements

Meteorological conditions

During the cruise campaign the typical Mediterranean summer conditions were encountered, with sunny and quite hot days. The air temperature average value was of $25.5 \pm 1.3°C$, with values range from $21.4°C$ to $30.3°C$, the maximum value being reached near Cagliari, Sardinia island. From the NCEP maps, we deduced that an anticyclone persisted throughout the whole sampling campaign. At first, the storm center of the anticyclone was located in the southwestern region of the Mediterranean basin, then moved northeastward up to Central Europe, to back again into the initial region.
During the whole route, the ship was always in areas with high synoptic pressure conditions. The local air pressure, monitored on board, never dropped below 1000 hPa and ranged from 1007 hPa to 1022 hPa with an average value equal to 1016 ± 3 hPa. The wind was mainly calm with a maximum speed value around 16 ms^{-1}.
The mean values of air temperature, pressure, atmospheric radiation,

and wind speed, for both stations and subroutes, are reported in Table 4.1.

Hg species and Chemical parameters (O_3, NO_x, SO_2) trends

Fig. 4.2a shows GEM, GOM and PBM data where GEM values have been averaged over the corresponding 2 hr during which both GOM and PBM have also been collected, while Hg and chemical parameters data recorded during the stations (S) and subroutes (R) are reported in Tab. 4.2.
Over the whole campaign the mean value of GEM was $1.6 \pm 0.5\ ngm^{-3}$. This result is in a good agreement with the background levels observed in the MBL of the Western Mediterranean Sea during previous oceanographic campaigns (Sprovieri et al. [2003, 2010b,a], Hedgecock et al. [2003]), which typically are higher than the background levels of the Southern Hemisphere (Diéguez et al. [2017]). In particular, during the 2003 summer cruise campaign the registered average GEM value was 1.9 ngm^{-3} for the complete route (North-West and South-East Mediterranean Sea), and 1.7 ngm^{-3} just for the sub-track performed in the North-Western Mediterranean area, which was similar to the route of this cruise campaign (Sprovieri et al. [2003]). GEM values showed a large variability ranging from 1.2 ngm^{-3} to 5.2 ngm^{-3} (median value of 1.5 ngm^{-3}), being this maximum value recorded along the central coast of Tuscany, near Rosignano where is located a chemical industry, the Solvay Chimica Italia. The high levels of Hg observed at specific sites along the route will be deeply discussed in the following dedicated section (par. 4.3.2).
GOM average value was 11.8 pgm^{-3} with a standard deviation of 15.0 pgm^{-3}, showing a large range from 1.1 pgm^{-3} to 128.7 pgm^{-3} and a median value equal to 7.9 pgm^{-3} (dataset of n=121). This latest peak was depicted in the Aeolian area, where volcanic degassing and/or eruptions can have a significant impact on the Hg emission levels (von Glasow [2010]). During the cruise campaign, GOM concentrations generally followed a typical diurnal cycle, with maximum values recorded

Table 4.1: Air Temperature, Air Pressure, Net Atmospheric Radiation, Wind Speed mean values (± Standard Deviation), for Cruise stations (S) and subroutes (R), are reported.

ID	Stops	Lat	Lon	Time Start	Time End	Air Temperature	Air Pressure	Net Atmospheric Radiation	Wind Speed
		(N)	(E)			$^{\circ}C$	hPa	W m^{-2}	m s^{-1}
R1	Palermo - Cagliari	-	-	26/06 16:00	28/06 04:00	24.3 ± 1.2	1016 ± 1.5	269 ± 332.9	3.3 ± 2.1
S1	Cagliari	39.07	9.08	28/06 04:00	28/06 21:30	25.1 ± 1.9	1014 ± 0.5	514.4 ± 301.6	5.4 ± 1.9
R2	Cagliari - MA2	-	-	28/06 21:30	29/06 05:30	23.8 ± 0.5	1016 ± 0.7	31.19 ± 131.5	2.8 ± 2.3
S2	MA2	40.13	10.56	29/06 05:30	29/06 12:00	25.2 ± 0.7	1018 ± 0.2	606.5 ± 30.9	1.1 ± 0.5
R3	MA2 - Bocche Bonifacio	-	-	29/06 12:00	30/06 12:00	24.6 ± 1.1	1017 ± 0.4	295.7 ± 340.0	2.3 ± 1.0
S3	Bocche Bonifacio	41.16	9.15	30/06 12:00	30/06 21:00	24.8 ± 0.4	1017 ± 0.2	247.8 ± 227.4	2.2 ± 0.6
R4	Bocche Bonifacio - Genoa	-	-	30/06 21:00	01/07 15:30	25.1 ± 0.8	1018 ± 0.4	277.2 ± 327.1	2.1 ± 1.1
S4	Genoa	44.23	8.54	01/07 15:30	02/07 09:45	25.4 ± 0.6	1019 ± 0.5	17.0 ± 114.0	1.0 ± 0.9
R5	Genoa - Rosignano	-	-	02/07 09:45	02/07 14:00	26.3 ± 0.7	1020 ± 0.2	657.6 ± 133.3	2.8 ± 1.5
S5	Rosignano	43.34	10.41	02/07 14:00	03/07 08:30	24.3 ± 1.8	1021 ± 0.6	11.8 ± 105.2	2.5 ± 0.8
R6	Rosignano - Civitavecchia	-	-	03/07 08:30	03/07 16:30	26.1 ± 0.5	1021 ± 0.8	501.1 ± 251.6	4.4 ± 2.2
S6	Civitavecchia	42.04	11.46	03/07 16:30	04/07 10:30	25.1 ± 0.8	1020 ± 0.5	52.4 ± 178.6	1.8 ± 1.1
R7	Civitavecchia - Fiumicino	-	-	04/07 10:30	04/07 12:50	26.9 ± 0.4	1019 ± 0.7	689.8 ± 114.1	3.0 ± 1.6
S7	Fiumicino	41.45	12.12	04/07 12:50	05/07 09:00	24.9 ± 0.5	1017 ± 0.3	270.7 ± 122.8	4.4 ± 0.6
R8	Fiumicino - Naples	-	-	05/07 09:00	05/07 15:30	26.0 ± 0.7	1017 ± 0.5	576.3 ± 247.0	4.4 ± 1.8
S8	Naples	40.47	14.14	05/07 15:30	06/07 09:00	24.9 ± 0.6	1017 ± 0.3	8.0 ± 93.7	1.5 ± 1.2
R9	Naples - MA1	-	-	06/07 09:00	06/07 13:30	26.0 ± 0.9	1017 ± 0.4	626.9 ± 118.0	3.5 ± 1.6
S9	MA1	39.42	12.5	06/07 13:30	06/07 20:40	27.3 ± 0.2	1017 ± 0.1	80.4 ± 129.6	2.3 ± 0.4
R10	MA1 - Marsili	-	-	06/07 20:40	07/07 13:00	26.5 ± 0.5	1016 ± 0.6	252.3 ± 345.5	1.5 ± 1.1
S10	Marsili	39.15	14.23	07/07 13:00	08/07 10:00	26.5 ± 0.7	1013 ± 0.7	50.2 ± 140.0	1.4 ± 0.7
R11	Marsili - Stromboli	-	-	08/07 10:00	08/07 11:00	26.7 ± 0.2	1011 ± 0.4	703.9 ± 121.5	3.3 ± 1.2
S11	Stromboli	38.45	15.1	08/07 11:00	09/07 08:00	26.4 ± 0.6	1009 ± 0.8	87.1 ± 196.8	1.4 ± 1.2
R12	Stromboli - Milazzo	-	-	09/07 08:00	09/07 10:15	26.6 ± 0.3	1009 ± 0.3	673.2 ± 127.8	2.0 ± 1.7
S12	Milazzo	38.22	15.24	09/07 10:15	10/07 09:00	26.1 ± 1.2	1009 ± 1.0	112.8 ± 244.9	2.1 ± 1.1
R13	Milazzo - Siracusa	-	-	10/07 09:00	11/07 14:00	26.6 ± 0.6	1014 ±1.9	340.1 ± 320.5	3.4 ± 1.7
S13	Siracusa	37.07	15.21	11/07 14:00	12/07 08:00	25.8 ± 0.2	1014 ± 0.6	5.9 ± 69.9	4.3 ± 0.9
R14	Siracusa - Palermo	-	-	12/07 08:00	13/07 08:15	26.9 ± 0.8	1014 ± 0.6	260.8 ± 331.3	3.4 ± 2.3

Table 4.2: Cruise stations (S) and subroutes (R); O_3, SO_2, NO_x, GEM, GOM and PBM mean values (± Standard Deviation), are reported.

ID	O_3 ppb	SO_2 ppb	NO_x ppb	GEM ng/m^3	GOM pg/m^3	PBM pg/m^3
R1	50.8 ± 4.9	NA	1.0 ± 0.6	1.4 ± 0.1	6.1 ± 0.9	2.6 ± 1.1
S1	54 ± 8.9	6.1 ± 1.3	3.0 ± 4.1	1.4 ± 0.1	6.6 ± 1.3	1.7 ± 0.5
R2	55.6 ± 5.0	6.6 ± 1.5	0.7 ± 0.5	1.3 ± 0.1*	5.1± 0.9*	1.5± 0.9*
S2	50.4 ± 3.5	7.1 ± 0.8	1.5 ± 1.0	1.3 ± 0.3	15.0 ± 5.7	1.8 ± 0.9*
R3	45.5 ± 2.5	6.1 ± 1.4	1.5 ± 1.5	1.4 ± 0.1	12.8 ± 5.0	3.4 ± 1.0
S3	NA	6.6 ± 1.7	2.7 ± 2.6	1.4 ± 0.1	20.5 ± 8.8	2.1 ± 0.9
R4	63.0 ± 11.4	6.1 ± 1.2	1.9 ± 1.3	1.4 ± 0.1	12.9 ± 4.8	2.4 ± 0.9
S4	50.4 ± 20.8	7.3 ± 1.8	18.8 ± 14.5	2.0 ± 0.3	11.4 ± 3.5	3.5 ± 0.8
R5	73.5 ± 7.9	7.8 ± 1.4	3.8 ± 2.0	1.5 ± 0.1	55.4 ± 22.8	2.4 ± 0.6
S5	45.4 ± 13.7	6.1 ± 1.3	10.1 ± 13.1	2.9 ± 1.8	17.5 ± 17.1	4.4 ± 1.5
R6	55.6 ± 2.4	5.9 ± 1.6	4.9 ± 3.9	1.6 ± 0.2	10.5 ± 0.9	1.4 ± 0.2
S6	40.9 ± 13.5	7.6 ± 1.1	9.8 ± 9.7	1.7 ± 0.1	8.6 ± 4.1	2.4 ± 0.8
R7	87.2 ± 4.2	6.3 ± 2.2	4.9 ± 3.9	2.0± 0.1*	10.0± 0.9*	4.7± 0.9*
S7	60.1 ± 17.9	6.8 ± 2.4	4.5 ± 6.9	1.7 ± 0.2	7.1 ± 8.0	2.0 ± 0.5
R8	47.3 ± 8.4	6.6 ± 0.7	5.2 ± 0.9	1.7± 0.1*	2.0± 0.9*	3.3± 0.9*
S8	32.6 ± 11.6	8.1 ± 1.5	16.6 ± 18.2	1.6 ± 0.1	5.9 ± 4.2	1.8 ± 0.7
R9	50.5 ± 2.9	8.2 ± 1.3	2.6 ± 1.7	1.4± 0.1*	3.0± 0.9*	NA
S9	46 ± 3.6	7.5 ± 0.9	1.3 ± 0.4	1.4 ± 0.1	9.2 ± 1.4	1.2 ± 0.9*
R10	50.5 ± 2.9	7.2 ± 1.1	1.9 ± 0.5	1.4 ± 0.1	1.2 ± 0.3	1.2 ± 0.3
S10	49.6 ± 3.1	8.3 ± 1.3	1.2 ± 1.3	1.4 ± 0.1	3.3 ± 2.5	NA
R11	40.8 ± 1.1	9.8 ± 0.4	1.5 ± 1.5	1.4± 0.1*	6.6± 0.9*	NA
S11	44.2 ± 2.8	9.9 ± 2.3	1.0 ± 1.1	1.4 ± 0.1	17.0 ± 10.4	NA
R12	44.4 ± 4.5	10.6 ± 0.9	1.4 ± 0.5	1.4± 0.1*	19.0± 0.9*	2.5± 0.9*
S12	37.5 ± 11	9.8 ± 1.3	7.4 ± 7.9	1.4 ± 0.1	33.4 ± 43.6	2.2 ± 0.9
R13	43.2 ± 6.5	8.7 ± 1.8	2.4 ± 1.2	1.6 ± 0.1	4.0 ± 0.9*	1.7 ± 0.97
S13	41.7 ± 6.7	8.8 ± 1.4	3.3 ± 2.6	1.6 ± 0.2	6.9 ± 7.0	2.3 ± 0.7
R14	46.9 ± 5.3	9.8 ± 2.4	3.0 ± 6.4	1.5 ± 0.1	14.7 ± 14.4	1.9 ± 0.9

*just 1 data available; instrumental errors have been considered.

during daylight, typically between 11:00-17:00, and nocturnal minimum values (Fig. 4.2b) (Sprovieri et al. [2003], Malcolm et al. [2003]). Although there are uncertainties on the atmospheric oxidants involved in the oxidation of GEM, studies suggest that Hg-bromine chemistry is particularly active in marine environments. This statement was also confirmed by previous results of Hg measurements and box-modelling studies, where the GEM oxidation by Br-containing compounds seems to be the fundamental reaction to produce GOM (Hedgecock et al. [2003], Sprovieri et al. [2005b,a, 2010a]). However, during the first days (27^{th} and 28^{th} of June, along the Palermo-Cagliari sub-route), it was not evident an increase in GOM daylight levels (Fig. 4.2b). As will be highlighted in the next paragraph 4.3.2, the Hysplit backward trajectory confirms that air masses collected in correspondence of Cagliari were coming from Sardinia, where some wildfires were occurring. During our sampling there was a major availability of particulate, mainly due to wildfire emissions. The subsequent up-take of GOM over the available particle surface could be the reason why we did not observe an expected enhancement in GOM values whereas we observed a quite concomitant increase in PBM levels (Feddersen et al. [2012]).
A significant diurnal peak of GOM, which amounted to 71.5 pgm^{-3}, was registered at 16:15 UTC of the 2^{nd} of July, in proximity of Rosignano (Tuscany). Although the time of the peak could fit within the typical diurnal GOM cycle, its high value might suggest an anthropogenic influence, being this latest hypothesis confirmed by high values recorded at the same time and in the same site for the other Hg species (see Fig. 4.2a and par. 4.3.2, for an in depth examination).
A particular nocturnal peak (about 32 pgm^{-3} at 01:25 UTC), unexpected by diurnal cycle, was recorded during the night of 9^{th} of July, when the research ship was anchored near Stromboli: the time condition of this peak excludes the linkage with photo-production processes, being it most probably due to an influence of volcanic emissions. In the following day, the absolute maximum value of the whole campaign, above 120 pgm^{-3}, was registered. However, this peak will be discussed in detail in the paragraph 4.3.2. The last GOM peak encountered, at 16:45 UTC of the 12^{th} of July, about 49 pgm^{-3}, was measured in the

Strait of Messina, although it could be included in the GOM cycle, the high value could make in mind again an additional source. By checking the wind direction it seems that this value was recorded under wind condition coming from the Aeolian islands, thus making explicable a possible volcanic influence.

Regarding PBM levels, we obtained a mean value for the entire campaign equal to 2.4 ± 1.1 pgm^{-3} with a range between 0.9 pgm^{-3} and 6.6 pgm^{-3} and a median value of 2.2 pgm^{-3} (dataset of n=94). The maximum peak of PBM, equal to 6.6 pgm^{-3} was registered during the stop of the RV in Rosignano (Tuscany), where, as already seen, the other Hg species showed a concomitant increase in values, probably due to an anthropogenic influence. The Tekran Model 1135 unit we used to record PBM in our study, due to its configuration, is able to measure Hg bind only on the finer fraction (particles with an aerodynamic diameter less than 2.5 μm), thus removing the coarser one. PBM can be emitted directly from sources but it is mainly formed through gas-particle partitioning (Kim et al. [2012]). In the Mediterranean basin there are numerous natural sources (i.e. sea spray, dust, volcanic ashes) contributing to high of levels of atmospheric particulate matter, mainly in its coarser fraction (Mamane et al. [2008]). In the area of our investigation is then likely to found higher concentrations of PBM bound to coarse particle than the finer particulate size (Malcolm et al. [2003]).

Since our instrument do not measure the Hg coarse fraction, our data mostly underestimates the marine as well as the volcanic contribution. In marine environment, sea spray make available sea-salt particle surfaces on which pre-existing GOM can adhere, thus contributing to generate PBM. In ideal conditions, we would expect a correspondence between the GOM and the PBM diurnal cycle, just like in the case of the 29^{th} of June, where, after the GOM peak of photochemical origin, we observed a succeeding enhancement in PBM values (see par. 4.3.2). During our campaign the typical PBM diurnal cycle was not so clear, probably due to the coexistence of a mixture of various influences, thus hiding the expected PBM profile in marine environment.

During the route, inshore, we sometimes approached areas where Large

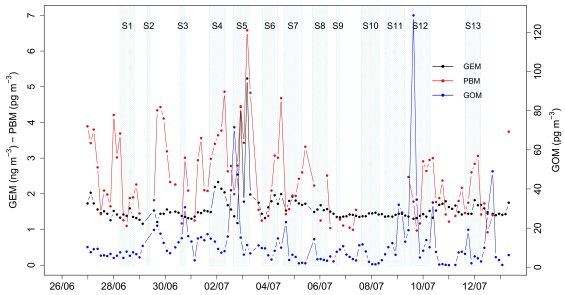

(a)

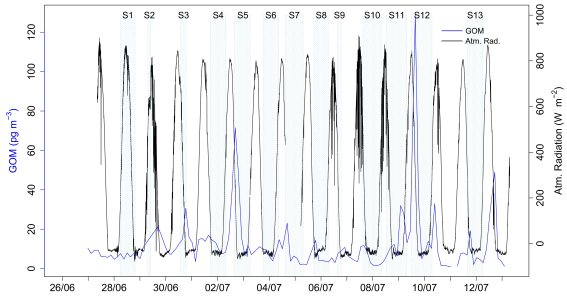

(b)

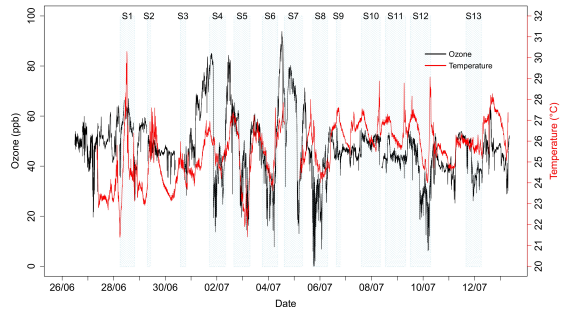

(c)

Figure 4.2: Temporal variations of atmospheric Hg and meteorological parameters recorded during the oceanographic campaign (light blue strips highlight stops): Temporal variations of atmospheric Hg species (GEM, PBM and GOM) (a), GOM and Atmospheric Radiation (b); O_3 and temperature levels (c).

Industrial Point Sources are located. Emissions from these large industrial sites are currently regulated by the Directive 2008/1/EC of the European Parliament and of the Council concerning Integrated Pollution Prevention and Control (IPPC). The European Pollutant Release and Transfer Register (E-PRTR) represents, at a European level, a truly integrated pollutant emissions register, and collects the information provided by those facilities whose pollution impact on the environment is very large and troubling for human health. Concerning Hg, which is included in the Annex III of The Directive 2008/1/EC within the list of the main polluting substances to be taken into account, the threshold values for releases are set equal to 10 $kgyr^{-1}$, for air; 1 $kgyr^{-1}$, for water; and 1 $kgyr^{-1}$, for soil, respectively. In order to check the atmospheric Hg emissions from the IPPC activities we encountered during our campaign, the E-PRTR register has been browsed and queried online (epr), and we found that four of the sites currently included in the E-PRTR register were approached during our campaign: Cagliari, Rosignano, Civitavecchia, and the Priolo area (near Siracusa).
Even if these latest sites are recognized as large industrial facilities for Hg we did not detect any high values in proximity of Cagliari, Civitavecchia, and Siracusa. Specifically, Hg levels in Cagliari reached about 1.4 ngm^{-3} for GEM, 6.6 pgm^{-3} for GOM and 1.9 pgm^{-3} for PBM; in Civitavecchia, we had 1.7 ngm^{-3} for GEM, 8.6 pgm^{-3} for GOM and 2.6 pgm^{-3} for PBM; in Siracusa, 1.6 ngm^{-3} for GEM, 6.9 pgm^{-3} for GOM and 2.6 pgm^{-3} for PBM. Differently, near Rosignano we detected the main peak of the whole campaign, as already discussed.

The Table 4.3 shows a comparison between Hg data of this study with other data collected on-board a ship or in a coastal site. The Hg (GEM, GOM, and PBM) mean values of this measurement campaign were in accordance with previous values, except for the values recorded in China (Bohai and Yellow Sea) and in the North Pacific Ocean, where GEM showed higher values. Regarding O_3, the mean value was of 47.7± 12.3 ppb and the range was between about 32 ppb and 93 ppb. The observed level variations of O_3 confirmed the typical

Table 4.3: Literature comparison data for GEM, GOM, PBM and O_3.

Reference	Location	GEM		GOM		PBM		O3	
		Range ngm^{-3}	Mean±SD ngm^{-3}	Range pgm^{-3}	Mean±SD pgm^{-3}	Range pgm^{-3}	Mean±SD pgm^{-3}	Range *ppb*	Mean±SD *ppb*
This study	Mediterranean Sea	1.2-5.2	1.6±0.5	1.1-128.7	11.8± 15.0	0.9-6.6	2.4±1.1	13.9-90.6	47.7±11.8
Sprovieri et al. [2010b]	Mediterranean Sea	-	-	0.2-30.1	11.6±9.8	4.8-17	9.6±3.2	-	-
Sprovieri et al. [2010b]	Mediterranean Sea	-	1.2±0.2	1.0-13.1	6.3±4.4	0.3-7.1	1.4±1.7	-	-
Sprovieri et al. [2010b]	Mediterranean Sea	0.5-4.4	1.7±0.3	0.1-25.3	6.2±5.5	0.2-11.9	2.6±2.0	-	-
Sprovieri et al. [2010b]	Mediterranean Sea	0.2-116.9	2.2±4.0	0.1-97.8	8.2±10.4	0.4-77.5	11.2±10.1	-	-
Mastromonaco et al. [2017]	Mediterranean Sea	<LOD-4.5	1.7±0.4	-	-	-	-	-	-
Mastromonaco et al. [2017]	Mediterranean Sea	0.7-3.2	1.5±0.3	-	-	-	-	-	-
Vetsev et al. [2011]	Mediterranean Sea	-	-	-	-	-	-	-	50.1±10.0
Bencardino et al. [2014]	Mediterranean Sea	-	-	-	-	-	-	22.0-73.2	48.8±9.3
Wang et al. [2016]	Bohai Sea and Yellow Sea	-	2.03± 0.72	0.2-9.8	2.5 ± 1.7	1.8-28.4	8.2 ± 6.3	-	-
Wang et al. [2016]	Bohai Sea and Yellow Sea	-	2.09 ± 1.58	0.8-15.3	4.3±2.5	1.0-31.3	8.3 ±6.9	-	-
Engle et al. [2008]	US Gulf Coast	-	1.6 ± 0.3	-	4.0 ± 7.5	-	2.7 ± 3.4	-	-
Cheng et al. [2014]	Coastal-rural site (Canada)	-	1.38 ± 0.20	-	0.4 ± 1.0	-	3.5 ± 4.5	-	-
Cheng et al. [2014]	Coastal-urban site (Canada)	-	1.67 ± 1.01	-	2.1 ±3.4	-	2.3 ± 3.1	-	-
Laurier and Mason [2007]	North Atlantic Ocean	-	1.63± 0.08	<LOD-27	5.9	-	-	-	-
Laurier et al. [2003]	North Pacific Ocean	1.6-4.7	2.5±0.5	0.15-92.4	9.5	-	-	-	-
Soerensen et al. [2010]	Global Ocean	-	1.53±0.58	-	3.1 ± 11.0	-	-	-	-

well-known behaviour (Warneck [1999]), in which it increases during the day, due the photochemical production, and at night reduces itself (Fig. 4.2c). Similarly to GOM, that did not show a marked gradient day/night in the first days of the campaign (27^{th} and 28^{th} of June, along the R1 sub-route), also O_3 did not have a significant gradient. In remote areas, far away from NO sources, the only effect of day-night did not show a large gradient of O_3 like in other cases, for example, in the open sea (MA1 and MA2) and in the Aeolian area (Marsili, Stromboli), where ozone concentrations did not go below 40 ppb, as well as, overnight temperatures did not go below $25°C$. This occurrence being due to the fact that sea breezes, which usually brought colder air, were absent, and the area was hotter for the volcano presence. Passing through the Strait of Messina, we observed a decreasing in O_3 levels (about 40 ppb), suggesting the influence of O_3 titration by shipping emissions, which, as confirmed by modelling studies in this area, act in reducing O_3 concentrations by 10-20% (Gencarelli et al. [2014]). The European health long-term objective for ozone levels is set at 120 μgm^{-3} as a maximum daily 8-hour mean and calculated for each day as the maximum of 8 hour running average of observed hourly values (Parliament and of the Council [2008]). During our cruise campaign the EU limit value (120 $\mu gm^{-3} \simeq$ 60 ppb) exceeded was exceeded 5 times over 15 days of observations (Fig. 4.3): in the surroundings of Cagliari, Genoa, Rosignano, Fiumicino, and Naples. The O_3 statistic was in accordance with previous measurements, as shown by the Table 4.3.

The spatial distribution of NO_x allows to distinguish sites affected by anthropogenic sources from sites with a predominance of natural sources. The mean value of NO_x recorded for the whole cruise campaign was 5.7 ± 9.4 ppb and the minimum and maximum values were 0.5 ppb and 177.7 ppb, respectively. Stops with a massive contribution of NO_x, such as, Genoa, Rosignano, Civitavecchia, and Naples, were identified as anthropogenic sites, while the other sites showed a minor anthropogenic impact. Generally, also sub-routes did not show important contribution of NO_x (see Table 4.2). Regarding to SO_2, the mean value was of 7.7 ± 2.2 ppb. The minimum value was about

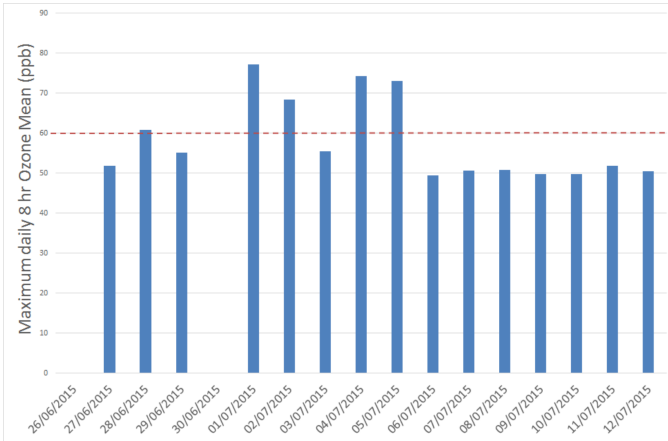

Figure 4.3: Temporal variations of the maximum daily 8 hr O_3 mean computed on the O_3 values recorded during the oceanographic campaign.

0.5 ppb, and the maximum recorded was about 17 ppb in the Strait of Messina, where shipping traffic is massive. Around the Aeolian Islands region (S11-R12-S12) we recorded relative higher levels of SO_2 (about 9-10 ppb).
A preliminary analysis has been made through a correlation analysis for Hg species and chemical parameters recorded during the stations and the subroutes (see Fig. 4.4 and Fig. 4.5). However, we preferred to continue analyzing each pollutants separately, identifying the peaks and hence, the hot-spot events.

4.3.2 Hot-spot events

During the measurement campaign, remarkable peaks of Hg and/or O_3 were detected, and an in depth discussion about these specific events will follow in the next sub-paragraphs.

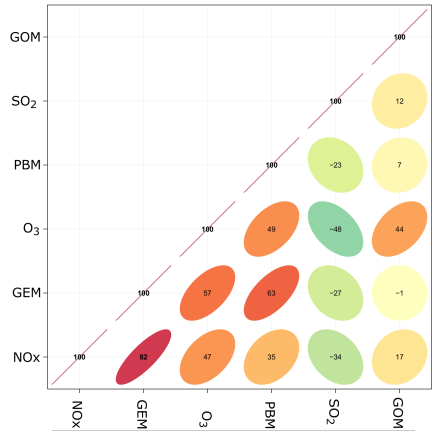

Figure 4.4: Correlation analysis for Hg species and chemical parameters measured during the subroutes (R).

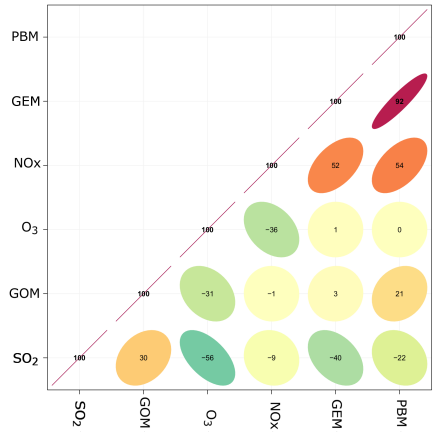

Figure 4.5: Correlation analysis for Hg species and chemical parameters measured during the stations (S).

Wildfires in Sardinia (S1)

The first case was observed on June 28^{th}, near the Sardinia island, in the harbour of Cagliari, where the maximum daily 8 hr O_3 mean exceeded the EU limit value (Fig. 4.3) whereas the NO_x concentration

was not particularly high (see Table 4.2). Furthermore, at the same station, we also recorded the maximum value for temperature (about $30°C$).
By checking the FIRMS tool an hot spot fire was identified in the south Western of Sardinia during the two days of 27^{th} and 28^{th} of June. A potential wildfire influence on the high values of both ozone and temperature, was then supposed. Furthermore, the NOAA-Hysplit model was used to calculate 48 hr backward trajectories for the RV's position. As shown in Fig. 4.6a, the backward trajectories crossed the southern part of the island intercepting fire smokes (red points from FIRMS data in Fig. 4.6a) before reaching the ship position (black point in Fig. 4.6a), thus supporting a possible wildfire influence on the higher O_3 concentrations we measured during the stop at Cagliari (see Fig. 4.2c). At low wind speed, lower O_3 values were observed even if, by a time plot with colours identifying the wind direction, we noticed that these data were concerning to the late evening, when the solar radiation was decreasing (Fig. 4.6b). During this event the Hg mean values for S1 were $1.4 \pm 0.1\ ngm^{-3}$ (n=5), $6.6 \pm 1.3\ pgm^{-3}$ (n=5), $1.7 \pm 0.5\ pgm^{-3}$ (n=5) for GEM, GOM, and PBM, respectively. Specifically, GEM concentrations ranged from 1.3 to 1.6 ngm^{-3} and PBM showed a relative peak of 2.26 pgm^{-3} (see Fig. 4.2a) while GOM concentrations showed a quite low variability. As known, wildfires are important sources of mercury emissions contributing significantly to the atmospheric mercury load (De Simone et al. [2016]). Large uncertainties still exist on the exact emission partitioning within each atmospheric Hg species (Obrist et al. [2007]). Previous studies stated that the majority of wildfire related to mercury emissions is in the form GEM, but a sizeable fraction can be released as particulate-phase mercury as well, while no significant GOM increases have been detected in biomass smoke (Friedli et al. [2003a,b]). Our observations confirm research studies already done in this field.

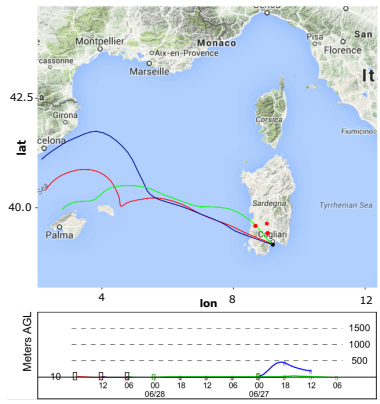

(a)

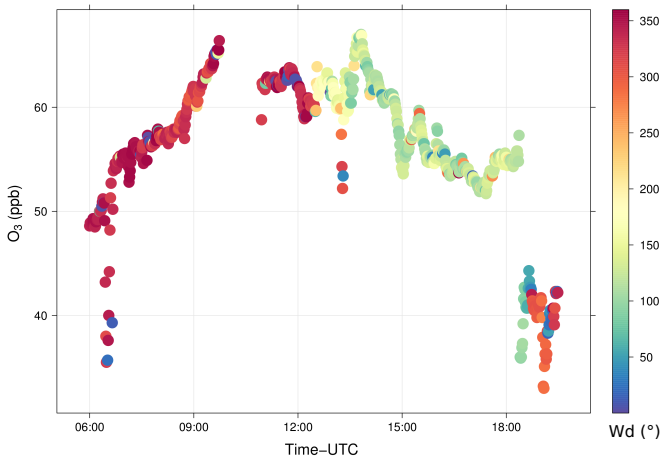

(b)

Figure 4.6: Backward trajectories (Hysplit) at the ship position (black point) and presence of wildfires (red points, FIRMS) (a), O_3 time plot with colours identifying the wind direction for June 28th (b).

In-situ production of GOM in the MBL (R3)

Along the sub-route R3, the ship was coming off-shore, going eastward of Sardinia, from midday of June 29^{th} till midday of the day

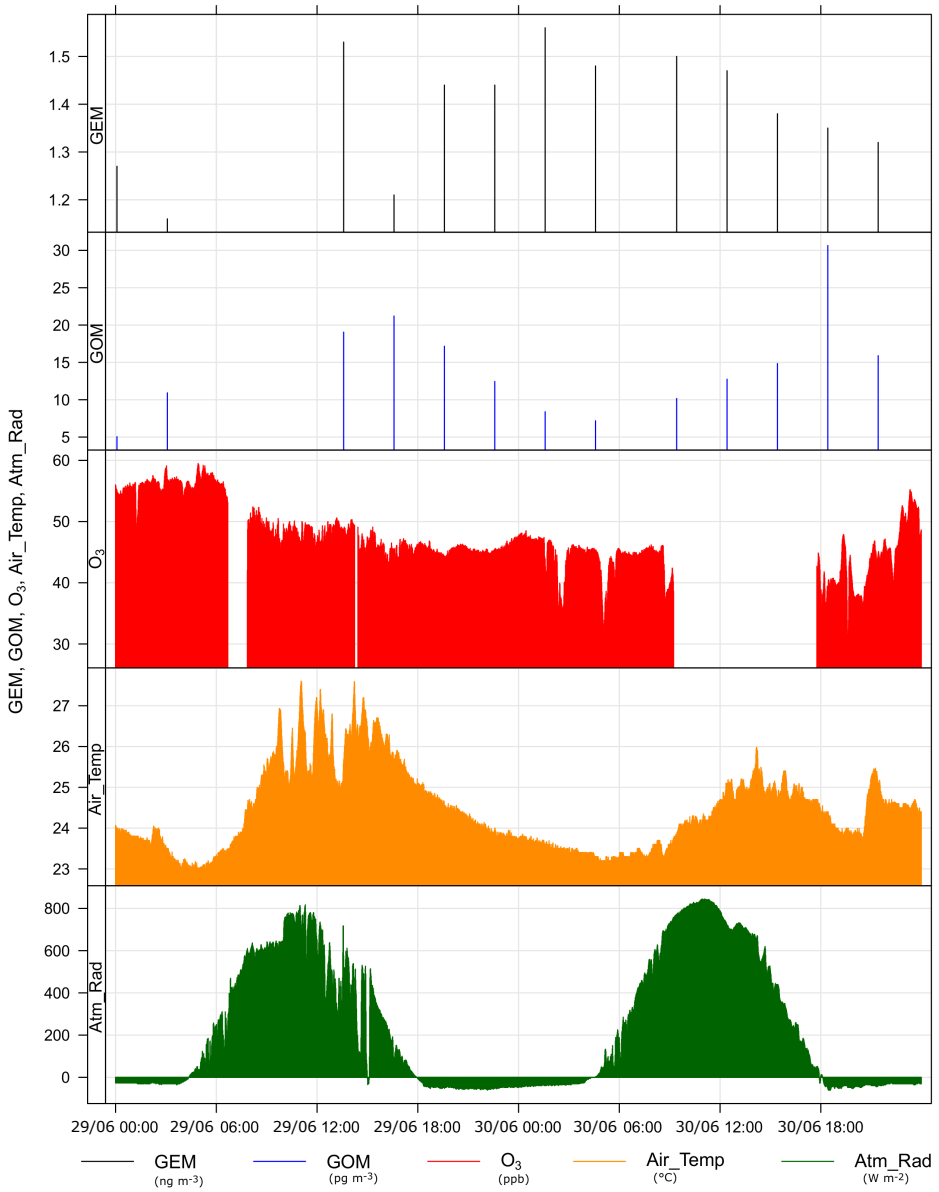

Figure 4.7: Time series for GEM, GOM, O_3, Air_temp and Atm_Rad during R3.

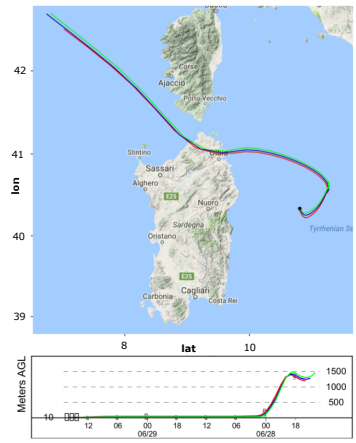

Figure 4.8: Backward trajectories (Hysplit) at the ship position (black point).

after (see Table 4.2). The mean values calculated for the sub-route R3 were 1.4 ± 0.1 ngm^{-3} (n=7), 12.8 ± 5.0 pgm^{-3} (n=7), 3.4 ± 1.0 ngm^{-3} (n=7) for GEM, GOM, and PBM, respectively. As Fig. 4.7 shows, within this temporal window, and specifically around the central hours (from 13:00 to 16:00, UTC) of the first day of navigation, the GEM concentrations registered an increase (up to 1.5 ngm^{-3}), in conjunction with the peak of both solar radiation (around 800 Wm^{-2}) and temperature (above 27°C). The diurnal variation, therefore, may be attributed to greater daytime production of GEM leading support the idea that photo-chemically produced oxidants are responsible for the major part of the GOM production. The increase in GEM was in fact suddenly followed by an increase in GOM. The sunny and quite warm weather, in this specific event, could suggest firstly an evasion of GEM from the sea surface (Carbone et al. [2016]) followed by the oxidation of GEM in the MBL with an *in-situ* production of oxidised Hg species. Our observation show a drop down of GEM values in conjunction with an increase in levels of GOM (21.2 pgm^{-3}). A similar pattern, even if less evident, has been observed in the following day

(30^{th} in June), when GEM levels increased again until to 1.5 ngm^{-3}, with a following slight drop corresponding to an increase in GOM concentrations (see Fig. 4.2) As suggested by previous both modeling and field studies, the possibility that comes to mind, is a reactant whose concentration is closely linked to daytime photochemistry, either in that it is the product of a photolytic process or is the product of a reaction involving a photolysis product. At the same time, the fact that O_3 levels slightly decrease (see Fig. 4.7 and Table 4.2), could rely on the presence of Br and OH, and more feasible on H_2O_2 production as oxidants (Hedgecock and Pirrone [2001], Sprovieri et al. [2003, 2005b, 2010b,a], Hedgecock et al. [2003]). This is because reactive Br leads to O_3 depletion (Finlayson-Pitts [2010], Obrist et al. [2011]) and OH and H_2O_2 are primarily produced by the photolysis of O_3 in the presence of water vapor (Read et al. [2008]).
Unless the magnitude of the *in-situ* production is known, it is not possible to distinguish between them and therefore it is not possible to draw conclusions regarding, for instance, the influence of atmospheric transport on deposition at a given site. If the measured GOM were being transported from anthropogenic sources the diurnal variation would not be so clear, because any variation in source strength would not follow a strictly diurnal pattern at the measurement site. In our case, the back trajectory calculations, showed in addition that air masses being sampled, were coming from the sea surface in the previous hours (see Fig. 4.8), thus allowing us to exclude, for this specific event, any anthropogenic influence. The possibility that the high GOM values represent transport from nearby sources has been discounted also for the meteorological conditions prevailing during this measurement period of the campaign characterized, in particular, by a low average wind speed (2.8 ms^{-1}), and indicating that transport was not a major factor in determining the GOM observed concentration. GOM is known to be emitted from industrial sources, but due to its chemical-physical properties it can be transported only for short distances from its point of production. Diurnal variation in GOM concentrations have been observed previously both in the Mediterranean (Sprovieri et al. [2003], Hedgecock et al. [2005]) and in the Pacific (Laurier et al. [2003]). In

both cases there was an absence of potential anthropogenic sources suggesting that GOM was being formed by the oxidation of GEM within the MBL itself. The previously cited studies also showed that the effects of meteorological parameters have a strong impact on GOM concentrations in the MBL (Sprovieri et al. [2003]). Highest GOM concentrations consistently occurred during periods of reduced wind speed and maximum Radiation. Wind speed thus controls the deposition velocity rates and the removal of GOM and the photochemistry controls the presence of photochemically induced oxidants, high Radiation otherwise induce high reactive-oxidant concentrations (Vogt et al. [2016], Dickerson et al. [1999], von Glasow et al. [2002]).

Industrialized area in Genoa (S4)

The Gulf of Genoa is a suffering area for many anthropogenic sources of pollution, such as the strong shipping traffic, due its harbour activities, and the massive presence of industries, both producers of NO_x, precursors of ozone (Benkelberg et al. [2000]). Furthermore, the harbour of Genoa, is the biggest Italian harbour for extension with a huge volume of traffics per year; additionally, the North of Italy, is densely industrialized, therefore the emissions are massive and so the city of Genoa usually exceed the European air quality limit value (Parliament and of the Council [2008]), set at about 60 ppb for ozone, and calculated like as the maximum daily 8 hr O_3 mean. For example during the 2014, at Genoa, there were 64 days exceeding the O_3 EU limit value (Di Vito et al. [2016]). According the expectations, the maximum daily 8 hr O_3 mean on the 1^{st} of July, day including part of the route until Genoa and part of the stop (see Table 4.2) exceed the EU limit (Fig. 4.3). Moreover, we recorded high values for O_3, about 60-70 ppb, during the ship movement, and about 50 ppb in the harbour (see R4 and S4 in Table 4.2). The presence of high O_3 concentration was also confirmed by the highest NO_x concentration recorded during the whole cruise (18.8 ± 14.5 ppb). Furthermore, an increase of GEM (with a peak of 2.6 ngm^{-3}), and of PBM (with a peak of 4.9 pgm^{-3}) were measured, whereas, the resulting mean value for GEM was 2.0

$\pm$ 0.3 ngm^{-3} (n=5), for GOM was 11.4 $\pm$ 3.5 pgm^{-3} (n=5) and for PBM was 3.5 $\pm$ 0.8 pgm^{-3} (n=5), in according with the value of previous campaign (in winter: about 2 ngm^{-3} for GEM, and 5-9 pgm^{-3} for PBM (Bencardino et al. [2013])). Supported by Hysplit, with the trajectory ending at 0:00 UTC, of July, 2nd, we can observe that the measured air masses were coming from the industrialized coasts (see Fig. 4.9a). Moreover, the Potential Source Contribution Function (PSCF) for the GEM trajectories ending at 9:00 UTC of July, 2^{nd} was represented. The PSCF map is the result of 20 trajectories at 90° percentile, each restarted after 1 hour for 20 times, to consider the time of the whole stopping. The PSCF probabilities confirmed high values over the industrialized coasts (see Fig. 4.10). During the stop (see S4 in Table 4.2), local data captured by the meteorological station on the ship confirms that the higher values of GEM had brought by the wind blowing from the coast, north-westerly (see Fig. 4.9b). On the other hand, the presence of industrial pollution increased the contribution of fine particulate, so Hg could bind to it, increasing the PBM levels.

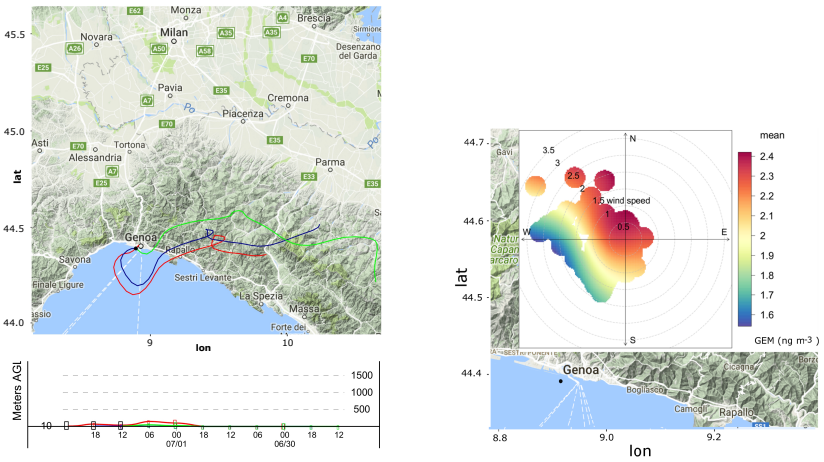

(a) (b)

Figure 4.9: Backward trajectories (Hysplit) at the ship position (black point), ending at 0:00 UTC of July, 2^{nd} (a), GEM Wind Rose during S4 (b).

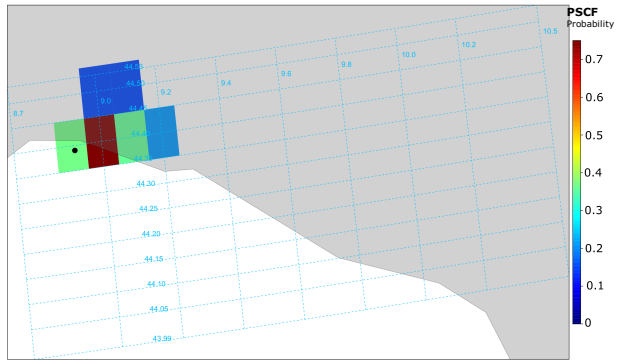

Figure 4.10: PSCF probabilities for GEM concentrations (90th percentile) at S4.

Mercury-based industry in Rosignano (S5)

Along the Tuscany coast, precisely in the harbour of Rosignano, we observed the highest value of GEM (about 19.54 ngm^{-3}, value with sampling time of 5 min, corresponding to 5.2 ngm^{-3} of average value calculated on 2 hr) and the highest peak of PBM, about 6.6 pgm^{-3} and an important peak of GOM, about 71.5 pgm^{-3}. On the other hand, the mean values were respectively 2.9 ± 1.8 ngm^{-3} (n=5), 17.5 ± 17.1 pgm^{-3} (n=5), 4.4 ± 1.5 pgm^{-3} (n=5) for GEM, GOM and PBM. Tuscany is an Italian region known from literature like a site highly polluted by Hg due to both natural and anthropogenic sources: the Mt. Amiata, in Tuscany, mostly consist of Cinnabar (HgS) rocks and was exploited as a mine in the past; furthermore, in Rosignano town, a chemical industry, the Solvay Chimica Italia, which from 1970 to 2007 used a Hg cell chlor-alkali (MCCA) technique (dell'Ambiente ITALIA [2010])) discharging Hg directly into the sea. In this situation, we investigated a possible correlation between this very high level of Hg and the industry. Although the Hysplit map shows that over a large scale the backward trajectories were coming from the open sea (Fig. 4.11a), we identified that the highest values had brought from wind coming from the industry area and, precisely, from the north-easterly

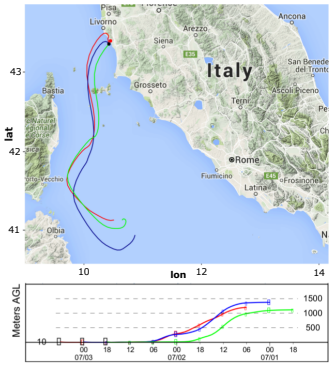

(a)

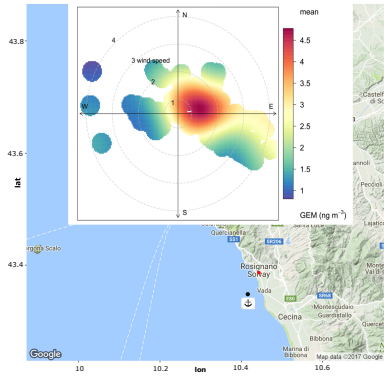

(b)

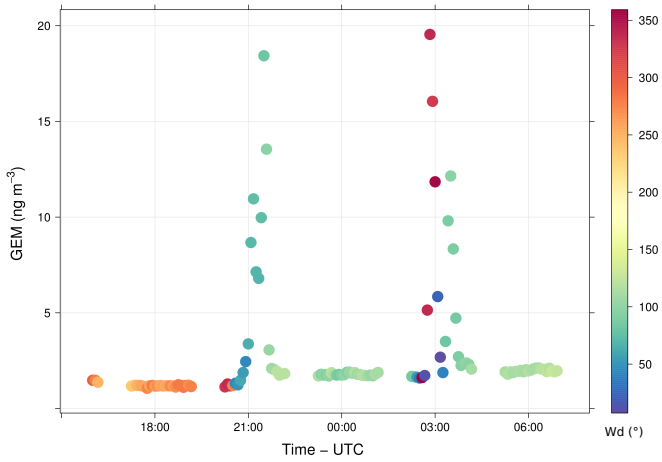

(c)

Figure 4.11: Backward trajectories (Hysplit) at the ship position (black point) and location of the Solvay industry (red points) (a), GEM Wind Rose during S5 (b), GEM time plot with colors identifying the wind direction (Wd) for July, 2^{nd}-3^{rd} (c).

sector. This occurrence, happened during S5, was also highlighted by the GEM rose wind (Fig. 4.11b). Furthermore, the source of air masses

was confirmed by the Potential Source Contribution Function (PSCF) map, calculated for the GEM trajectories ending at 8:00 UTC of July, 3^{th}, that showed a high probability for trajectories coming from the industrialized coast (Fig. 4.12). The PSCF map included 18 trajectories, each started after 1 hour, for the 18 hours of stopping. Moreover, the wind direction of source, was also highlighted by the GEM rose wind (Fig. 4.11b). The GEM rose wind was realized with the GEM 5-min data of this stopping. For each wind direction bin, the mean values of GEM were calculated and represented. Moreover, the GEM time plot shows that the peaks happened when the wind blew mainly from $45° - 120°$, where the industry of Solvay was set (see Fig. 4.11c). A further peak was recorded when the wind blew from $330° - 360°$, in correspondence of which, an inversion of wind direction occurred. At the same way, we deduced that the peak for the other species of Hg (GOM and PBM) are due to the industry. GEM value here recorded resulted higher than previous measurements made during an oceanographic campaign in the same site (about 2 ngm^{-3}, during fall 2007, (Bencardino et al. [2013])). A comparison of results obtained with a previous campaign conducted on land, near the plant of Solvay Chimica Italia has been made (Gibičar et al. [2009]). In previous campaigns measured TGM instead of GEM, and obtained values ranging from 8.0 ngm^{-3} to 8.7 ngm^{-3}, with peak until 100 ngm^{-3}. The higher values could be explained with the closeness to the plant of Solvay Chimica Italia (Gibičar et al. [2009]). Similarly, the GOM peak for this site is significantly higher than the previous oceanographic campaigns (about 4 pgm^{-3}) (Bencardino et al. [2013]), but significantly lower than values reported during a campaign on land (277-691 pgm^{-3}) (Gibičar et al. [2009]); instead the PBM peak recorded is in accordance to the measurements made on board of the research vessel in previous campaigns (5-9 pgm^{-3}) (Bencardino et al. [2013]), whereas close the industry the campaigns showed presented values higher (about 25-70 pgm^{-3}) (Gibičar et al. [2009]).
The O_3 for the entire time of anchorage was 45.4 ± 13.7 ppb, not very high, although we had considered that the stop was nocturnal. Indeed, for the all day before the stop including the stop itself, the maximum

daily 8 hr O_3 mean exceed the limit value of about 60 ppb. Therefore, the massive presence of O_3 in this area was explained with an important production of O_3 precursors, NO_x (see Table 4.2), produced by anthropogenic activities.

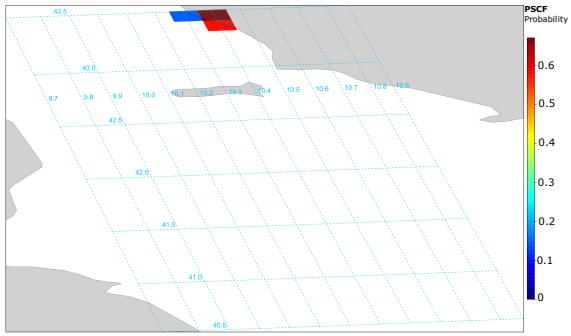

Figure 4.12: PSCF probabilities for GEM concentrations (90th percentile) at S5.

Volcanic emissions in the Aeolian area (R11 - S11 - R12)

Significant research has been published over the last 10 years demonstrating the importance of emissions from volcanos (Friedli et al. [2003a], Gustin [2003], Gustin et al. [2008]) and the potential impact that both cataclysmic volcanic eruptions and quiescent degassing and moderate eruptions as well may have on Hg global and local/regional budget throughout the injection of volatile Hg into the atmosphere influencing its cycle also for a few years with long-term effects on environments (Schuster et al. [2002], Bagnato et al. [2007]). On regional scale, as is the case of the Mediterranean Sea basin, a persistently active volcano may act as an important local point source (e.g. emissions from Etna or Stromboli volcanos, Sicily). Considering the Hg sampling for the whole hot-spot (R11-S11-R12), the mean value was 1.4 $\pm$0.1 ngm^{-3} (n=17) for GEM, 21.9 $\pm$ 29.4 pgm^{-3} (n=17) for GOM, and 1.3 $\pm$ 1.2 pgm^{-3} (n=17) for PBM. During our research cruise, when the research vessel was in proximity of Stromboli volcano, we detected an

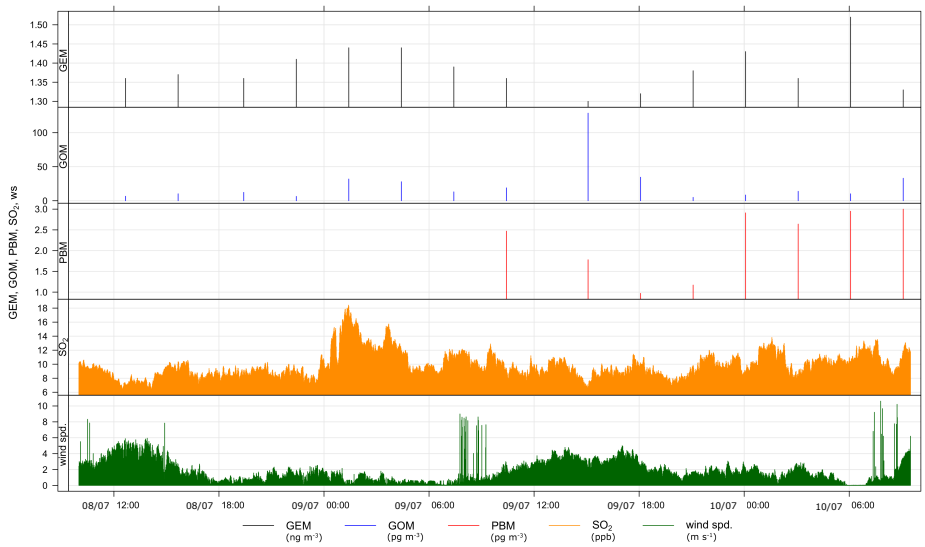

Figure 4.13: Time series for GEM, GOM, PBM, SO_2, Wind Speed, during R11 - S11 - R12.

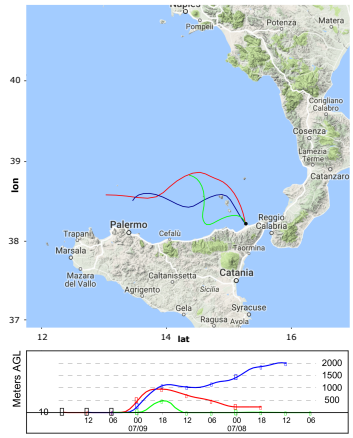

Figure 4.14: Backward trajectories (Hysplit) at the ship position (black point), ending at 18:00 UTC of July, 9^{th}.

increase of GOM at night (from 00:00 to 06:00 UTC, of July, 9^{th}, with a peak of about 30 pgm^{-3} at 01:25 UTC). We suppose that this increase was due to volcanic emissions, like confirmed by an increase of both SO_2 and GEM (von Glasow [2010]). Moreover, by the theoretical model (von Glasow [2010]), GEM could be rapidly converted in GOM and PBM. The values of PBM recorded were lower than MDL because there were a major concentration of coarse particulate emitted by volcanos, so Hg could be associated to it. There are currently many difficulties in quantifying the Hg flux from volcanic emissions due to the spatial and temporal variability in the activity from one volcano to another (Ferrara et al. [2000], Bagnato et al. [2011]), or from different emission points on the volcano (Bagnato et al. [2007]). Due to the logistical restrictions of acquiring measurements at volcanos (difficulty of access, limited power supply, etc.), Hg measurements often only comprise few data points and the related Hg emission current estimates show a large variability which partly reflects the complexity of the chemical and physical processes that Hg undergoes while interacting with the atmosphere. During the day of July 9^{th} (at 15:05 UTC), we recorded the highest value of GOM, about 128.7 pgm^{-3}, concerning the 2 hr of sampling relative to the route from Stromboli to Milazzo, passing near Volcano island, which was degassing, followed by a peak of about 35 pgm^{-3}. In the morning of the following day (9:05 UTC, of the 10^{th} of July) another peak of about 30 pgm^{-3} was recorded. As Fig. 4.13 shows, the highest GOM peak corresponded to a decrease of GEM that probably was converted to GOM and PBM (mainly in the coarser size fraction); it was also favoured by a lower concentration of SO_2, which less affected GOM reduction, as well as by a higher wind speed, which resulted in a major dilution (von Glasow [2010]). The Hysplit map, calculated in Milazzo (see Fig. 4.14), shows that the backward trajectories were coming from the Aeolian islands, therefore, the air mass measured was influenced by volcanic emissions too. In the whole area, since the starting from Marsili station to the leaving of Milazzo, the values of SO_2, tracer of volcanic emissions, were significantly higher than the other regions (see Table 4.2). In the volcanic area the SO_2 levels were about 10 ppb (9.8 ± 1.9 ppb) over a value of

about 7 ppb (7.4 ± 2.0 ppb), this last value being computed as mean of the whole SO_2 dataset recorded during the campaign without considering the values measured in the Aeolian area. Furthermore, the Hg/SO_2 mass ratio in this area was about $5.4 \cdot 10^{-5}$, which is compatible with the other classification of passively degassing volcanos (Pyle and Mather [2003]).

4.4 Conclusions

Measurements of atmospheric Hg were performed aboard the RV "Minerva Uno" of the Italian CNR during an oceanographic campaign conducted in the summer of 2015. The campaign aimed to assess how Hg species concentrations in the Western Mediterranean MBL change in relation with specific source influences. Meteorological parameters and other trace gas levels (O_3, NO_x, SO_2) were also collected and examined to support the discussion on the most likely Hg source attribution and on the main Hg driving mechanisms. This set of measurements contribute to grow the database regarding Hg speciation in the atmosphere, especially in the Mediterranean region, where Hg is an ubiquitous pollutant and temporal variation has an extremely important role in its cycling. Results herein presented are in agreement with previous measurements, both in values and in variability over time, performed in the framework of the MEDOCEANOR on-going program in the Mediterranean Sea basin. During the measurements campaign we identified a number of events in which the concentrations of at least one of the atmospheric Hg species or of the chemical parameters increased notably beyond their average campaign values. In total five events with distinct peaks in the O_3 and GEM concentration in combination with either GOM and PBM, or both, have been observed. With the support of meteorological variables, NO_x and SO_2 data, and others information gained by free tools, we were able to identify the most likely influencing sources, both anthropogenic and natural. Specifically, higher NO_x levels, reaching values above 177.7 ppb were encountered on-shore, whereas lower concentrations, until 0.5

ppb, were detected off-shore and far from potential influencing sources. Within our hot-spots, the anthropogenic influence was observed twice and in both cases it was of industrial origin. Natural influences was also detected twice but with different origin: wildfires and volcanic. Data on SO_2 were otherwise useful to compute the Hg/SO_2 mass ratio for the volcanic area that resulted to be about $5.4 \cdot 10^{-5}$, compatible with the classification of passively degassing volcanos. Knowledge of the contribution of volcanic degassing systems and geothermal fields to the global budgets of Hg in the atmosphere is therefore essential to evaluate the role played by volcano systems on the Hg cycle. In addition, GEM and GOM species in volcanic gas plumes as well as the ratio of gaseous to particulate Hg forms, have rarely been determined in a systematic way. Further measurements close to volcanos are therefore essential to better understand the mechanism of Hg species in volcanic plume, in order to give important contributions to validate theoretical models (von Glasow [2010]). Among natural and industrial influence we also detected a specific reaction mechanisms occurring between halogen and GEM, favoring the so called *in-situ* GOM production, during which we observed a decrease in GEM values followed by a grow in GOM concentrations. Our observations corroborate studies previously performed on this issue that suggest a lifetime of GEM significantly shorter than 12 months in the MBL. It would also imply that marine emissions of GEM are at least in part, directly recycled to GOM in the MBL and redeposited to the oceans. Our findings highlight that the natural contribution of sources on Hg levels within the Mediterranean basin should not be considered negligible.
A deep analysis regarding the size distribution of PBM is essential to better understand processes of Hg in presence of particles in the coarser fraction, like those especially linked to natural sources and mainly present in the Mediterranean basin, such as volcanic emissions, and sea spray. A future study focusing on the coarse fraction of PBM would be very interesting also in view of the fact that PBM-coarse is heavier than PBM-fine and therefore we attend a higher deposition velocity, with major input causing a worse effect on environment.

Chapter 5

Development of new Sensor Technologies for Atmospheric Mercury Measurements

5.1 Introduction

Recently, global traceability and measurements of mercury have been addressed with a network approach using automated and/or semi-automated systems for sampling and detection of Hg in air and wet deposition. Based on the commonly used procedures for the determination of mercury in ambient air within the GMOS global network, the corresponding costs to run more than 40 monitoring sites are extremely high, especially in remote regions such as Antarctica or in pristine areas that do not have a basic infrastructure (i.e., no clean labs, poor power supply) as well as trained operators. This situation clearly increases the need to develop technologies and new sensing systems for rapid Hg detection at lower operating costs. On the long term, the management sustainability of global or continental scale monitoring networks for measuring mercury in ambient air depends very much

on our ability to develop advanced sensor capacities to collect total mercury concentrations or even better if this can be done for speciated mercury concentrations (GOM and/or PBM). These sensors should be robust, traceable and should not require either a gas carrier, a significant energy supply or highly qualified technical expertise.
This Chapter provides a report on the development of a prototype sensor for atmospheric mercury measurements (TGM/GEM) in ambient air which will be field tested and validated later on in this project employing the GMOS sites worldwide. It focused in particular on the development of components for a TGM passive sampler including a collection surface, diffusive housing, and an external shield. Important goals for the final product were a system inexpensive to manufacture, simple to analyze, easily shipped and deployed, which could be handled and transported without contamination.

5.2 Passive air sampler (PAS) as a tool for long-term Hg air pollution monitoring

Passive samplers present a means of addressing many issues in atmospheric chemistry monitoring, providing a simple and cost effective way of monitoring specific species in hazardous and extreme environments at regional and global scales, and therefore offer broad capacity building opportunities. While the appropriateness of the use of passive samplers has been questioned in the past due to concerns related to reliability and accuracy, current developments and studies indicate that passive samplers are now a viable option for many species and many applications are becoming an effective alternative for conventional active samplers in exposure and health effects studies due to their simplicity (having no moving parts) and portability (smart), whereas also no electricity, pumps or other supporting equipment is required. Furthermore, they are simple to use (no human intervention - non-'expert' based systems) and inexpensive. The low cost of the materials allows

Figure 5.1: Simplified scheme of a passive sampler.

for sampling at multiple locations (Global Network). They have been designed to give information about the average Hg pollution levels over time periods of few hours to weeks/months providing comparable performance to active samplers in terms of sensitivity and reproducibility.

5.2.1 Basic Principles and Passive sampler materials

The sampling technique is based on the property of molecular diffusion of gases, hence the term "passive sampling" (also referred to as diffusive). Gas molecules (i.e., Gaseous Elemental Mercury) diffuse through a diffusive surface into the sampler where they are quantitatively collected on an impregnated filter or an absorbent scaffolding. Thus they achieve a time-integrated (or average) concentration. A passive air sampler consists, in fact, of a collection surface (absorbent material) that has a high affinity for the chemical of interest (in this case, Hg) and a method to eliminate turbulence and create a region of stagnant air between the ambient atmosphere and the collection surface where only diffusion occurs. Gas molecules are collected by passing through a diffusion barrier (usually an entrapped air volume that keeps the sampling rate constant), slowly diffusing through the region of stagnant air and sorbing to the collection surface. Fig. 5.1 shows a simplified scheme of a passive sampler.

If the sampling efficiency is sufficiently high, then the sampling rate can be calculated using Fick's first law of diffusion from the cross sectional area perpendicular to the transport direction and the distance

that the gas has to diffuse. Therefore, following Fick's Law:

$$Q = D \cdot K$$

where the sampling rate (Q) is a function of the diffusion coefficient of the analyte (D) and the geometric constant of the sampler. The diffusion coefficient (D) always remains constant for a given analyte, therefore, to improve the sampling rate (Q), the geometric constant (K) must be improved. The geometric constant is:

$$K = S/l$$

where (S) is the diffusive surface and (l) the distance between the diffusive and adsorbing surface. To work properly (and quantitatively) it is essential that the transport occurs solely by molecular diffusion and that no gas is lost to the walls of the sampler. Under these conditions the sampling rate, and thus the concentration range of the sampler, is directly proportional to its cross sectional area and inversely proportional to its length. Furthermore, since the rate of molecular diffusion depends on temperature (through temperature dependency of the molecular diffusivity), the average sampling rate (sorbed amount per unit time divided by the ambient concentration) is a temperature dependent constant for a given species and sampler. The samplers are very easy to manufacture. Specifically, the sampler prototype was manufactured in borosilicate glass material with teflon material components. The body of the sampler is a cylindrical glass vial (inner diameter of 2.04 cm, length 2.54 cm) (Fig. 5.2) with a teflon screw cap at one end. There are two screw caps: one "screw cap opened" in the middle used during the sampling time and one "screw cap closed" employed before and after the sampling period.

To avoid turbulent diffusion inside the vessel during exposition, the open end cap contains a thin-film with an anti-convection porosity. This mesh/membrane consists of a fine micro-porous nylon screen placed at the inlet end. They are also very cheap to manufacture and all components, including the quartz coated filter (passive membrane),

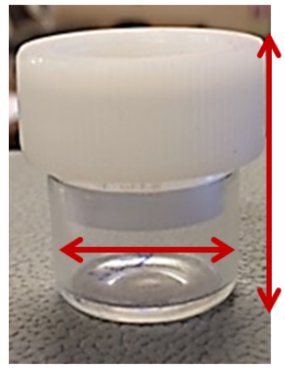

Figure 5.2: Body of the sampler prototype.

which can be thermally regenerated and reused for further measurements after the desorbing phase. Supporting rings keep the passive membrane in position within the vessel. The membrane consists of a quartz coated filter (thin layer of the nanostructured material) placed at the bottom of the vial. The success of a diffusion sampler rests critically on the collection efficiency of the impregnated filter. A passive membrane which selectively and quantitatively absorbs the targeted species, while other pollutants do not interfere, is needed for passive samplers. This is the key factor which determines which species are suitable for passive sampling. Fig. 5.3 and Fig. 5.4 show all material components of the prototype sampler sensor and the passive membrane sealed into the sampler housing, respectively.

5.2.2 Nanoparticle (NP) Film Preparation

Within the PhD work has been investigated the chance to design absorbing material based on either nanofibers or nanoparticles, due to the shape, size and peculiar geometry of these structures. Electrospinning is a method of electrostatically depositing polymer nanofibers onto an object by applying a high voltage to a liquid polymer solution. Using collection surfaces of various shapes and sizes as scaffold, this technology can produce standalone materials and devices, or can be

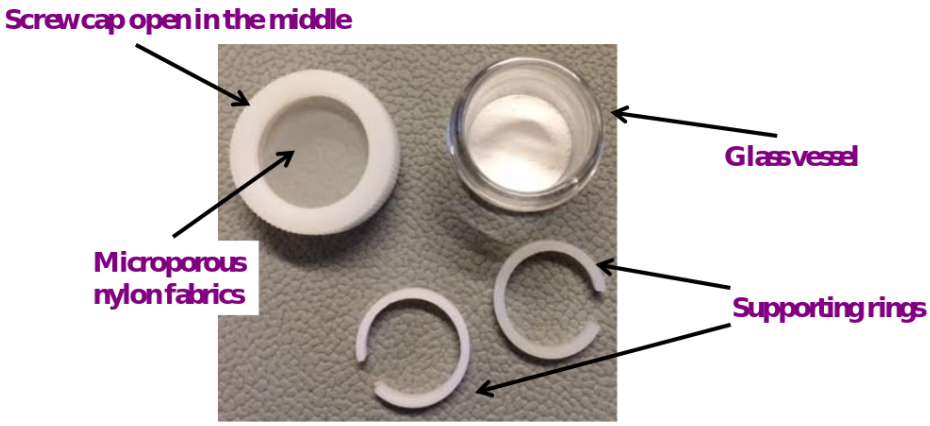

Figure 5.3: Material components.

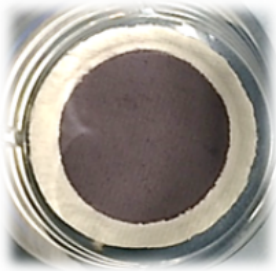

Figure 5.4: Top view of the passive membrane sealed into the sampler housing.

used to coat nanofibers onto existing materials and devices. Electrospinning technology has been commonly used to design highly efficient filtering system, also for mercury in air as well as in water. Nowadays fibrous membranes have been used in different filtration applications (respirators for citizens, industrial gas cleaning equipment, air purifiers for cars, cleanrooms, indoor environments, etc.). Depending on the application, the technology allows creating nanofibers made of a wide variety of materials, such as cellulose, glass, plastics, ceramics, metals or composites. It is known that conventional fibrous structures suffer from many structural disadvantages, like large fibre diameter,

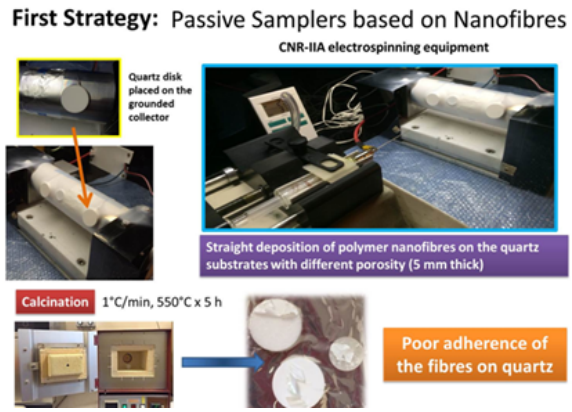

Figure 5.5: First strategy of designing and developing passive samplers for mercury in air based on electrospun nanofibers.

non-uniform fibre diameter and pore size, low filtration efficiency and poor high temperature resistance. On the other hand it is well documented in literature that the smaller the fibre diameter, the better the filtration performances. In order to design proper adsorbing layer for mercury based on electrospinning, CNR-IIA developed a series of fabrics based on nanofibers of titanium oxide properly functionalized with gold nanoclusters, since similar structures exhibited, as filtering systems, the highest Hg^0 removal efficiency (100%) when compared to other nanofibrous systems. Quartz disks, having two different porosities (45 and 450 μm, respectively) were provided in order to withstand the high temperature (550°C) of the process of fibers calcination (oxidising and crystallization of TiO_2). They were easily coated with a non-woven layer of polymer nanofibers (precursor of TiO_2) through electrospinning technology and then subjected to annealing in an oven (Aprolab, 1°$Cmin^{-1}$, 550°C x 5 h). Different strategies have been followed during this work. The process and the results are reported in Fig. 5.5.

During the thermal treatment, fibres shrivelled and detached themselves from the substrates of quartz, making vain the proposed strategy. However since a polymer free standing fabric was obtained too,

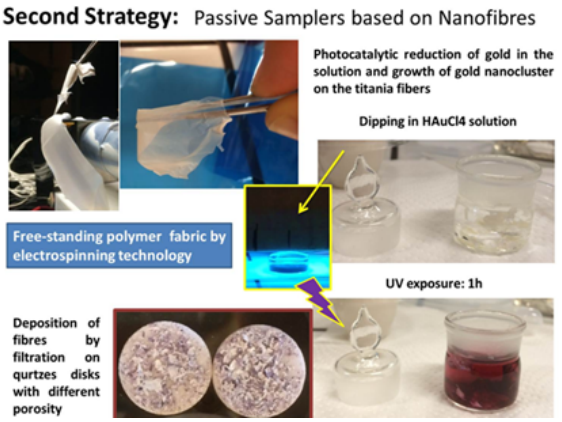

Figure 5.6: Second strategy of passive samplers preparation based on free-standing electrospun fibres of titania and following procedure of photocatalytic functionalization with gold nanoparticles.

a second strategy was proposed. Therefore the fibrous scaffold was annealed and then successfully functionalized under UV irradiation (1 h) in a suitable aqueous solution comprising a capping agent (PVP, 0.1 M) and $HAuCl_4$ (Tetrachloroauric(III) acid, 0.5 $mgml^{-1}$). The process is depicted in Fig. 5.6. Fibers were fragmented and filtered using as substrates the quartz disks with different porosity. After slow heating and drying in an oven ($1°Cmin^{-1}$, $110°C$, 24 h), fibers resulted well attached to the substrates and usable as passive sampler. However the absorbent material appeared poorly reproducible and uneven distributed on the quartz surface.

The third strategy proposed to design absorbing material based on composite nanoparticles [titanium oxide (TiO_2) properly functionalized with gold nanoclusters] that due to the shape, size and geometry of these structures hugely improve the diffusive surface. The preparation of a passive sampler based on this sensor technology resulted in a simple and economical approach because titania nanoparticles are available on the market (Sigma Aldrich, Titanium (IV) oxide, anatase, $\leq$ 25nm diameter) and are easier to handle and deposit on various substrates. In addition, the calcination process is not required any longer,

which results in additional energy savings. Therefore, 500 mg of Titanium (IV) oxide (anatase) (Sigma Aldrich, CAS 1317-70-0) has been suspended in an aqueous solution of PVP/$HAuCl_4$ (0.1 M PVP, 0.5 mg/mL $HAuCl_4$) for the preliminary investigations. Such a suspension was UV-irradiated for 1 h, thus changing the colour from yellow to blue-violet (shown in Fig. 5.7 and Fig. 5.8). A series of thinner quartz slices (500 μm thick) were dipped in such a prepared suspension overnight and then removed, dried (150°C) and weighed (an average of 150 mg per sample). The layers looked homogeneous and adhering to the substrates. Each quartz disk could easily be handled and housed in the commonly used exposure glass chambers (Marbaglass, Italy) for VOCs and gases passive sampling. Nanoparticles were analyzed by a UV-Spectrometer Shimadzu 2600 before and after gold nanofunctionalization, confirming the gold reduction and adhesion on the surfaces of the titania NPs and suggesting, according to literature results, a very small diameter (under 20 nm) of AuNPs. These novel structures are promising to develop a very attractive passive sampling system based on both the strong affinity between mercury and gold and a wide adsorbing surface due to the nanosize of the materials (expected high efficiency and lifetime).

5.2.3 Hg passive sampling: the sequence

The average concentration at the measurement site over the time period that the sampler is exposed to ambient conditions is determined by chemical analysis of the passive membrane. Passive samplers are analyzed directly by thermal desorption at 550°C by CVAFS (Cold Vapor Atomic Fluorescence Spectrometry). The lower detection limit is commonly defined as 2 to 3 times the standard deviation of the blanks. The laboratory blanks are stored in the lab and periodically tested. Thus, procedures and improvements which reduce the standard deviation of the blanks result in significant improvements in the lower detection limits of the samplers. The repeatability of the results is quantified and checked by use of duplicate samples. Fig. 5.9 shows

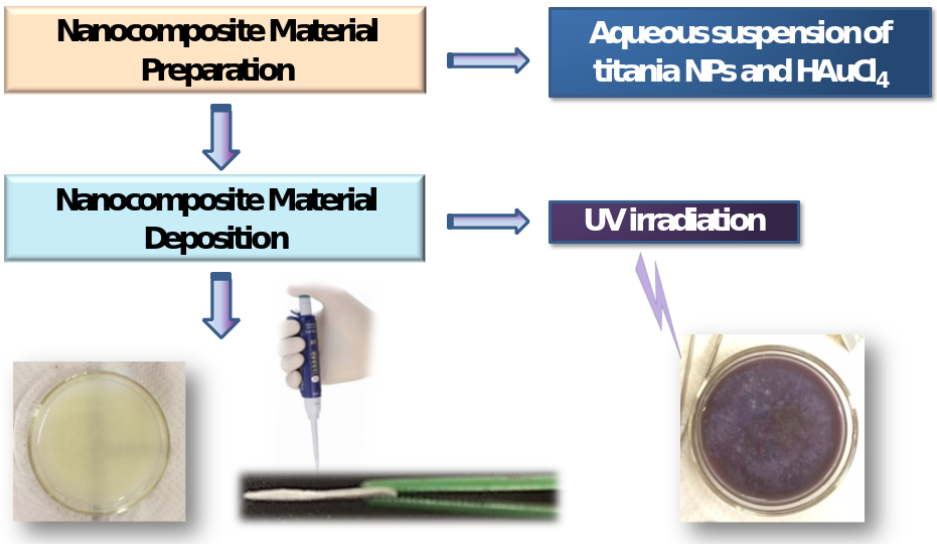

Figure 5.7: Nanocomposite material preparation, deposition on the quartz filter surface and 1h - UV irradiation process.

examples of couples of PASs desorption step, and both graphics reported in the figure highlight the peak concentration obtained exactly after 5 min of the desorption time.

Fig. 5.10 shows laboratory experiments of exposure of a number of passive samplers into the exposure glass chamber in the laboratory and a simplified scheme of the diffusion process and amalgamation on gold-nanoparticles of the passive membrane. On the other hand, Fig. 5.11 shows the typical deployment of passive samplers in the field for the scheduled exposure time after having carefully placed them into the designated shelter seat, with the diffusive layer facing the air (i.e. the opened screw cap down).

It should be emphasized that they provide time integrated concentrations with continuous time coverage, with the averaging time determined by the period they are exposed to ambient air, which can be daily, weekly, monthly, etc..Therefore, they are obviously not well suited for monitoring temporal variations over short time intervals, or

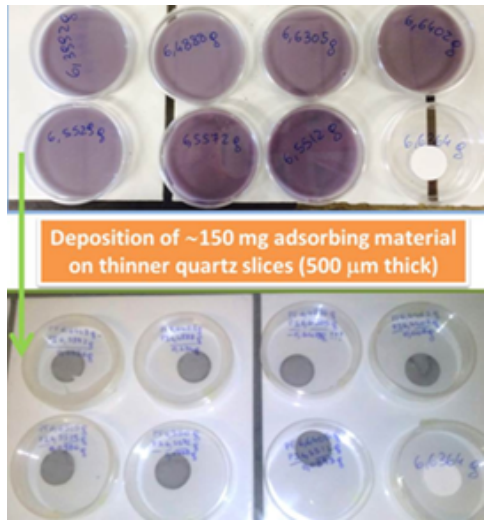

Figure 5.8: Example of passive membranes prepared for the passive samplers.

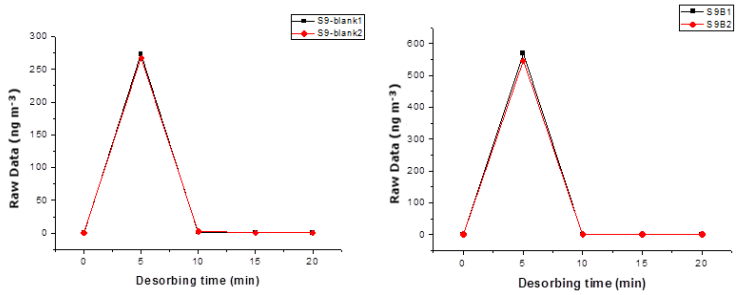

Figure 5.9: Examples of couples of PASs desorption step.

for detection of individual peak values, or when real-time measurements are needed.

Adsorption and desorption processes of mercury (calibration and validation) in atmosphere are actually matter of investigation. A prototype of thermal desorption system was also planned at the CNR-IIA and developed in order to be connected to the most commons analytical systems of mercury. The prototype was manufactured in quartz

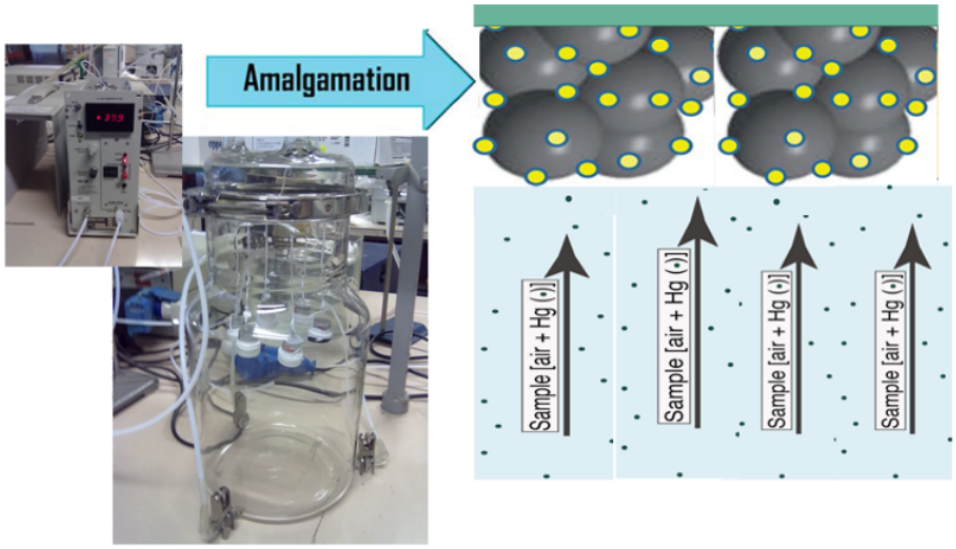

Figure 5.10: Exposure of a number of passive samplers into the exposure glass chamber in the laboratory and a simplified scheme of the diffusion process and amalgamation on gold-nanoparticles of the passive membrane.

and housed in a heater system to allow the fast desorption of the Hg adsorbed on the thin layer of the nanostructured material, flowing ultrapure gas (argon) and/or Zero Air throughout the desorption chamber. A picture of the thermal desorption prototype is reported in Fig. 5.12.

5.3 Electrospunnanofibres of AuNCs/TiO_2 for novel sensors of elemental mercury in atmosphere

In the present research work, hybrid nanofibrouselectrospun layers of TiO_2 coating Pt micro-resistors were suitably designed in order to create nanostructured 3D-frameworks, potentially capable of adsorbing

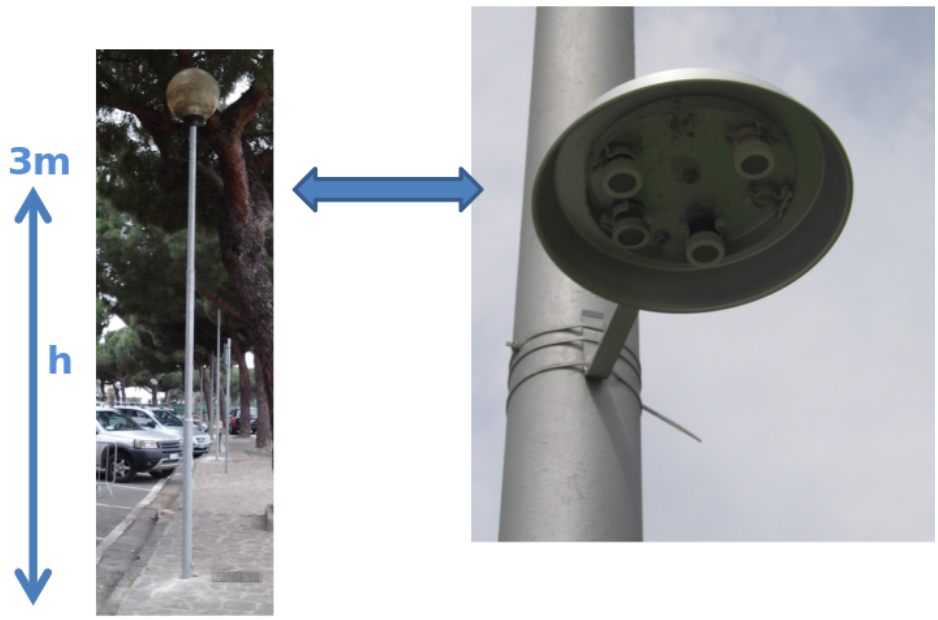

Figure 5.11: Typical deployment of passive samplers in the field. On the right, passive samplers mounted under a rain shield.

and revealing elemental mercury vapors in the atmosphere. Indeed, exploiting the outstanding photocatalytic properties of the nanofibers of titania, gold nanoclusters were selectively grown, under UV-light irradiation, on the electrospuntitania nanofibers through the photocatalytic reduction of $HAuCl_4$ (tetrachloroauric acid) in the presence of an organic capping reagent. Due to the uniqueness of the resulting nanostructures (high surface to volume ratio, high fibre interconnectivity and nano-scale interstitial spaces) and for production rate and cost, the planned sensors were expected to be promising candidates for elemental mercury detection in traces. An electrospinning solution ($7.877 \cdot 10^{-5}$ M) was prepared according to literature by dissolving polyvinylpyrrolidone (PVP, Mn 1,300,000, Aldrich) in anhydrous ethanol (EtOHa, Aldrich) and stirred for a few hours. A solution of titanium isopropoxide (TiiP, Aldrich, 1:4 (w/v)) solved in a 1:1 (v/v)

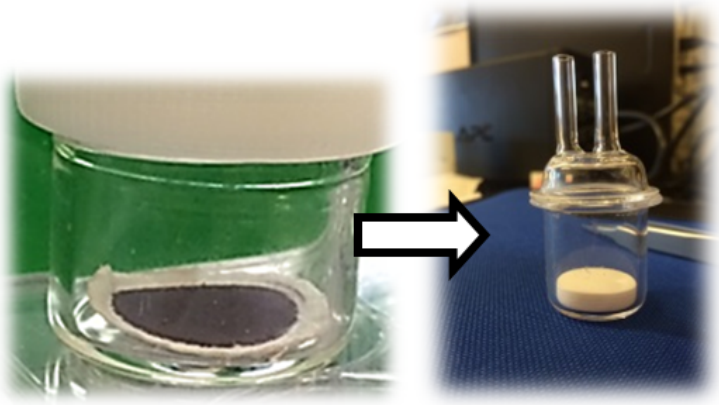

Figure 5.12: A prototype of the desorbing thermal quartz chamber.

mixture of glacial acetic acid (AcAcg) and EtOHanh was freshly prepared and added to 2.5 ml PVP solution under stirring (clear yellow solution). Both mixtures were prepared in a glove box under low humidity rate (<7%, obtained under continuous N2 flow rate). The polymer solution was then transferred into a glass syringe equipped with a 24-gauge stainless steel needle (din = 0.0122 in., purchased from Hamilton). The syringe filled with the TiiP/PVP solution was fixed to a syringe pump (KDS 200, KD Scientific) working in horizontal direction and perpendicular to a 15 cm far grounded rotating cylindrical collector (45 mm diameter). The syringe needle tip was connected to a positive DC-voltage. The selected feed rate was 100 ml/h and the applied voltage was 6 kV. The substrates were fixed, through a suitable holder, to the collector surface (600 rpm, 21°C and 35% RH) and the deposition time was set to 20 min. Fibres were annealed under oxygen atmosphere using a thermal ramp from room temperature up to 550°C ($1°Cmin^{-1}$, 4h dwell time) in order to remove PVP and proceed to crystallize the metal oxide (anatase). The resulting fibrous layers were immersed into an aqueous solution containing $1.5 \cdot 10^{-3}M$ tetrachloroauric acid ($HAuCl_4$) and 0.1M PVP (as capping agent).

The substrate was then irradiated with UV light for specified intervals. A long-wave UV lamp (365 nm) (Helios Italquartz) was used as the UV light source. After UV irradiation for a specified interval, the samples were rinsed with copious amount of water and dried in air. The samples on silicon wafers were directly employed for scanning electron microscopy (SEM) and atomic force microscopy (AFM) imaging. SEM images were taken using a scanning electron microscope (SEM Jeol, JSM 5200, 20keV) operated at an accelerating voltage of 5 kV;AFM micrographs were taken through NanosurfFlexAFM, tapping mode 190Al-G, 190 kHz, 48N/m. The transducers were interdigitated electrodes (IDEs: 40 pairs of electrodes, 150 nm thick, 20 μm width electrode, 20 μm gap) designed and manufactured in CNR-IIA (Italy) on oxidised silicon wafer through a standard photolithographic process (lift-off procedure) then followed by Ti sputtering and Pt evaporation. Each chemoresistor was placed in a suitable case made of PTFE and connected to an electrometer (Keithley 6517 Electrometer) capable of measuring the current flowing through the IDE, when a fixed potential was applied to it, and to send data to a PC. In order to test the responsiveness of the device to lower Hg concentration, a dynamic permeation tube was set up to dilute the mercury-saturated gas to the concentration range of interest, by using a mass flow controller system (4-Channel-MKS 247). The final Hg^0 concentration (measured by Tekran2537A) was obtained by tuning the oven temperature and the dilution flow. Specifically, titania fibers (100 nm mean diameter) were decorated with gold nanoclusters (AuNCs) (Fig. 5.13a) induced to grow selectively upon photocatalytic reduction of $HAuCl_4$ caused by UV light irradiation. Similar structures planned for electrospunnanofibrous filters and catalytic systems, were produced in literature to create novel abatement systems for Hg. They reported an efficiency of about 100%. The morphology and size of gold nanoclusters, as well as the coverage of fibers, depended on UV irradiation exposure (Fig. 5.13b-c). When the samples were UV irradiated for 1 hour, fibers were completely covered with Au particles (confirmed by SEM microanalysis, data not shown) with globular shape merged together and with numerous protruding budding, densely clustered and overlapping (SEM

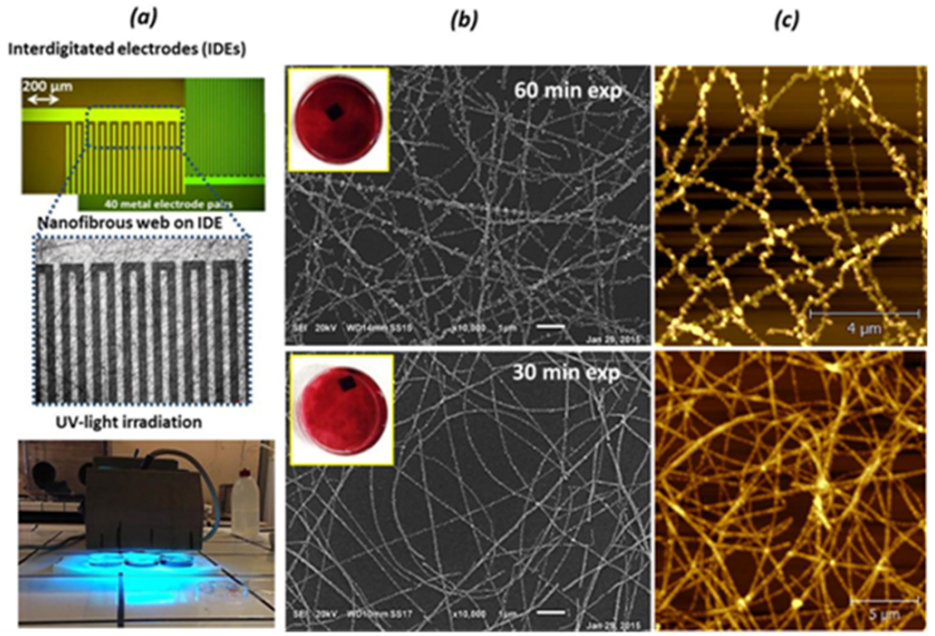

Figure 5.13: (a) Optical micrographs of the electrodes before(top) and after electrospun deposition (in the middle) and a picture of the samples (down) in solution and under UV irradiation; SEM (b) and AFM (c) micrographs of titania nanofibers after 60 min and 30 min of UV exposure, respectively. The chemical reaction can be monitored by the color change of the solution (colorless > orange > red > purple).

and AFM micrographs in Fig. 5.13). On the contrary when fibers were exposed to UV irradiation for a shorter time (30 min), they appeared more homogeneously coated with round-shaped nanoparticles.

The sensors coated with both structures showed Ohmic behavior in air and at room temperature (Fig. 5.13), but with different resistance values depending on the quality of the coverage, as expected. The most common electrodes used for manufacturing conductometric sensors are interdigitated electrodes (IDEs) that are implemented over insulating and flat substrates (like alumina, silicon dioxide wafers, etc.) in various geometrical layout (one or several pair of electrodes) using

photolithography and metal deposition techniques. A constant potential is applied and the output signal strength of IDEs is controlled by the design of the active area, width and spacing of the electrode fingers. The resistance value depends on both the quantity and quality of the texture covering the electrodes, such as fibre density, shape and dimension of fibres (individual resistance value) assembled over the electrodes (aligned, nonwoven, etc.). The sensor measurements, that were the electrical signals reported when interaction between the sensing layers and the analytes were happening, resulted in a change of the whole resistance (or current, i.e. I=V/R according to Ohm law) of the device according to the following rule:

$$R = \frac{1}{2N-1}\rho\frac{w}{hL}$$

where (N) and (L) are number and size of the fingers, (h) the electrode thickness and (r) la resistivity of the overlying material. We reported the preliminary results related to sensors coated with 1h UV-irradiated fibres (the most conductive sensors, R=580-650Ω). Oxygen and relative humidity did not affect the electrical parameters of the sensors, thus comparable electrical features were reported when measurements were carried out under nitrogen or air (Fig. 5.14, on the left) and increasing percentages of relative humidity (Fig. 5.14, on the right). Firstly, the chemosensors were exposed to water vapours ranging between 10-70% RH. The relative humidity percentage was measured through a commercial sensor, placed inside the measurement chamber, confirming the achievement of the equilibrium one minute after the start of measurement.

Secondly vapor of mercury were flowed throughout the measuring chamber housing the sensor. The strong affinity and specificity of Au for Hg^0 explain the sensitive responsiveness of Au nanoclusters (AuNCs) on the nanofibrous scaffolds to mercury, highlighted by the current changes of the sensors upon Hg adsorption. In detail, sensors exposed to mercury vapours, pointed out a decrease in current, and the slope of the electrical signals seemed to be dependent on analyte concentration. When a sensor was exposed overnight to high

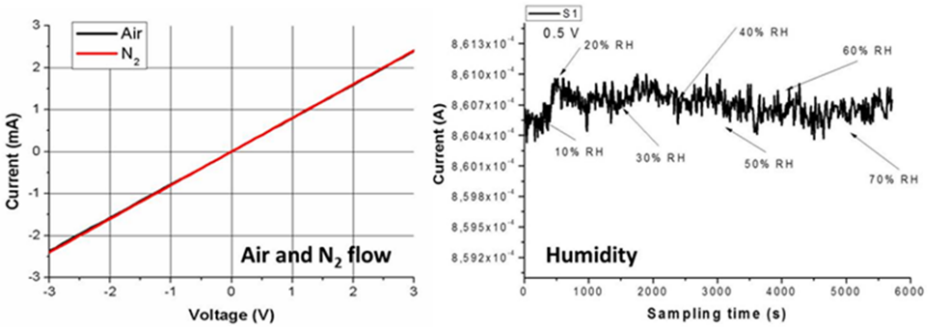

Figure 5.14: (On the left): Current-Voltage curve of one sensor 1h-UV-exposed sensor under air (black line) and nitrogen (red one) flow; (on the right) sensor transient response (current) to increasing percentage of relative humidity (10% - 70% %RH) (0.5V).

concentration of Hg ($PV = 1.6 \cdot 10^{-3} mbar$), its resistance changed by 30% (Fig. 5.14a). In order to test the responsiveness of the device to lower Hg concentration, mercury vapours were flushed, from a dynamic permeation tube, throughout the measuring chamber. The final Hg^0 concentration was obtained by tuning the oven temperature and the dilution flow. Preliminary results showed that the exposure of a sensor to 7.5ng/l of Hg resulted in a decrease in current, with a rate of ∼109 nA/min (+2V) and a limit of detection about 0.18 ng/l (LOD: three times the standard deviation of the blank) (Fig. 5.14b). Quick thermal shots restored sensors, due to the high porosity of the layer and the extremely reduced size of the gold nanoclusters. Exploiting the excellent photocatalytic properties of the nanofibroustitania, the sensing layer was decorated by gold nanoparticles (AuNPs) by immersing the electrospun material, into a solution containing $HAuCl_4$ under UV irradiation. AuNCs played an active role in mercury sensing, increasing the active surface area, improving both diffusion inside the layer and the sensor conductivity. The resulting sensors, functioning in air and at room temperature, showed constant and low level of resistance providing the chance to work at very low voltage values (low power, slow sensor degradation).The response curve of the tested

sensors to increasing concentration of mercury vapor reported a general decrease in current. These attracting sensing features sound as encouraging premises to develop sensors for elemental mercury based on electrospunfibres of gold nanofunctionalized titania.

5.4 Conclusions

The ability of Hg to be re-distributed in the environment through a complex combination of physical, chemical and biological processes, has received increasing attention in recent years and has enhanced the need for a global action in ruling and monitoring its releasing in the atmosphere. Since the need for fast detection systems, at low cost and low maintenance, as well as ease of use are becoming ever more urgent, sensors and sensing systems looked the most promising alternative to the traditional instruments. The mainly sensing strategy has focused on the strong affinity of Hg to gold, and more recently thanks to the advances in nanotechnology, to nanostructured gold materials (such nanoparticles, nanowires and nanorods). In order to design proper adsorbing layer for mercury CNR-IIA developed a series of fabrics based on nanofibers of titanium oxide properly functionalized with gold nanoclusters, since similar structures exhibited, as filtering systems, the highest Hg^0 removal efficiency (100%) when compared to other nanofibrous systems. Thus, gold nanoparticles have been grown on nanofibrous scaffolds of TiO_2 by photocatalysis. Electrospinning technology has been used successfully to create a 3D-framework of titania covering the electrode sensing area of the properly designed chemoresistors (IDEs). By dipping the samples within tetrachloroauric solutions under UV irradiation, the titania layers proceeded the nucleation of gold nanospheres lonely on the fibres. Small changes of $HAuCl_4$ concentration allowed to tune both size, arrangement and distribution of the AuNPs along the fibres. Electrospinning was confirmed therefore to be a very promising nanotechnology for developing smart and ultrasensitive sensing systems, and gold nanoparticles provide a sensing

medium with potential advantages in sensitivity, selectivity, robustness, and cost over established techniques. The nanofibrous layers loaded with more particles resulted conductive at room temperature (Ohmicbehaviour) and suitable to change their current values to low concentrations of mercury vapours (tens of ppt). The easy of deposition (electrospinning) and preparation (UV-irradiation in aqueous solution) as well as the high Hg^0 sensitivity, suggests the chance to investigate the material features by further transduction systems. An encouraging reproducibility in laboratory fabrication of the chemoresistors was obtained (Rm=1.3 $k\omega$). The fabricated nanostructured chemosensors worked as Hg^0 vapours highly adsorbing 3D conductive traps, capable of working until the saturation of all the interacting sites occurred. Depending on the strategy of sampling, the limit of detection could be improved, $\sim$6 ppt when mercury vapor was injected and about 2 ppt when slowly flowed within the measuring chamber. Despite the high sensitivity of the chemosensors to Hg^0 vapour, the responses appeared to be slow. However, a change of the geometry of the vapour jet is expected to improve the adsorption rate and then the sensor responses.

Chapter 6

Comparison campaigns of Hg data between the conventional analyzers and the prototype devices (PASs)

6.1 Introduction

The developed Hg passive samplers, based on composite nanoparticles (titanium oxide (TiO_2) properly functionalized with gold nanoclustershave), have been firstly tested at the CNR-IIA laboratories and planned to share them among the selected GMOS sites in different environmental and meteorological conditions. A detailed plan of sampling campaigns using the passive samplers have been also developed for all GMOS sites involved. In order to test the novel Hg passive device, therefore, the CNR-IIA has involved many GMOS experts and managers of ground-based monitoring sites around the world that perform mercury measurements by conventional instruments to be agreed for performing Hg measurements using the new sensor device developed by the CNR-IIA. In particular, as first exercise, it has been proposed a selection of five monitoring stations established within the

GMOS network, mostly background sites, to undertake passive sampling and analysis of Hg in ambient air in order to strengthen capacity in providing globally comparable data. The list of the sites has been performed and agreed with the GMOS partners in order to plan two seasonal field campaigns in different conditions (i.e., meteorological, geographical etc.). The CNR-IIA, therefore, defined the stations for co-working of passive air samplers for Hg measurements and conventional Hg instruments. The selected GMOS stations at the end of both sampling campaigns delivered the results of continuous Hg measurements related to the period of simultaneous exposure of Hg using active air samplers as well as the passive samplers have been shipped at the CNR-IIA laboratories for subsequent analysis step. The GMOS selected stations included in this study are located in the following countries:

- (Mount Curcio Station, MCU), Italy
- (EMMA station, Bariloche, BAR), Argentina
- (Cape Point Station, CPO), South Africa
- (Mount Ailao, MAL), China
- (Listvyanka Station, LIS), Russia.

6.2 Methodology

6.2.1 Configuration and characteristics of the selected GMOS ground-based sites

This paragraph provides a brief review of principal characteristics of the selected GMOS monitoring stations distributed in the Northern and Southern Hemispheres in framework of the global network. In particular, Tab. 6.1 shows the characteristics of the GMOS ground-based sites reported as "Master" (M) stations where Gaseous Elemental

Mercury (GEM), Gaseous Oxidized Mercury (GOM), and mercury associated to suspended particulate matter ($PBM_{2.5}$) are continuously measured, or as "Secondary" (S) stations where only Total Gaseous Mercury (TGM) is continuously measured.
Listvyanka (LIS). This site is situated at the coastal hill (near Lake Baikal), at the Astrophysical Observatory, about 1 km from the outskirts of the Lystvyanka settlement and 70 km from Irkutsk city. All surrounded hills are covered by forest (mostly pine). At the site there is rocky soil with a thin grass. The site has been part of the East Asia Network for Acid Deposition Monitoring (EANET) since 2000.
Mount Curcio (MCU). The site is a Global Atmospheric Watching (GAW) Climatic-Environmental Observatory located in a strategic and isolated position within the Sila massif, one of the main three areas making-up the Sila National Park, in the South of Italy. It is characterized by no local sources of contamination and no access by road and it is 200 m from a ski resort and from the cable car arrival point of the surrounding ski area. The operative station is situated at 1780 m a.s.l. on a southern Appenine mountain peak with completely free horizon, thus allowing to gain atmospheric monitoring measurements with a large spatial representativeness.
Mount Ailao (MAL). It is located at a summit of the northern edge of the Ailao Mountain National Nature Reserve in central Yunnan province, southwestern China. The reserve has an area of 677 km^2 and is predominantly ($> 80\%$) covered by evergreen broadleaf primary forests. This site is frequently influenced by long-range transport of Hg released from anthropogenic sources and biomass burning in southwestern China, the Indochinese Peninsula, and South Asia.
Cape Point (CPO). The station is located at the tip of the Cape Peninsula (210 m a. s. l.) within a nature reserve. It is surrounded by the ocean. The area has a rocky terrain and is sparsely vegetated. The site experiences moderate temperatures, dry summers with occasional biomass burning episodes in the surrounding area and increased precipitation during austral winter.
Bariloche (BAR). The station is located near the laboratory of photobiology on the shore of the Gutierrez River. The area is a natural

forest (mixed Andean forest, Nothofagus spp. and several species of bushes and grasses) and close to the station there is riparian endemic vegetation (max. 4-5 m height) as wells as a few planted pine trees (> 20 m height).

Table 6.1: Hg statistical summary at GMOS monitoring sites during the first and second campaigns.

Stations	LAT	LON	Elevation (m a.s.l.)	Country	Type	Institute Affiliation
Listvyanka	51,85	104,89	560	Russia	S	SPBSU GAW
Mount Curcio	39,31	16,42	1780	Italy	M	CNR-IIA GAW
Mount Ailao	24,53	101,03	2503	China	M	IGCAS
Cape Point	-34,35	18,49	230	South Africa	S	SAWS GAW
Bariloche	-40,40	-71,42	840	Argentina	M	INIBIOMA GAW

6.2.2 Field Seasonal sampling Campaigns

GMOS experts were contacted in order to undertake appropriate agreements to plan the first campaign. Shipments of technical-scientific material started in December 2016. In particular, for the seasonal sampling campaigns at the GMOS sites, 250 passive samplers have been prepared and shipped. Sampling campaigns have been structured using a much higher number of samplers that have been co-located and exposed for 2 and 3 weeks in parallel; this will allow to cross check the following key parameters for the QA/QC: linearity over time, reproducibility and behavior of samplers at different climate conditions. The sampling campaigns have been scheduled over one month and half during two seasons.
The first sampling campaign started in February and ended in March 2017 according to the following dates across the related GMOS sites:

- ITALY (MCU) started on 1st February and ended on 15th March (boreal winter);

- ARGENTINA (BAR) started on 1st February and ended on 15th March (austral summer);

- SOUTH AFRICA (CPO) started on 1st February and ended on 15th March (austral summer);
- RUSSIA (LIS) started on 6th February and ended on 20th March (boreal winter);
- CHINA (MAL) started on 10th February and ended on 24th March (boreal winter);

The second sampling campaign started at the end of May until mid of July 2017 according the following dates:

- ITALY (MCU) started on 31st May and ended on 7th July (boreal spring/summer);
- ARGENTINA (BAR) started on 31st May and ended on 12th July (austral autumn/winter);
- SOUTH AFRICA (CPO) started on 1st June and ended on 13th July (autumn/winter);

As example, in the following Fig. 6.1 the sampling scheme with information related to the codes of PASs and the time of exposure (i.e., two weeks, three weeks etc.) is reported.

6.2.3 Hg Data collection by Conventional methods and new PASs

On-going GMOS ground-based mercury measurements

Most of the on-going GMOS stations measure concentrations of atmospheric mercury fractions by using an automated and continuous mercury speciation system: the Tekran Mercury Vapour Analyzer Model 2537 coupled with the speciation models 1130 for GOM, and 1135 for PBM (Tekran Instruments Corp., Toronto, Ontario Canada). This equipment meets the GMOS requirements and is commonly available.

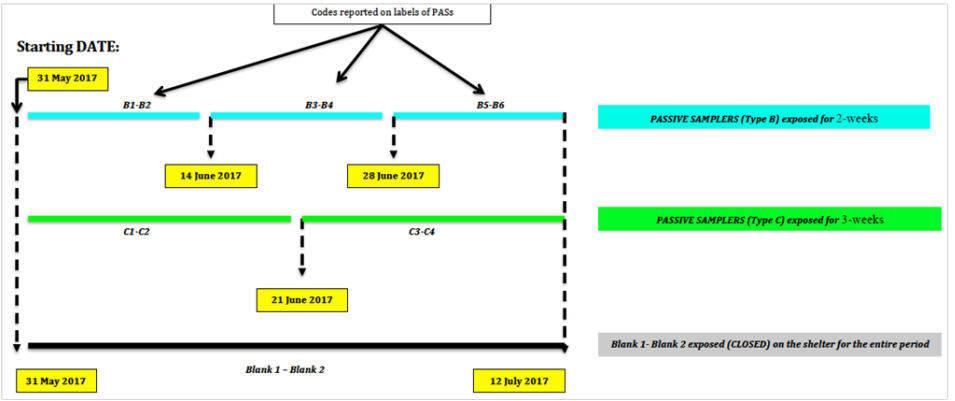

Figure 6.1: Sampling scheme with information related to the codes of PASs and the time of exposure (i.e., two weeks, three weeks etc.).

TGM measurements in air can also be performed by using a monitoring system from Lumex, which does not employ trap-and-desorb technology, but it is based on the Zeeman atomic absorption of mercury (Lumex, St. Petersburg, Russia). Among the on-going GMOS stations there are actually two ones that are measuring TGM levels by using the Lumex Analyzer. Data coming from the on-going ground-based sites have been acquired by the GMOS Cyber-(e)-Infrastructure (GMOS-CI) (Cinnirella et al., 2014; D'Amore et al., 2015). The GMOS-CI collects raw data on mercury observations and ancillary parameters from the GMOS network. Each monitoring site measures mercury and associated parameters following the Standard Operating Procedures (SOPs) established by the GMOS Consortium (Munthe et al., 2011) within the global network. The GMOS-CI was designed to integrate data from different data sources using different network protocols and data formats. In order to comply with this vision, different strategies were needed to match the requirements of each GMOS site, which are served by the so called Information and Communications Technology (ICT) infrastructures with different architectures and capabilities. In some cases, monitoring sites are reached by an Internet connection, while others are not. GMOS-CI offers two options in order to integrate

data:

- Data Upload through the GMOS GeoPortal, for those stations without Internet connection, by using a Human to Machine (H2M) approach; or
- Data Integration, using the System Integration capabilities of GMOS-CI, for those stations connected to Internet, by using a Machine to Machine (M2M) approach.

After their collection and integration data are screened with an ad-hoc validation process the "GMOS-Data Quality Management System - G-DQM" aimed to Quality Assure and Quality Control all datasets coming from the on-going GMOS sites. Once validation process has been completely done, all resulting data files, reporting only valid data, are then arranged, harmonized and stored within the GMOS central database.

Sampling Methods

As soon as the quartz filters are impregnated and the passive membranes are immediately thermally cleaned and then checked. After being assembled the passive samplers start to measure ambient Hg levels. A filter kept in the laboratory will measure laboratory levels, while field blanks measure the integrated exposure during the transport and storage periods. Before the passive samplers are sent to the field, they are labeled by an alphanumeric code inscribed onto each passive sampler identifying the lab, field blanks and field passive sample. An example the labelling code could be S2-C2-0316. Specifically, S2 is a tag related to the sampling site; C is a tag related to the exposure time (i.e., 1 week, 2 weeks, 3 weeks etc); the number following the label C (i.e. C2) is a serial number related to the sequential sampling within the scheduled sampling procedure. The final 4 numbers (here reported as 0316) are related to the passive batch fabrication number. The samples named as "Blank" (1 and 2, respectively) will be kept exposed throughout the sampling campaign, but tightly closed.

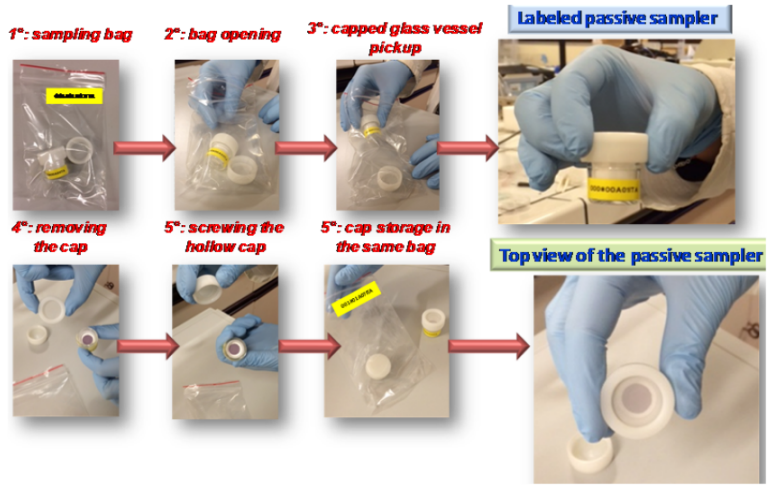

Figure 6.2: The assembling sequence of the passive samplers for their employment in the field.

Fig. 6.2 shows the assembling sequence of the passive samplers for the preparation of the shipping (1°-2°-3° phases), and the procedure for the exposition (4°-5°-6° phases).

For the placement in the field, the passive samplers were kept in a shelter under a rain shield. Each shelter, in fact, comprises 8 labelled positions to house up to 8 Passive Samplers (A-A, B-B, C-C, and Blank 1 and 2) (Fig. 6.3).
After the sampling, the passive samplers are placed in three plastic zip bags and stored in a dark and cool container. The samplers are sent to the CNR-IIA laboratory where the analysis are performed.
The average concentration at the measurement site over the time period in which the sampler is exposed to ambient conditions is determined by chemical analysis of the passive membrane. Passive samplers were analyzed directly by thermal desorption at $550°C$ by CVAFS (Cold Vapor Atomic Fluorescence Spectrometry). The analytical technique is based on 5 min thermal desorption at $500°C$ of the passive membrane under argon or nitrogen of purity greater than 99,999%, suitable for use as a carrier gas for CVAAS and CVAFS. Moreover,

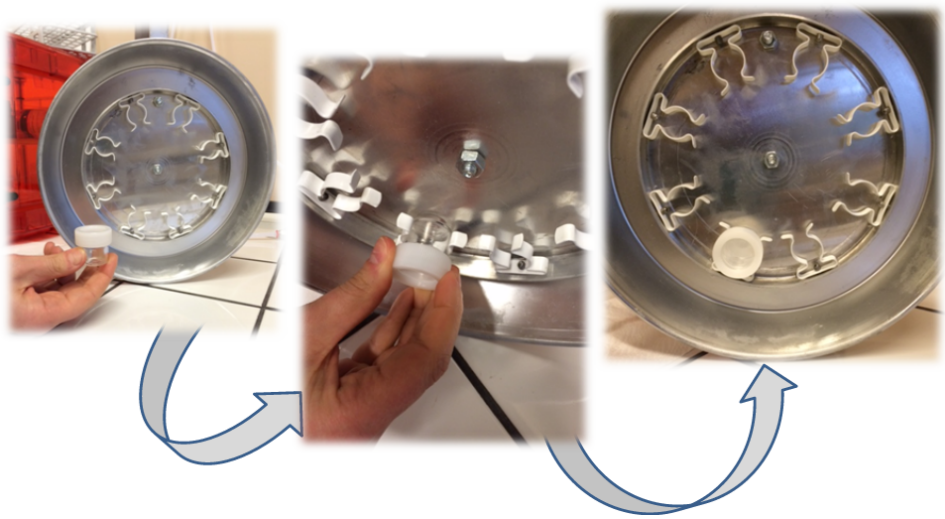

Figure 6.3: Shelter design and shelter seats for the passive samplers in the field.

the collection quartz coated surface (passive membrane) is the key factor of the passive sampling system which can be thermally regenerated and reused for further measurements after the desorbing phase.
Hg in atmosphere was measured from the beginning of the intercomparison exercise using both the methods, conventional measurements by Tekran/Lumex systems and Hg passive samplers. Within the selected sites only one (LIS) used a Lumex instrument. As it has been demonstrated in earlier intercomparisons, the Tekran and Lumex methods yield comparable results (Brown et al., 2010; Sprovieri et al., 2016). The Lumex instrument was run at a 5 min sampling frequency as well as the Tekran analyzers at BAR and MCU, whereas the Tekran at CPO was run at 15 min sampling frequency according to the GMOS-SOPs for remote and rural monitoring sites. The manual PASs method was run for 2 weeks and 3 weeks sampling times. The obtained Hg levels recorded by Tekran/Lumex were therefore averaged over the corresponding bi-weekly/three-weekly PASs exposing period to make comparable measurements resulting from the two different sampling

methods.

6.3 Results and Discussion

6.3.1 Hg levels recorded by reference instruments

A statistical summary of Hg concentrations obtained by conventional instruments (Tekran and Lumex) at the selected GMOS monitoring sites during the first and second campaigns is reported in Tab. 6.2. The GMOS sites located in the Southern Hemisphere, CPO and BAR, recorded, respectively, mean concentrations of 0.92±0.07 ngm^{-3} and 0.87±0.17 ngm^{-3}, during the first campaign and of 0.97±0.08 ngm^{-3} and 0.66±0.13 ngm^{-3}, during the second campaign (see Tab. 6.2). These values are in accordance with the annual mean concentration values normally observed in the Southern Hemisphere, which are generally lower than those observed in the Northern Hemisphere (Sprovieri et al., 2016). The other two sites, MCU and LIS, in fact, recorded mean values of 1.16±0.16 ngm^{-3} and 1.39±0.25 ngm^{-3}, respectively, during the first campaign, and 1.15± 0.12 ngm^{-3} at MCU during the second campaign (see Tab 6.2). These values are in good agreement with the overall mean concentrations observed at the multiple sites of the network distributed in the Northern Hemisphere. The last site, MAL, showed several technical problems of the Tekran analyzer, hence the QA/QC system recorded as "invalid" most of the data, resulting in a final dataset covering just the first two weeks of our interest. However, the mean concentration for MAL was of 1.40±0.31 ngm^{-3} during the first campaign well fitting with the Hg background value in the Northern Hemisphere.
The LIS station was also not involved during the second campaign due to technical maintenance of the Lumex instrument. As a result, the co-exposure of active and passive sampling devices during the second campaign was performed only at three sites, one in the Northern Hemisphere, MCU, and two in the Southern Hemisphere, BAR and CPO (see Tab. 6.2).

Table 6.2: Hg statistical summary at GMOS monitoring sites during the first and second campaigns.

Campaign	Information	BAR	MCU	CPO	LIS	MAL
1st	Instrument	Tekran	Tekran	Tekran	Lumex	Tekran
	Sampling Time	5'	5'	15'	5'	5'
	n	9808	10431	5385	16137	1498
	Min (ngm^{-3})	0.30	0.70	0.57	0.59	0.64
	Mean ± SD (ngm^{-3})	0.83±0.17	1.19±0.16	0.90±0.08	1.35±0.25	1.40±0.31
	Max (ngm^{-3})	1.28	2.30	1.25	2.60	3.46
2nd	Instrument	Tekran	Tekran	Tekran	-	-
	Sampling Time	5'	5'	15'	-	-
	n	7348	7949	3821	-	-
	Min (ngm^{-3})	0.20	0.70	0.65	-	-
	Mean ± SD (ngm^{-3})	0.66 ± 0.13	1.15 ± 0.12	0.97 ± 0.08	-	-
	Max (ngm^{-3})	1.47	1.45	1.60	-	-

As Table 6.2 shows, while from winter to spring/summer MCU did not show significant variations of Hg concentrations, BAR and CPO stations recorded higher Hg concentration during summer and lower during the cold season.

6.3.2 Comparison of Hg data between the conventional analyzers and the prototype devices (PASs)

Preliminary statistical analysis of quality data

In order to test the comparability of the methods a detailed data analysis have been performed considering Hg distributions and values observed at the selected sites by automated (Tekran/Lumex) and manual PASs instruments, respectively. In particular, the correct operation of the Hg passive devices was tested by exposing simultaneously two passive samplers for each selected measuring periods (varying from two or three weeks) and by comparing their results with those obtained, over the same observing period, from Hg standard reference instruments. According to the proposed development method, the mean value of the concentrations revealed by each passive device should be considered as the representative measure for their simultaneous exposure. The idea of this method is to guarantee stronger results considering possible statistical fluctuations of values. However, a preliminary analysis was

herein carried out to evaluate the measurement precision of each single passive device, and the potential occurrence of specific working anomalies as well as the influence of erroneous procedures of handling and storage. The Hg data distribution observed during each sampling campaign and at each selected monitoring station by the reference active instrumentation has been plotted by boxplots, where the central line of the boxplot shows the median value, the whiskers extend to the most extreme data points which are no more than range times the interquartile range from the box, and finally, the points besides the whiskers are outliers. Each obtained boxplot was then overlapped with both the single values of the corresponding Hg levels measured by the two co-exposed passive samplers, to establish how much the latest ones fit within the Hg Tekran/Lumex distribution. Hereafter, for each involved monitoring stations, specific graphs are reported and discussed for both the 1st and the 2nd campaigns and with respect to the planned measuring periods: 3 bi-weekly periods (1W2W, 2W4W, 5W6W) and 2 three-weekly periods (1W2W3W, 4W5W6W).

At MCU station, the statistical distribution of Hg levels recorded by Tekran was quite steady for both the 1st and the 2nd campaigns, with whisker values ranging in any case from 0.8 to 1.5 ngm^{-3} (Fig. 6.4). Otherwise, the Hg concentrations measured by each single co-exposed device (Passive 1 in red and Passive 2 in blue) showed in general a more variable response, either for each single exposition, either over time. Going in details, as Fig. 6.4a shows, it is possible to observe that during the 1st campaign the difference of each single measurement from the two co-exposed devices was larger over all the 3 bi-weekly periods (1W2W, 2W4W, 5W6W) with a divergence between values (Passive1 - Passive 2) around 0.7 ngm^{-3}. Anyway, over both the 2 three-weekly periods (1W2W3W, 4W5W6W), the precision was better, with a difference in values of only 0.1 ngm^{-3}. Further, in terms of accuracy it is possible to notice that the response of the passive devices was better over the 2 longer sampling periods (1W2W3W, 4W5W6W), with Hg concentrations levels resulting included within the whiskers of the Tekran Hg data distribution. During the 2nd campaign better results were obtained, in terms of both precision and accuracy (Fig. 6.4b).

Also in this 2nd campaign the divergence of measurements from the two co-exposed devices was larger over the bi-weekly periods in respect to the three-weekly ones but, in this case, with a narrow difference in values (around 0.3 ngm^{-3}). Over both the three-weekly periods the difference in values was almost null and thus showing a very good result. In terms of accuracy it is possible to notice that during the 2nd campaign, with the 5W6W as the only exception, the values recorded with the passive systems were close to the lower whisker value of the Tekran data distribution, thus resulting in a general underestimation by PASs in respect to the reference Hg values. Differently, during the 1st campaign there was a general overestimation. This difference in the device response over the two observing campaigns could suggest a potential influence of some meteorological factors. For this reason and for the MCU station as a case study, an in depth analysis was done, where the main meteorological parameters have been also taken in consideration in evaluating their possible influence on the PASs correct operation (see paragraph 6.3.2).

At BAR station, in general, the results were quite similar to those ones obtained and already discussed for the MCU station. In fact, the response of the passive devices was more precise and accurate with a general underestimation in values during the 2nd campaign in respect to those observed over the 1st one (Fig. 6.5). Specifically, only over two bi-weekly periods (1W2W and 5W6W) during the 1st campaign, the divergence from the simultaneous passive systems was about 0.3 and 0.6 ngm^{-3}, respectively. These same sampling devices gave also Hg levels far from the distribution of reference Hg Tekran data (Fig. 6.5a). However, with the above mentioned cases as an exception, it is possible to notice good results in terms of precision and accurancy. In fact, the difference of measured values from the co-exposed passive devises was in all other cases null or around 0.1 ngm^{-3}. Furthermore, the Hg concentrations measured by PASs were included or very close to the reference Hg distribution.

At CPO station, the sampling campaigns were negatively influenced by several problems. In fact, the samples of the 1st campaign were affected by extreme meteorological conditions, like very strong

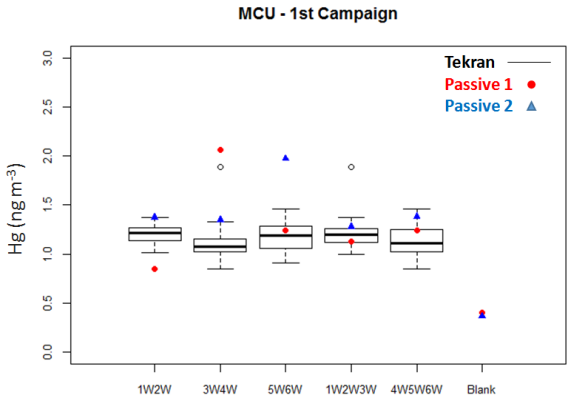

(a)

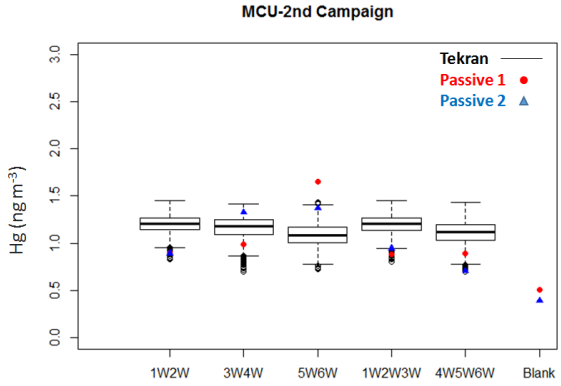

(b)

Figure 6.4: Comparison between the Hg Tekran data distribution, represented by boxplots, and the Hg data concentrations from each single co-exposed passive sample, data points in blue/red, obtained during the 1st (a) and 2nd (b) sampling campaign at Mt. Curcio station.

winds, which brought dust inside the passive vials. On the other hand, during the 2nd campaign, errors of storage had been done since just one plastic bag had been used, instead of three. These errors probably implied some bias on the results of passives that had measured much

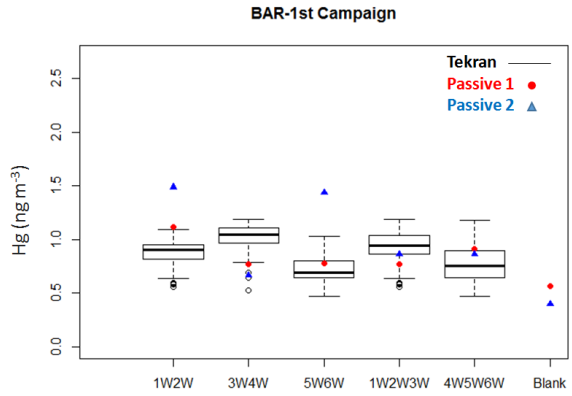

(a)

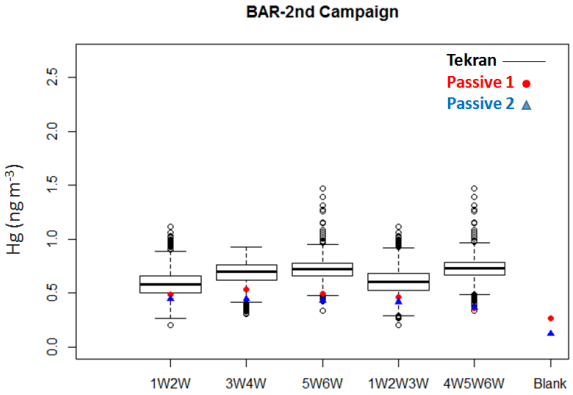

(b)

Figure 6.5: Comparison between the Hg Tekran data distribution, represented by boxplots, and the Hg data concentrations from each single co-exposed passive sample, data points in blue/red, during the 1st (a) and 2nd (b) campaign at the Bariloche station.

higher Hg concentrations than Hg data recorded by Tekran, for both campaigns (Fig. 6.6).

Also in terms of precision, not stable results were obtained with a difference of values (Passive 1 - Passive 2) ranging from 0.1 to 0.6

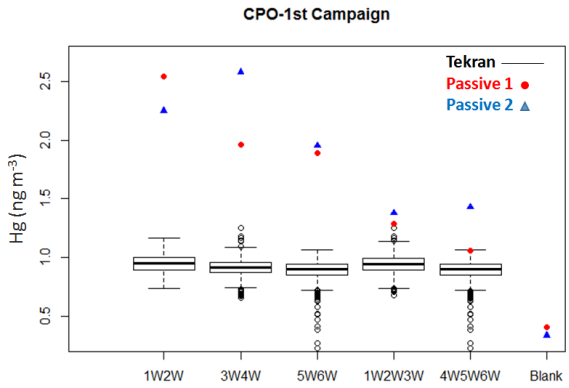

(a)

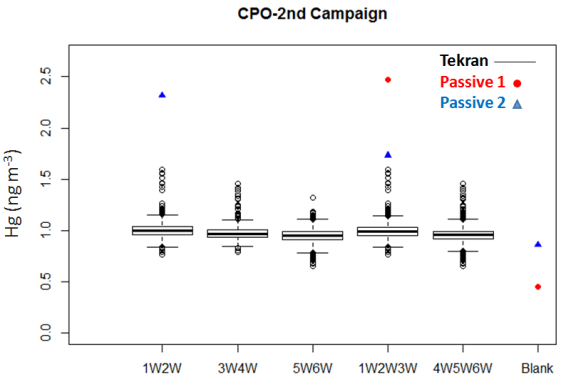

(b)

Figure 6.6: Comparison between the Hg Tekran data distribution, represented by boxplots, and the Hg data concentrations from each single co-exposed passive sample, data points in blue/red, during the 1st (a) and 2nd (b) Campaign at Cape Point station.

ngm^{-3}, in the 1st campaign (Fig. 6.6a) and from 0.1 to 2.0 ngm^{-3}, during the 2nd one (Fig. 6.6b). As an exception, during the 1st campaign and only for the three-weekly sampling periods (1W2W3W and 4W5W6W) the passive devices registered Hg values closer to the distribution of the reference Hg data. At LIS station, it was possible to

carry out only the 1st campaign, which gave back quite good results in terms of reproducibility. There was a general underestimation of passive results in respect to the Hg Lumex data distribution even if, over each observing period, both Hg concentrations measured by the two co-exposed passive devices resulted included within the lower part of the box-plot with reference Hg data. In terms of precision, the results were good only for the 3W4W observing period, whereas in the other cases a difference of values ranging from 0.2 to 0.4 ngm^{-3}, was recorded (Fig. 6.7).

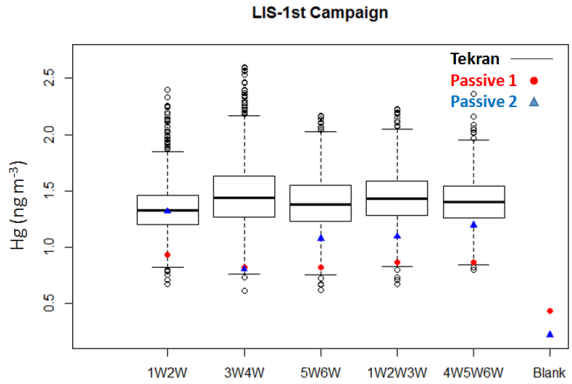

Figure 6.7: Comparison between the Hg Tekran data distribution, represented by boxplots, and the Hg data concentrations from each single co-exposed passive sample, data points in blue/red, during the 1st Campaign at Listvyanka.

At MAL station, there were technical problems of the Tekran instrument, resulting in a data coverage of just two weeks representative only for the 1W2W sampling period. However, for this specific case, the result of the Hg levels measured with passives were in very good accordance with the Hg reference Tekran data, being similar the response of the two simultaneous passive devices and their revealed concentrations very close to the median value recorded, over the same sampling period, by the standard Tekran instrument. For the other cases, for which reference values were not available, it is possible to notice that

the precision was quite variable with a difference in values that ranged from 0.1 to 1.0 ngm^{-3} (Fig. 6.8).

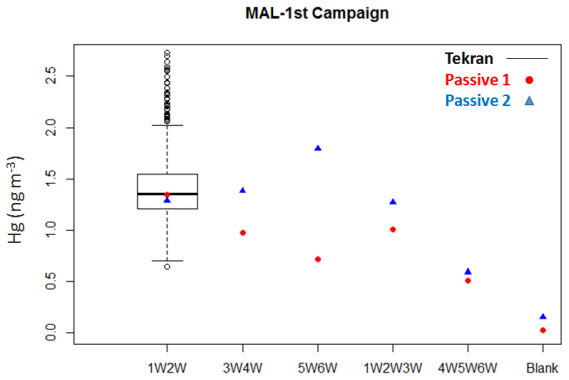

Figure 6.8: Comparison between the Hg Tekran data distribution, represented by boxplots, and the Hg data concentrations from each single co-exposed passive sample, data points in blue/red, during the 1st Campaign at Mt. Ailao.

Bootstrapping analysis

Due to the small dataset, the bootstrapping analysis was conducted to evaluate if the distribution of the mean Hg concentrations of Tekran, and of the Hg Passive (given by the mean value of the two simultaneous passives) belonged to the same population. The bootstrapping analysis is a random sampling with replacement, based on the inference about a population from sampled data. The population is modelled by a "resampling" of data, then the inference of "resampled" data is conducted. The bootstrapping analysis has been applied to the dataset of Mt. Curcio and Bariloche, because they showed the more solid and valid dataset, with the largest number of data (10 passives data/Tekran means), and without errors of sampling. The "null hypothesis", which there is no relationship between the populations of Hg mean values of Passives and Tekran data, has been rejected. In fact, like the distribution of the two populations showed, they were not independent (Fig.

6.9). Furthermore, the analysis highlighted that the distribution of Hg passives data was generally with a broader range than the Tekran distribution.

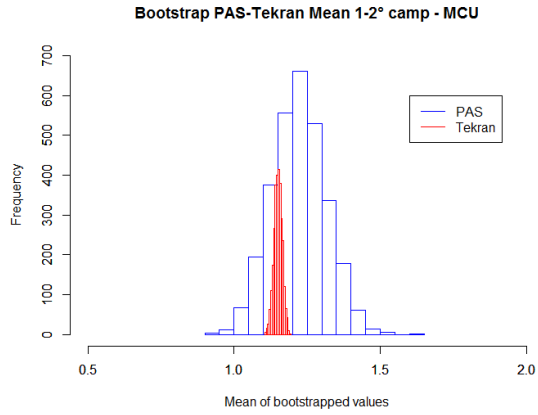

(a)

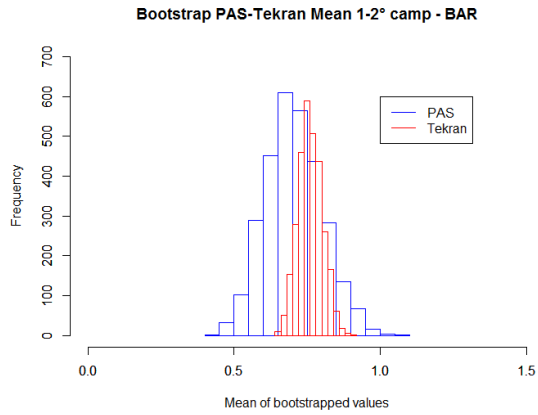

(b)

Figure 6.9: Comparison between Histograms with means of bootstrapped Hg values from Passives (PAS) and Tekran data observed during the campaigns at Mt. Curcio (MCU) (a) and at Bariloche (BAR) (b).

Synthetic statistical analysis

To obtain a synthetic characterization on the operation of the passive devices, for each observed sampling period, a comparison between the mean value of Tekran or Lumex Hg levels and the mean value of the two simultaneous passive samplers had been carried out. The comparison analysis for the MCU station showed good results especially for the 1st campaign, where PAS values (mean ± sd) were always in agreement with Tekran data. On the other hand, the 2nd campaign showed mainly PAS values lower than Tekran mean (1W2W, 1W2W3W, 4W5W6W) (Fig. 6.10).

The 1st Campaign performed at BAR station recorded good results especially for the three-weeks samples, whereas, in the comparison of the 2nd Campaign, the Passives resulted to underestimate the Tekran values (Fig. 6.11).

As already mentioned, the Cape Point campaigns showed several problems, like as, the dust into vials of passives or errors of storage, which caused invalid results, mainly with values very high (until 5 times the right value) (Fig. 6.12). The results of comparison campaign at LIS was acceptable, with PASs values in agreement with the mean values of Tekran, with the only exception of the 3W4W sample (Fig. 6.13).

For MAL station, it is important to point out that the comparison between Tekran and PAS data have been performed only on the first two weeks, as reported above, due to the overlap of some technical problems with the Tekran system. Fig. 6.14 reports the comparison between Hg Tekran mean values and PASs results for the first two weeks, showing a good agreement over the only single available data. This is also the reason for that MAL has not been involved during the second sampling campaign.

In Table 6.3, a synthetic statistical comparison between the results obtained during the 1st campaign by passive samplers and conventional analyzers was carried out to evaluate the difference (in %) calculated between the two systems over the sampling time considered. In particular, mean values over bi-weeks and three-weeks for

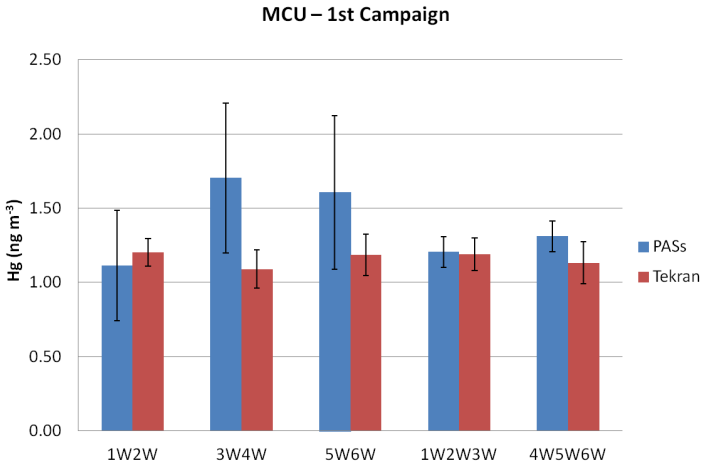

(a)

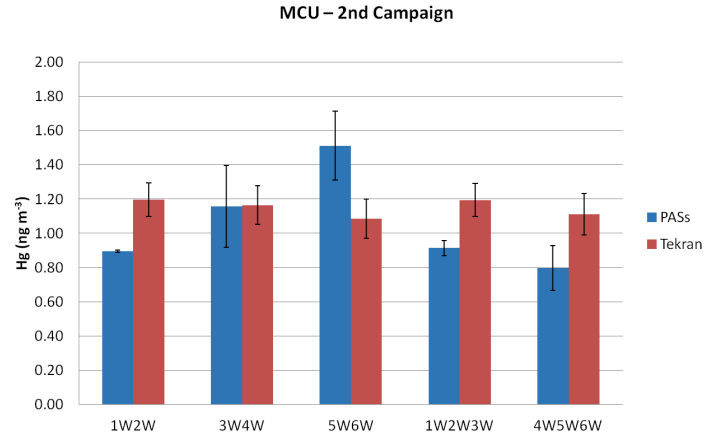

(b)

Figure 6.10: Comparison between Hg Tekran mean values and PASs results for the 1st (a) and 2nd (b) campaign at Mt. Curcio.

both Tekran/Lumex and PASs are reported in Table 6.3, as well as the difference between the systems. It was clearly observed that the

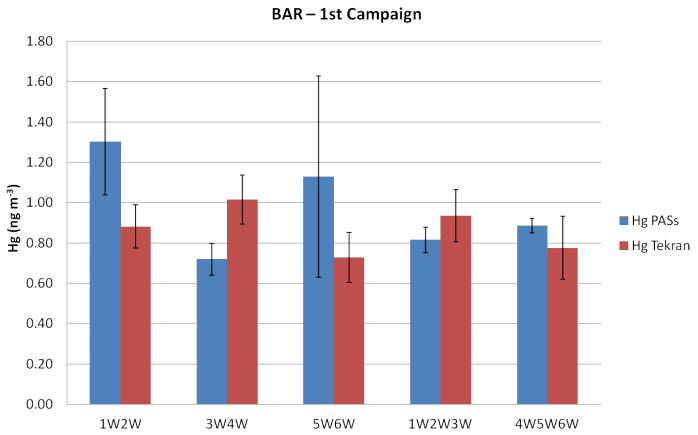

(a)

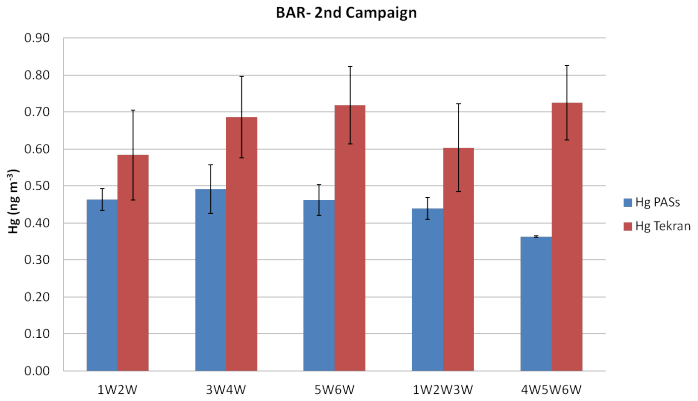

(b)

Figure 6.11: Comparison between Hg Tekran mean values and PASs results for the 1st (a) and 2nd (b) campaign at Bariloche.

overall variability in terms of percentage (%) between the methods decreases during the first sampling campaign, highlighting that the correlation between the PASs and the Tekran/Lumex instruments improved

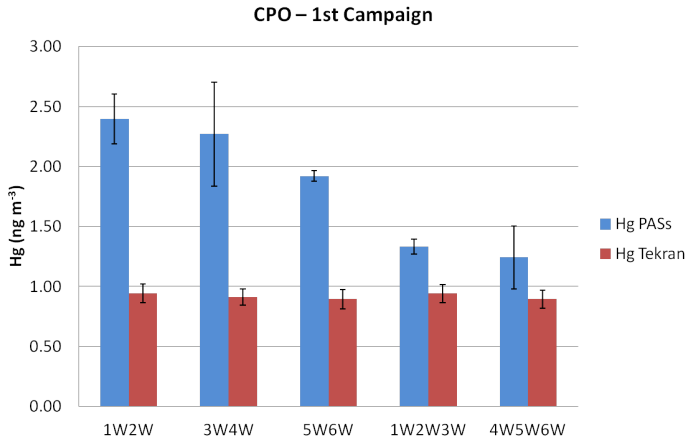

(a)

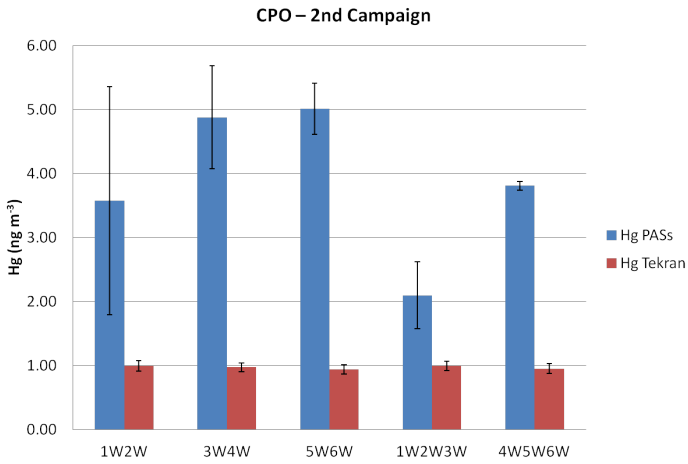

(b)

Figure 6.12: Comparison between Hg Tekran mean values and PASs results for the 1st (a) and 2nd (b) campaign at Bariloche.

continuously during the measurement period reaching acceptable difference values over three weeks. This results could be a clear consequence of the two simultaneous passives divergence over two weeks

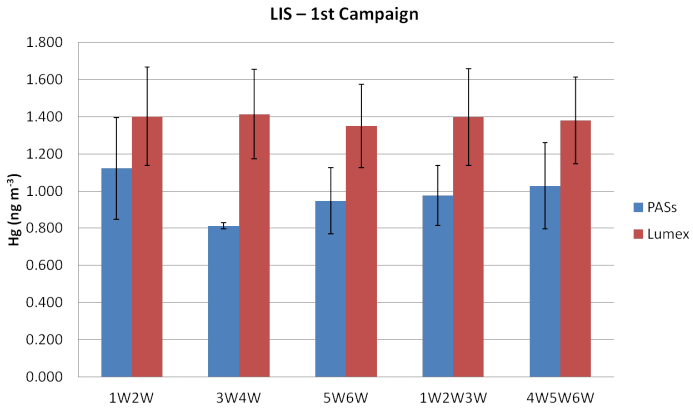

Figure 6.13: Comparison between Hg Lumex mean values and PASs results for the 1st campaign in Listvyanka.

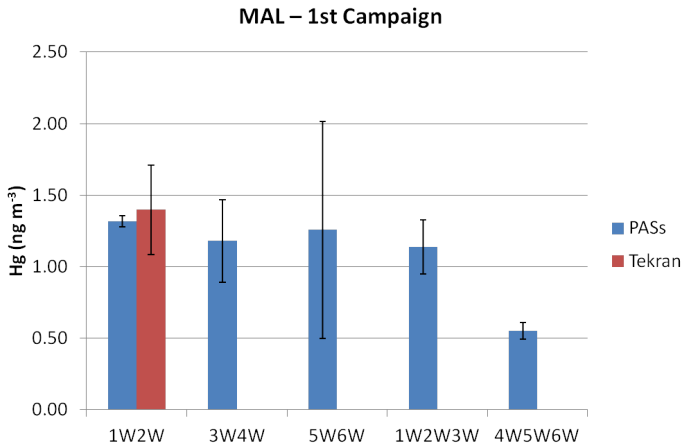

Figure 6.14: Comparison between Hg Tekran mean values and PASs results for the first two weeks at MAL and PASs results observed for the whole sampling period related to the 1st sampling campaign.

observed throughout the preliminary analysis performed by the box-plots of Hg data by PASs and Tekran/Lumex values, reported in the previous paragraph. In summary, with the only exception of the CPO

station, the difference (in %) between both systems for the first campaign ranged, in absolute value, from 10% to 29%.

Table 6.3: Synthetic statistical comparison between the results obtained during the first campaign by passive samplers and conventional analyzers carried out to evaluate the difference (in %) calculated between the two systems.

Site	Mean	Hg Tek/Lum (ngm^{-3})	Hg PASs (ngm^{-3})	Difference (%) systems
MCU	Bi-weeks	1.16 ± 0.14	1.47 ± 0.46	-27%
	Three-weeks	1.16 ± 0.15	1.26 ± 0.10	-8%
	Bi-Three-weeks	1.16 ± 0.14	1.37 ± 0.28	-18%
BAR	Bi-weeks	0.87 ± 0.13	1.05 ± 0.28	-20%
	Three-weeks	0.85 ± 0.15	0.85 ± 0.05	0%
	Bi-Three-weeks	0.86 ± 0.14	0.95 ± 0.17	-10%
CPO	Bi-weeks	0.92 ± 0.07	2.20 ± 0.23	-139%
	Three-weeks	0.92 ± 0.07	1.29 ± 0.16	-40%
	Bi-Three-weeks	0.92 ± 0.07	1.74 ± 0.20	-90%
LIS	Bi-weeks	1.39 ± 0.24	0.96 ± 0.16	31%
	Three-weeks	1.39 ± 0.25	1.00 ± 0.20	28%
	Bi-Three-weeks	1.39 ± 0.24	0.98 ± 0.18	29%

Table 6.4 reports the same above mentioned information related to the second sampling campaign. It is important to point out that the improvement of the difference between the methods did not occur in this sampling campaign. In fact, the difference (in %) between systems was larger and ranged from 11% to 34%.

Table 6.4: Synthetic statistical comparison between the results obtained during the second campaign by passive samplers and conventional analyzers carried out to evaluate the difference (in %) calculated between the two systems.

Site	Mean	Hg Tek/Lum (ngm^{-3})	Hg PASs (ngm^{-3})	Difference (%) systems
MCU	Bi-weeks	1.15 ± 0.11	1.19 ± 0.15	-3%
	Three-weeks	1.15 ± 0.11	0.86 ± 0.09	26%
	Bi-Three-weeks	1.15 ± 0.11	1.02 ± 0.12	11%
BAR	Bi-weeks	0.66 ± 0.11	0.47 ± 0.05	29%
	Three-weeks	0.66 ± 0.11	0.40 ± 0.02	40%
	Bi-Three-weeks	0.66 ± 0.11	0.44 ± 0.03	34%
CPO	Bi-weeks	0.97 ± 0.07	4.49 1.00 ±	-361%
	Three-weeks	0.97 ± 0.08	2.95 ± 0.29	-203%
	Bi-Three-weeks	0.97 ± 0.07	3.72 ± 0.65	-282%

In addition, for each involved GMOS site and for the two planned sampling campaigns, a synthetic statistical summary with a comparison between the mean values for Hg levels recorded by Tekran/Lumex

and PASs in reported in Table 6.5. Hg mean concentrations obtained by both sampling systems at all GMOS sites during the two sampling periods are also showed in Fig. 6.15.

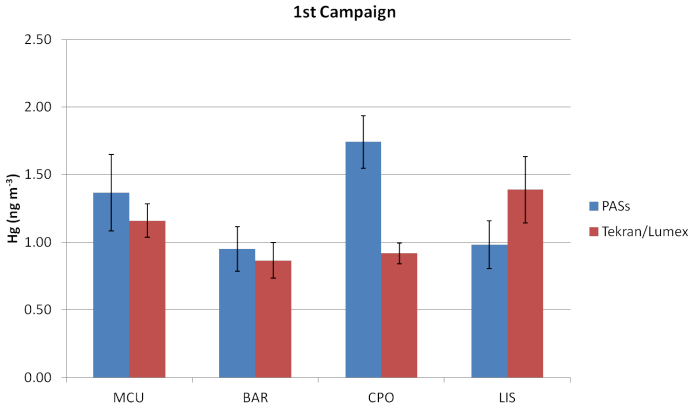

(a)

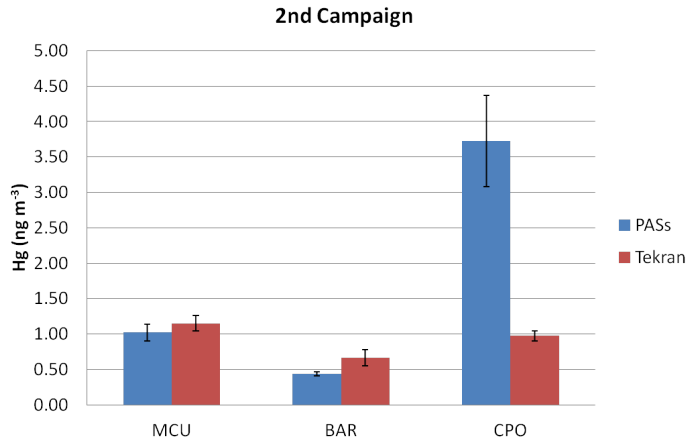

(b)

Figure 6.15: Comparison between Hg Tekran mean values and PASs results for the 1st (a) and 2nd (b) campaign at all GMOS sites.

The comparison between the mean concentrations obtained for both PASs and Tekran/Lumex analyzers produced acceptable results

for all the involved stations. The best results were recorded at the MCU station, where the PAS results were in good agreement with the Tekran concentrations for both the campaigns. At BAR, the PASs values resulted better for the first campaign, while the second campaign recorded values lower than Tekran concentrations.
As previously noticed, the CPO site was a negative exception with the PASs systems that recorded Hg concentrations not typically observed in South Africa and extraordinary higher than those measured by Tekran [(TK: 0.92 ± 0.07 and 0.97 ± 0.08) (PASs: 1.74 ± 0.20 and 3.72 ± 0.6)] (see Table 6.5). The higher and variable PASs results at CPO probably were due to uncorrected management and of the exposed samplers as well as incorrect storage and shipping of them in respect to those scheduled within the method (i.e., triple Ziplock bags). In addition, it is important to take into account that these results could be also influenced by the local conditions (i.e., dust, high wind speed, etc.) along with other parameters and factors occurred at the sampling site. Several samplers returned from the South Africa, in fact, showed the presence of dust inside the passive vials. From the Figure 6.15 it is possible to highlight that the PASs concentrations sometime resulted overestimated and underestimated compared to the Tekran values.

Table 6.5: Statistical summary of Tekran/Lumex and PASs data at GMOS sites during the first and second campaigns *(calculated only for the first two weeks).

Campaign	Method	Hg BAR (ngm^{-3})	Hg MCU (ngm^{-3})	Hg CPO (ngm^{-3})	Hg LIS (ngm^{-3})	Hg MAL (ngm^{-3})
1st	Tekran/Lumex	0.87 ± 0.17	1.16 ± 0.16	0.92 ± 0.07	1.39 ± 0.25	1.40±0.31*
	PASs	0.95 ± 0.17	1.37 ± 0.28	1.74 ± 0.20	0.98 ± 0.18	1.32 ± 0.04*
2nd	Tekran/Lumex	0.66 ± 0.13	1.15 ± 0.12	0.97 ± 0.08	-	-
	PASs	0.44 ± 0.03	1.02 ± 0.12	3.72 ± 0.64	-	-

Influence of Meteorological parameters on Hg PASs sampling results

Among the stations involved into the comparison campaigns between the passives systems and the conventional systems, we chose the CNR-IIA Station, located at Mt. Curcio (MCU), to analyze any influences of meteorological data, such as, the air temperature, the wind speed, and the relative humidity, on the passives' efficiency. The MCU is an high altitude station (1780 m a.s.l), hence, during the winter season, it is generally characterized by continuous snowfalls, low temperatures, and many storms, while, during the spring and in summer, the weather is mainly fair and the temperature increases until about $30°C$. The first comparison campaign was performed during the winter season, from the 1st of February 2017 until the 15th of March 2017. Unfortunately, during this period, the meteorological sensors presented some technical problems, resulting in a data coverage for only the last two weeks of the campaign. The temperature for this period was very low, ranging between about -5$°C$ and 10$°C$, with a mean value of 1.3±3.7$°C$, while the wind speed recorded was about 4.9 ms^{-1}, and ranged from calm wind condition to a maximum value of 24.3 ms^{-1}. Moreover, the mean relative humidity was about 67%. Due to the scarce dataset of ancillary parameters (only two points), any qualitatively discussion was not possible (Fig. 6.16). On the other hand, the second campaign, which started on the 31st of May 2017 until the 7th of July 2017, involved two seasons, the spring until the summer solstice, on the 21st of June, and the beginning of summer. During this campaign, the temperature ranged between about 5$°C$ and 30$°C$, and the mean values calculated over the sampling weeks was increasing gradually following the change of season (we remember that into the label is included the number of the week). The wind speed ranged between 0 ms^{-1} and 20 ms^{-1}, while the mean value was of 3.2±2.6 ms^{-1}. Finally, the mean value for the relative humidity of the whole period was about 50%.The spring/summer campaign showed an interesting behavior of the meteorological parameter and the passives' response. By a qualitative analysis, it seemed that the PASs concentrations were

raising with an increase of the temperature and of wind speed (Fig. 6.17a and 6.17b), except for the three-weeks sample 3W4W5W, which did not show this behavior with clarity. The RH ancillary parameter seemed to not cause any influence (Fig. 6.17c). However, this dataset is still too little to proceed with a quantitative analysis that could confirm any influence with certainty. Hence, further measurements, for longer period could allow to establish or exclude some dependence on the meteorological parameters.

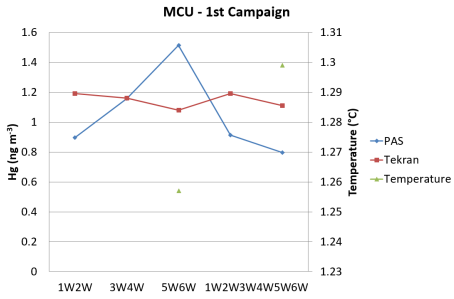

(a)

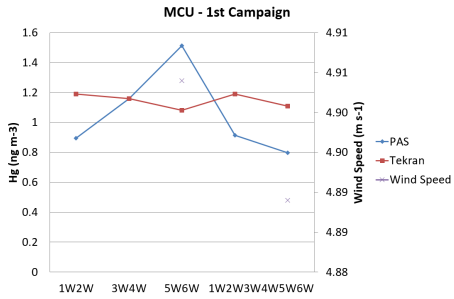

(b)

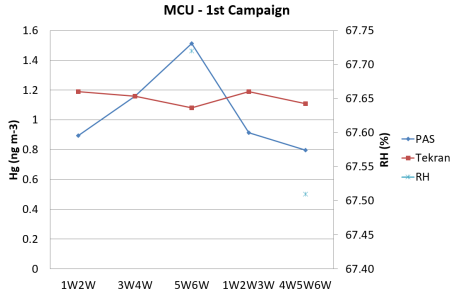

(c)

Figure 6.16: Comparison between Hg pattern from Passives (PAS) and Tekran data observed during the 1st campaign at Mt. Curcio (MCU) and the meteorological parameters: air temperature (a), wind speed (b), relative humidity RH (c).

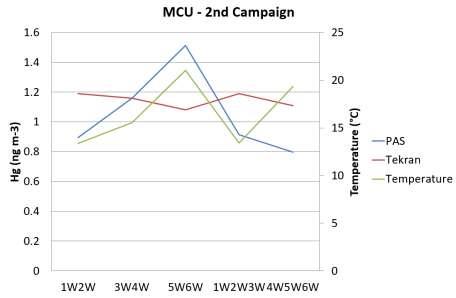

(a)

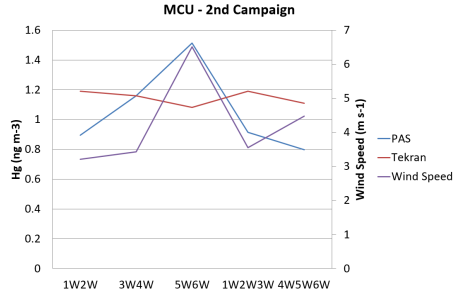

(b)

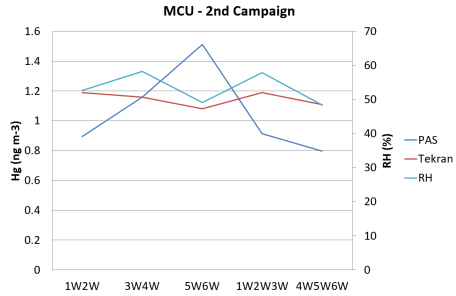

(c)

Figure 6.17: Comparison between Hg pattern from Passives (PAS) and Tekran data observed during the 2nd campaign at Mt. Curcio (MCU) and the meteorological parameters: air temperature (a), wind speed (b), relative humidity RH (c).

6.4 Conclusions

The passive devices developed by the CNR-IIA for the Hg monitoring in ambient air have been employed for the first time in the field during two sampling campaigns at five selected GMOS sites, three in the Northern Hemisphere (in Italy, Russia, and in China) and two in the Southern Hemisphere (in Argentina and in South Africa). This first experiment was performed in order to test their validity in different meteorological and geographical conditions characterizing each site.
Firstly, from the analysis of the first campaigns is clear that the method of sampling (i.e. the shelter) should be improved to avoid accidents of sampling in extreme meteorological conditions, like as strong winds with sandstorm or cloudbursts, which could bring, respectively, dust or water inside the vial of passives. Although the preliminary intercomparison results between PASs and the conventional active systems showed some variability and disparities in the data that could be due to some limitations of the samplers, in other conditions observed they seem to suggest promising results, in terms of both precision and accuracy.
Therefore, additional experimental campaigns could allow establishing if eventual over/underestimations are predictable and so preventable. For example, whether there is loss during the transport from the sampling location to the laboratory has not been quantified. In order to make comparisons using different methods, they need to be fully intercompared at a location with variable and measurable concentrations of the target compounds. This will need to be done with a suitable number of samples for reasonable statistical analyses. Further campaigns of comparison are thus essential to improve the robustness of the Passives System.
Hg passive samplers, despite limitations, have significant utility since they may be widely deployed and do not require electricity or specific site characteristics. They are also useful for establishing data platforms from which a better understanding of spatial and temporal trends in concentrations may be established. This information may also be used to determine where more detailed air monitoring would

be useful. It is clear that additional field performance tests are needed to characterize Hg passive samplers, and further development is needed before we can completely confirm the robustness of the method. For example, the CNR-IIA passive samplers need to be further tested at a monitoring site for a larger deployment period, employing in parallel a larger number of passive samplers for established time period in order to obtain a bigger amount of data for a detailed statistical analysis to assess the robustness of the method and of the sampling devices. The ease of deposition (electrospinning) and preparation (UV-irradiation in aqueous solution) as well as the high Hg sensitivity, suggests the chance to investigate the devices features by further comparison of the systems. Further investigations are in fact necessary also to assess the effects of physical parameters of the environment, such as temperature fluctuations and UV-light, as well as chemical ones, such as volatile organic compounds and gas (like halides and sulphides) which are potentially interfering the adsorption process of the Hg on gold. We are currently measuring uptake curves in PASs deployed at a number of sites with ongoing active sampling across a wide range of climatic conditions. Other measurements in the field are needed to verify if there is a dependence on the meteorological conditions, like as, temperature, relative humidity, and wind speed. The influence of meteorological factors should be isolated and examined individually. Further research is needed to address these uncertainties. Lastly, in order to be applied in broad regional and global networks a standardized method should be applied that has been calibrated and is accurate. In conclusion, further work into the testing of the developed Hg passives is essential to argue their validity in every condition, and after that, to strengthen the GMOS Network, thus providing an alternately sampling method that will be not expensive and user-friendly.

Chapter 7

New Sensor for Mercury Measurements in wet deposition

7.1 Sensors for Mercury in wet depositon

The wet deposition represents a crucial trouble because allows to Hg to enter into the acquatic system. When it is deposited, Hg could be in its elemental form (Hg^0) or in its reactive form (Hg^{2+}). Therefore, the elemental form could oxidize through photochemical processes. The Hg could react with Me (CH_3^-) to become MethilMercury (MeHg/CH_3Hg^+), which is bioaccumulated into the fishes. Big fishes, like as swordfish and tuna, are involved into the process of biomagnification, because they eat smaller Hg enriched fishes, increasing considerably their Hg concentration. Finally, Hg enriched fishes arrive into the food chain, where people can have damages to the nervous system or kidneys, until the death at high concentration.
Therefore, many attempts to quantify Hg^{2+} in wet deposition have been made. Several works attempt to use the Silver Nanoparticles (AgNPs) to realize a colorimetric sensor for Hg(II). In presence of Hg(II), the absorbance of AgNPs decreases showing a visible change of color,

from deep yellow to light yellow. The absorption spectra show a shift of the wavelength to the blue due to the oxidation of Ag(0) to Ag(I). The limit of detection (LOD) is of 0.06 ppm, although it can be reduced to 0.008 ppm in presence of Cu(II) (Jarujamrus et al. [2015]). A biological agent (soap-root plant) has been used as a stabilizing for Ag-NPs. The synthesis and stabilization of the sensor require 3 hr, while the LOD is only 0.44 ppm (Farhadi et al. [2012]). Another colorimetric sensor for Hg(II) that has been developed is based on citrate-capped AgNPs. It requires a long time of preparation (48 hr), and a high LOD (2 ppm) (Wang et al. [2012]). The silver nanoparticles have been used also as AgNPs-embedded poly(vinyl alcohol) (Ag-PVA) thin film. The sensor fabricated is selective for Hg^{2+}, Hg_2^{2+}, and Hg, while the limit of detection is 1 ppb (Ramesh and Radhakrishnan [2011]). A polypyrrole (PPy) film immobilized on the gold surface has been developed to detect Hg^{2+} in water. To increase the sensitivity until 0.001 ppm, 2-mercaptobenzothiazole (2-MBT) has been added. The monitoring is conducted through the Surface Plasmon Resonance (SPR) (Jorn et al. [2004]). Functionalized multi-walled carbon nanotubes (MWCNTs) with a LOD of 0.5 ppb were used to detect Hg^{2+}. The response time is very fast (5 s), moreover it could be reused at least 55 days (Khani et al. [2010]). Some DNA-based sensors for Hg^{2+} have been investigated (Chen et al. [2014], Kong et al. [2009], Liu et al. [2010], Niu et al. [2011]). One of this sensors has been realized by a covalent conjunction of the aminated poly-$T_{(25)}$ oligonucleotide onto the glass carbon electrode (Wang et al. [2012]). Therefore, Hg^{2+} establishes an interaction with a bis-thymidine through the N_3 of thymidine. It bridges two thymidine residues to form T-Hg-T base pairs with a binding constant equal to $4.14 \cdot 10^6 Lmol^{-1}$. In presence of Au(III), the chelated mercury, between the two thymidines, could accelerate the formation of gold amalgamation. The amalgamation is investigated by AFM and cycling voltammetry (Chen et al. [2014]). Like thymidine, also the thymine establishes a strong and stable bind with Hg^{2+} (Miyake et al. [2006]). Moreover, the thymine-Hg-thymine based sensor can be AuNPs functionalized increasing the detection limit until 3.2 nM (Kong et al. [2009]). The mercury ion specific bonding (MSB) probe

based on DNA strands could be used like sensor using the conformational switching of thymine in presence of Hg^{2+}, which folds itself into a "hairpin" structure. The MSB is released from the sensor, inducing a decrease of the current during the cyclic voltammograms (Liu et al. [2010], Wu et al. [2010]). Recent studies showed that Limonene is sensitive to Hg^{2+}. Indeed, when a polysulfide (Sulfur and D-Limonene) is exposed to a solution of $HgCl_2$, a bright yellow deposit will be formed. Furthermore, no change of color is observed with other chemical elements, like as, Li^{+}, Fe^{3+}, Ca^{2+}, Cu^{2+}, Pb^{2+}, Mg^{2+}, Zn^{2+}, Ni^{2+}, K^{+}, Mn^{2+}, and deionized water (Crockett et al. [2016]).
In this work, we tried to realize active sensors, characterized by a real-time response, based on the impedimetric variations. Two different sensors have been realized, both sensitive to Hg^{2+} in a solution. The first sensor has been functionalized through the Poly(thymine) trying a correspondence between the variation of the physical configuration (from straight to "hairpin") due to the concentration of Hg^{2+}, and the electrochemical impedance of the sensor itself. The other sensor that we would develop, is based on the use of the Limonene. We attend an impedance variation corresponding to the binding of the Hg^{2+} to Limonene.

7.2 Impedimetric analysis

In this section, the method to perfom the impedimetric measurements, and the needed materials are described.

Three Electrode Cell

The voltammetry deals with the study of the current in function of applied potential, obtaining information about analytes. In voltammetry, three electrodes cells are usually used, although at least two electrodes are enough. Hence, the two electrodes, the working electrode (WE) and the reference electrode (RE) are, respectively, the

electrode where happens the reaction, and the electrode which maintains the reference potential. The WE can be a cathode or an anode if the reaction is respectively a reduction or an oxidation. It is made of inert materials, likes as, gold, silver, platinum, glassy carbon or pyrolytic carbon, mercury drop and film electrode. The RE has a stable and well-known potential, thanks to a redox system with constant (buffered or saturated) concentrations of each participant of the redox reaction. To maintain stable the potential of RE, avoiding currents which could modify its potential, it is useful to add a further electrode, called auxiliary, obtaining a three electrode system. The current flows through the auxiliary electrode (AE), but doesn't happen the reaction of the WE. Usually, the AE has a higher area than working electrode. Moreover, it is isolated with fritz glass to ensure not influence and contamination on the reaction on the working electrode. Furthermore, auxiliary electrodes are made of inert material like as gold, platinum, and carbon.
In this work, commercial gold three electrodes - Micrux Technologies (Oviedo, Spain) were used (7.1). They present a substrate of glass, with a protective layer of SU8-resin, while the electrochemical cell is of 2 mm of diameter. The principal advantages are the low cost, the prospect of reuse, the reproducibility and the sensitivity.

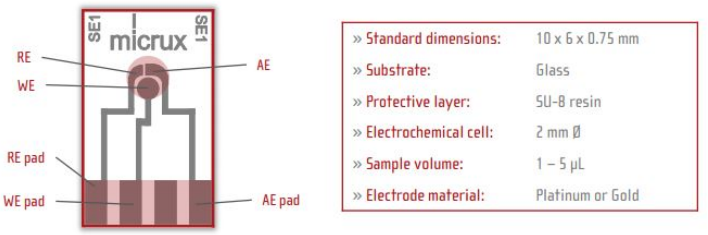

Figure 7.1: Three Electrode Cell- Micrux and features.

Voltammetry

Voltammetry, together potentiometry, that measures the potential between two electrodes, and amperometry, that measures the current between electrodes, is one of the electroanalytic methods. Voltammetry is a particular case of amperometry, in which the measure of the current is conducted while the potential is changing at a constant rate. The graph describing the behavior of the current in function of the potential is called voltammogram.
When an electrode is subject to a variation of potential or an adsorption process, on the electrode surface there will be a (dis-)charge of the electrode surface. During this processes, called capacitive, the capacitive current ("non-faradaic") is due to the electrical charges of the electrode, and of the electrolyte solution close to the electrode. This two layer of charges realize a double layer on its surface, which could be schematized like as a capacitor. The double layer can be explained by the Helmotz model which establishes that the charge on the electrode (Q) is directly proportional to the difference of potential (E) and to the capacitance of body (C) into the following way:

$$Q = CE \tag{7.1}$$

with the capacitance which follows the law:

$$\frac{C}{A} = \frac{EE_0}{l} \tag{7.2}$$

where E is the dielectric constant of the body dividing the two plans, E_0 is the permittivity of vacuum, l is the distance between the two plans, A is the area of the electrode. The current can be deduced by deriving 7.1 in respect of time, obtaining:

$$\frac{dQ}{dt} = C\frac{dE}{dt} \tag{7.3}$$

where at the first member it is possible to identify the current (I), while at the second member the rate of potential (ν), therefore, in mathematical terms:

$$I = C\nu. \tag{7.4}$$

In this way, we obtained a relationship between the capacitive current and the rate of potential.
On the other hand, when reactions happen on the electrode surface, we can speak of faradaic current and thanks to the current peak (corresponding to a specific potential) it is possible to deduce the species involved.
In cycling voltammetry, the potential on the WE is varied from an initial value (E_0) until a limit value (E_f), called inversion potential, to back to the initial value (E_0) inverting the potential. Therefore the potential describes a triangular function. In a solution without an electroactive species, the result of a cycling voltammetry is just the capacitive current, due to the double electric layer created by the ionic migration. Therefore, at the beginning, the current grows for the potential variation, but successively the current remains constant because the potential scansion rate is constant. When the potential is inverted, also the current inverts its sign. Finally, at the suspension of the potential, the current will be null (Fig. 7.2).

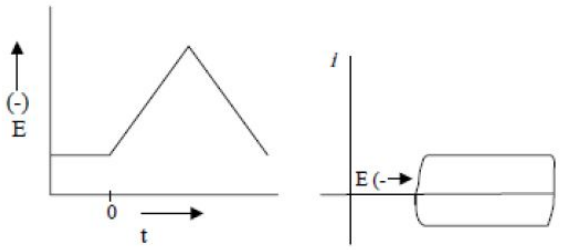

Figure 7.2: Cycling voltammetry without electroactive species.

The electrochemical reactions are mainly established by the Nernst Equation that shows the relationship between species concentrations and the potential of electrode:

$$E = E_0 + \frac{RT}{nF} ln \left(\frac{a_{ox}}{a_{red}} \right) \tag{7.5}$$

where E_0 is the standard potential of the couple RED/OX, nF the Faraday's constant (nF=96485,3365 C/mol), a_{ox} e a_{red} the species oxidized and reduced concentrations. At first, the concentration of oxidated/reduced species in the bulk is homogeneous. When a potential is applied, the oxidated/reduced species acquire/release electrons from/to electrodes, creating a gradient of the species in the bulk. According to the first law of Fick, a gradient of concentration of a species create a flux towards points with a minor concentration, therefore, the resulting flux is established by:

$$J = \frac{dN}{Adt} = -D\frac{\partial C}{\partial x} \tag{7.6}$$

where N is the number of moles, A is the surface, t the time, whereas, D is the diffusion constant, C is the concentration and x is the distance from the electrode. This transport of the species oxidated or reduced allows the reduction or oxidation on the electrode, creating a resulting current. Therefore, during a potential scansion, the current describes a peak, reaching a maximum value at the corresponding potential of oxidation (reduction), after this potential, the current decreases because analytes are decreasing. Inverting the scansion, the potential of reduction (oxidation) will be reached, showing an inverse peak of current (a depth) in respect of the previous. Given a charge Q involved in the reaction

$$Q = nFN \tag{7.7}$$

where nF is the Faraday's constant and N is the number of moles, the resulting current will be:

$$I = \frac{dQ}{dt} = nF\frac{dN}{dt} = nFAJ = -nFAD\frac{\partial C}{\partial x} = nFAD\frac{C_{bulk} - C_x}{\Delta x}. \tag{7.8}$$

Therefore, at a greater flux corresponds a greater current, moreover, when the current is cathodic (reduction) its values are negative, instead when the current is anodic (oxidation) its values are positive 7.3. In a cyclic voltammogram, the peak current, in just one electroactive species (OX/RED), is established by the Randles-Sevcik equation:

$$I_p = kn^{3/2}AD^{1/2}\nu^{1/2}C_{bulk} \tag{7.9}$$

where n is the number of moles of transfered electrons per moles of electroactive species transformed, A the area of electrode, D the diffusion constant, ν is the rate of scansion, C_{bulk} is the concentration of species in the bulk, and k is a constant equal to $2.69 \cdot 10^5$.

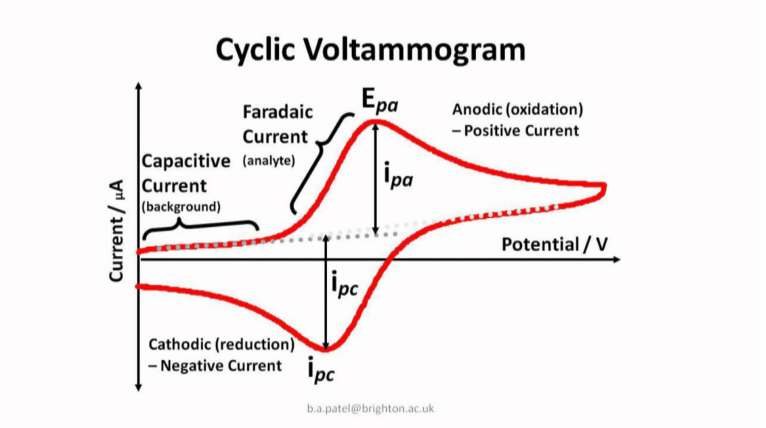

Figure 7.3: Cycling voltammetry without electroactive species.

Before of starting with the real treatment on the three electrodes, the cyclic voltammetry is applied to conduct the pre-cleaning of it. Indeed, through several cycles of voltammetry in a background electrolyte (BGE), like as H_2SO_4, HCl, KCl, the impurities of the three electrodes are released.

Self-Assembled Monolayer

The Self-Assembled Monolayer is an organized layer of amphiphilic molecules with the affinity between their heads and substrate. Molecules show hydrophilic and hydrophobic group. Therefore, when they are immersed in aqueous liquid, the two groups form a bilayer with hydrophobic tails toward external, instead hydrophilic heads toward internal. At first, molecules are in a chaotic phase, called lying down phase, and after some hours they start to form a crystalline or semicrystalline structures over the substrate. Successively, they absorb on

the substrate thanks to the van der Waals interactions and distribute themselves in a close-packed to realize a monolayer (Fig. 7.4). These adsorbates lower the free energy of the interface between the substrate and the environment. Many head groups have high affinity with specific metals, metal oxides, and semiconductors. The most diffuse SAMs are alkanethiols and silanes on a substrate like as gold, silver, copper, palladium, platinum and mercury. The principal advantage is the extremely facility to realize a monolayer, although it requires a long time (overnight). Therefore, the Self-Assembled Monolayer allows to study the interactions at the interfaces, molecules - substrate and molecules - solvent, and to investigate phenomena like as the growth, the ordering, the wetting, the adhesion, the lubrication, and the corrosion.

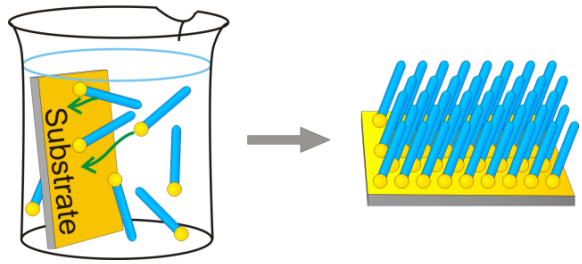

Figure 7.4: Self Assembled Monolayer's formation.

Chronoamperometry

The technique of chronoamperometry allows conducting an analysis of a nucleation process and to determine the quantity of charge for deposition or dissolution. This method implies the measurement of current versus time, setting the system at a constant potential or at a sequence of potential pulse. We suppose that an electrode is immersed in a solution with just oxidized form (Ox). When a specific potential is applied, oxidized forms in the proximity of the electrode surface are reduced (Red). In this way, there will be a concentration gradient of Ox, followed by the diffusion of Ox in the bulk of solution to the electrode surface, where they will be subject to reduction reactions.

During this process, the current decreases until the zero value. At reverse, applying a potential to reduced forms, they will be oxidized and can diffuse away from the electrode surface. The behavior of current in time (t) is established by the Cottrel Equation:

$$I = \frac{nFA\sqrt{D}C^b}{\sqrt{\pi t}}$$

where

- n: number of electron moles involved
- F: Faraday's Constant (96458C/mol)
- A: electrode surface
- D: diffusion coefficient of species
- C^b: analyte concentration in solution.

On the other hand, the capacity current, due to the double layer, follows the function 1/t, thus it decrease to zero in few ms (Fig. 7.5). Generally, the chronoamperometry is conducted at single potential step, from E_0 to E_s, but it is possible to conduct experiment also at double potential step, with a forward potential step. The Chronoamperometry can be used also to immobilize molecular structure on the electrode, like an alternative method to the Self Assembled Monolayer, because applying a constant potential on the gold working electrode (1.3 V vs Ag/AgCl) it is possible driving molecules in the proximity of the electrode.

Atomic Force Microscopy (AFM)

The Atomic Force Microscopy (AFM) or Scanning Force Microscopy (SFM) creates a sample image "feeling" or "touching" it. The AFM uses a mechanical probe set to a mobile cantilever subjects to movements due weak interaction (van der Waals Forces) between the probe and the sample. Generally the probe is made by silicium or silicium

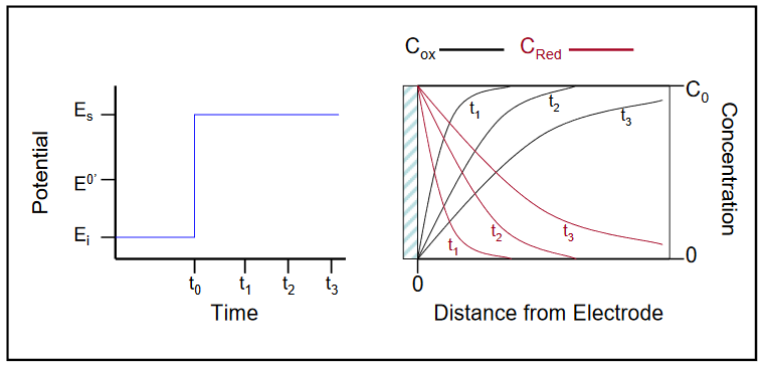

Figure 7.5: Potential Plot (on left) and Concentration of species versus distance from electrodes (on right) in chronoapmerometry.

nitride.The deflection (until 0.01 nm), established by the Hook's Law (elastic constant is known), is tracked by the reflection of a laser. The reflected light is revealed by a photomultiplier. The photomultiplier amplifies the signal of the cantilever movement, hence, for example, for a cantilever of length l and a photomultiplier of 2L, the gain is equal to 2L/l. Sometimes, due to the expansive cost and the large dimensions of laser, it is replaced by a piezoresistive probe, which reveals deflessions. Furthermore, to avoid damaging the probe, the force between the probe and the surface could be maintained constant, while the probe is moving. There are different mode of operation:

- Contact Mode: force between the probe and the sample surface is constant, and therefore also the deflection;
- Non-Contact Mode: the probe is forced to oscillating near the resonance frequency, therefore, the oscillation is modified by interaction forces, and thanks to them, it is possible to deduct sample information;
- Tapping Mode: generally, samples show a meniscus liquid that can block the probe on the surface. Alternatively, using a tapping mode that implies a cycling touch of the surface, it is possible to avoid to this problem.

An analysis of biosensors at the AFM allows exploring the surface verifying their properties of roughness, waviness, and texture. The roughness indicates the deviations of the normal vector from the ideal surface to the real surface. The waviness is defined like "the irregularities whose spacing is greater than the roughness sampling length". Finally, the texture indicates the variations from an ideal flat surface, hence, it includes the roughness, the waviness and the lay. Finally, the lay is the direction of the predominant surface pattern.

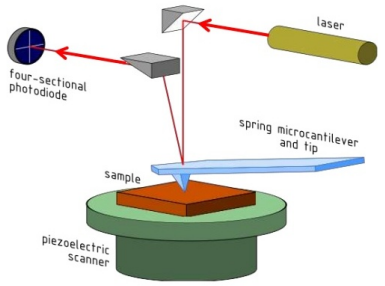

Figure 7.6: Principle of operation of Atomic Force Microscopy.

Electrochemical Impedance Spectroscopy

Impedance Spectroscopy is a powerful method to investigate the electric proprieties of materials and the interfaces. In particular, it is possible to study the dynamics of charge (bound or mobile) in the bulk or at the interface of the sample, which can be liquid or solid and made of materials like as ionic, semiconducting, mixed electronic-ionic and insulators (dielectrics). The principle of Impedance Spectroscopy is the approximation of the system to an electric circuit, considering all the involved proprieties, like as the polarization resistance (R_p), the resistance of charges in solution (R_s), the capacity of double layer created at the interface electrode-solution (C_d). Therefore, the charge transfer at the interface creates a mass transport of reactants and products, originating another form of impedance (Z_w), called Warburg impedance. The system, which generally is an electrode with over a material, is

subject to a known voltage or current, and successively, the electric response, current or potential, respectively, is analyzed. The behavior of the system is deducted in analogy with the electronic equivalent circuit (EEC). The first EEC proposed by Randles is shown in (Fig. 7.7), which is schematized with both components working mainly at high frequencies, like as R_s, and at low frequencies like as Z_w. The

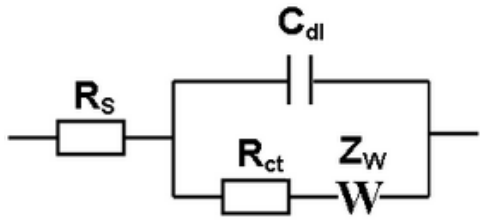

Figure 7.7: Randles circuit.

frequency- dependent impedance, $Z(\omega)$, follows this function:

$$Z(\omega) = R_s + \frac{R_p + \sigma\omega^{-1/2}}{\sigma\omega^{1/2}(C_d+1)^2 + \omega^2 C_d^2 (R_p + \sigma\omega^{-1/2})^2} + \\ + j\frac{\omega C_d (R_p + \sigma\omega^{-1/2})^2 + \sigma\omega^{-1/2}(\sigma\omega^{1/2}C_d + 1)}{(\sigma\omega^{1/2}C_d+1)^2 + \omega^2 C_d^2 (R_p + \sigma\omega^{-1/2})^2} \tag{7.10}$$

where

$$\sigma = \frac{RT}{\sqrt{2}n^2F^2A\left(\frac{1}{D_O^{1/2}C_O(x,t)} + \frac{1}{D_R^{1/2}C_R(x,t)}\right)}$$

with A the area of the electrode, $C_O(x,t)$ and $C_R(x,t)$ are the concentrations of oxidated and reducted species at the distance x from the electrode surface, and at time t. At high frequency, the expression 7.10 can be reduced to

$$Z(\omega) = R_s + \frac{R_p}{1+\omega^2 R_p^2 C_d^2} - j\frac{\omega R_p^2 C_d}{1+\omega^2 R_p^2 C_d^2} = Z^{'}(\omega) - jZ^{''}(\omega) \tag{7.11}$$

whereas, at low frequency, 7.10 becomes

$$Z(\omega) = R_s + R_p + \sigma\omega^{-1/2} - j(\sigma\omega^{-1/2} + 2\sigma^2 C_d) \tag{7.12}$$

In the Nyquist plot (Z' versus Z''), we can identify the semicircle described by the equation 7.11, at high frequency, and the straight line described by the equation 7.12, at low frequency.

Chemical and Biological material

The materials involved into the realization of the (bio)sensor were: Poly(thymine), Cysteamine, Glutaraldehyde, Limonene.

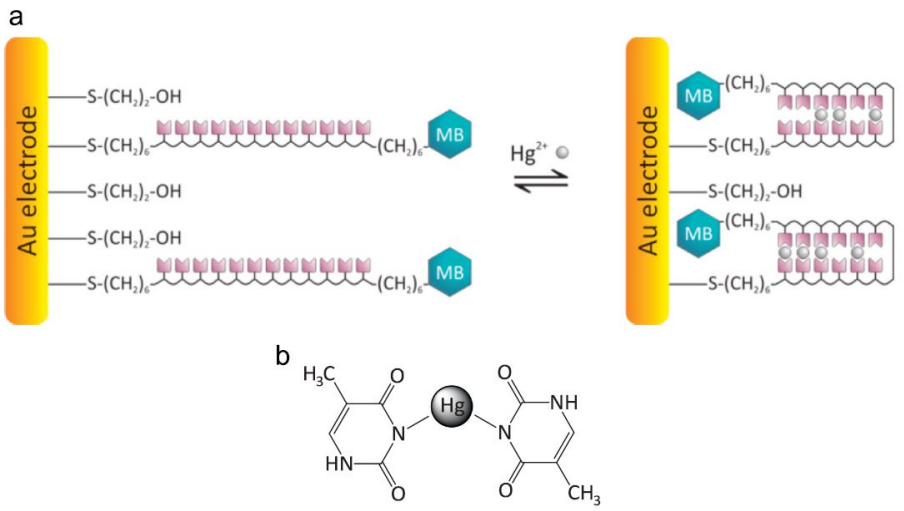

Figure 7.8: Poly(thymine)-Hg biosensor functioning principle (a) and structure of complex Thymine-Hg-Thymine (b).

- The *Poly(thymine)* is a chain of variable odd number Thymine nucleotide (T), one of the four nucleobases of the nucleic acid of DNA, together to Adenine (A), Guanine (G), Cytosine (C). In DNA, the Thymine binds to Adenine via two hydrogen bonds,

while in RNA Thymine is replaced by Uracil (U). An alternative name for Thymine is 5-methyluracil because it is derived by the methylation of uracil at 5th position. Thymines, in the Poly(thymine) chain, act as bridges in forming diester linkages between the deoxyribose moieties. In presence of Hg, Thymine creates a complex T-Hg-T more stable of T-A, furthermore, the Poly(thymine) chain changes its conformation, passing from straight to a "hairpin" configuration (Fig. 7.8).

- The *Cysteamine* (Cys, β-mercaptoetilamina) is an aminothiol with formula $HSCH_2CH_2NH_2$ (Fig. 7.9), showing the aminic group, $-NH_2$, and the thiol group, -SH. It is the result of the degradation of the amino acid cysteine that loses a carboxylic group, and in standard temperature, it presents itself in a solid malodorous state. The -SH group shows high affinity with gold. Cysteamine was purchased from Sigma-Aldrich.

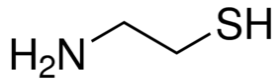

Figure 7.9: Skeletal formula of Cysteamine.

- The *Glutaraldehyde* is an organic compound with formula $CH_2(CCH_2CHO)_2$ (Fig. 7.10). It is colorless and emits a strong smell. Generally, it is available in an aqueous solution where the aldehyde groups are hydratated.

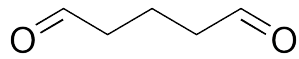

Figure 7.10: Skeletal formula of Glutaraldehyde.

- The *Limonene* is an hydrocarbon with formula ($C_{10}H_{16}$) (Fig. 7.11), classified as a cyclic terpene. Its name is due to the limon, because limonene is included into citrus fruit (orange, limon, etc).

It is in liquid and colorless state. Limonene is a chiral molecules that bind with the -SH group. Limonene is a molecules sensitive to Hg, additionally it changes color in its presence.

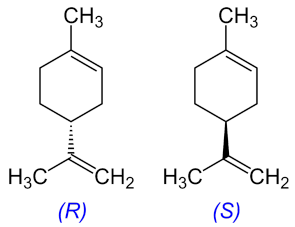

Figure 7.11: Skeletal formula of Limonene.

7.3 Development of the CNR-IIA Impedimetric active sensor for Hg in wet deposition

A comparison between methods of deposition of organic molecules over a substrate (gold, glass, silicon, ceramic materials as well as Al_2O_3, TiO_2, ZnO_2 et cetera) was conducted. In this work, the Cysteamine was deposited over the gold three- electrodes through the Self-Assembled Monolayer (SAM) technique and the Electrochemically Deposed Multilayers (EDMs). A flow system in wet deposition has been used to perform the analysis. The flow system in water was based on the sensor built *ad-hoc* set into the Micrux batch cell, where the treatments and the analysis were conducted. The analysis of cleaning, deposition, and the impedance spectra, were conducted through the potentiometer-voltmeter and impedance analyzer, the PalmSens3.
Before of the deposition, the substrate (Au electrodes) was cleaned with cyclic voltammetry (CV) at ±1.2 V vs Ag/AgCl pseudo-RE in H_2SO_4, 0.1 M (Scan rate=1 V/s, Estep=5 mV) (Fig. 7.12). Although the implementation of SAM technique is extremely easy, an overnight treatment of the thiol (Cys, 20mM) is required. The realization of

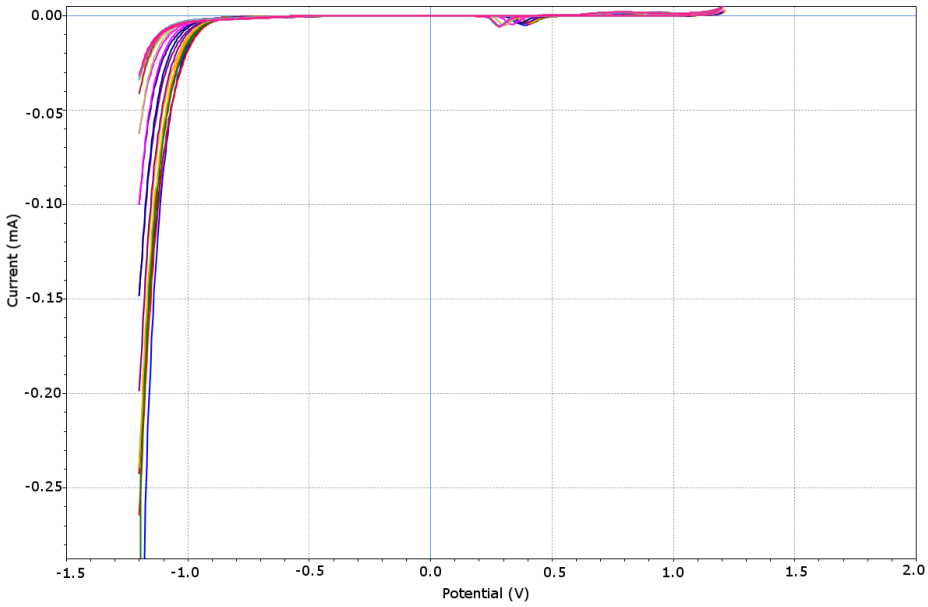

Figure 7.12: Cyclic Voltammogramms of a gold three-electrode.

SAM deposition happens diving the electrode in a solution of Cys and leaving it on an oscillation shaker overnight. By this way, SAMs are deposed not only on the working electrode (WE) but also on reference (RE) and auxiliary (AE) ones.
Electrochemically Deposed Multilayers (EDMs) are commonly adopted in our lab (Vastarella et al. [2007], Maly et al. [2005, 2004]) for immobilization of molecular structures in order to obtain (bio)sensors for several analytes. Generally, the EDMs request 20 minutes to realize an optimal deposition, but really the deposition happens in few seconds. Hence, we tried to realize the EDMs by chronoamperometry at +1.3 V vs RE in thiolated solution for 50 s (Fig. 7.13) to verify its proprieties. Electrochemical Impedance Spectroscopy (EIS) has been performed on two electrodes, before and after the thiol deposition in both methods, in equimolar potassium hexacyanoferrate

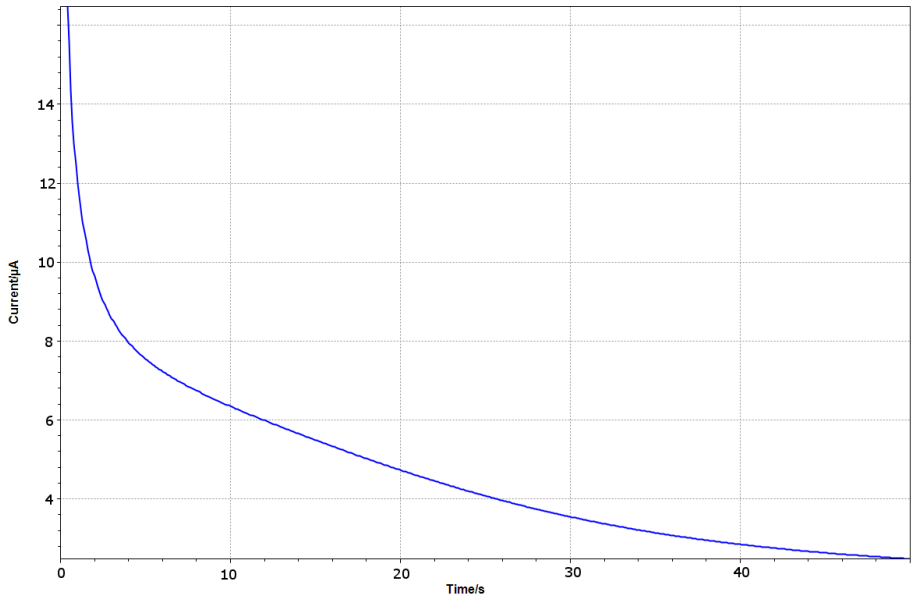

Figure 7.13: Chronoamperometry for EDMs of Cys.

$K_3[Fe(CN)_6]/K_4([Fe(CN)_6]$ 0.1 M, at 0.0 V vs RE and with an alternate potential of 10 mV exploring a frequency range between 1 Hz and 20 kHz. The Fig. 7.14 shows an increase of impedance curve after the Cys's deposition. Moreover, the EDMs of Cys are characterized by a higher impedance due to the larger quantities of deposited materials. After the impedance analysis, a surface analysis was performed by Atomic Force Microscopy (AFM, a Nanosurf Flex-ANA) in tapping mode. By comparison of the impedance spectra for SAMs and EDMs, we can deduce that EDMs shows higher impedance values (Fig. 7.14), on the other hand, thanks to AFM images, we establish that EDMs is thicker (Fig. 7.15) than SAMs. SAM shows Au electrodes poorly covered with a thinner film with holes where the bare Au electrode is exposed (poor electrochemical performances of further obtained biosensors). On the contrary, the substrate covered with EDMs shows a more homogeneous and smooth surface, as well is confirmed by

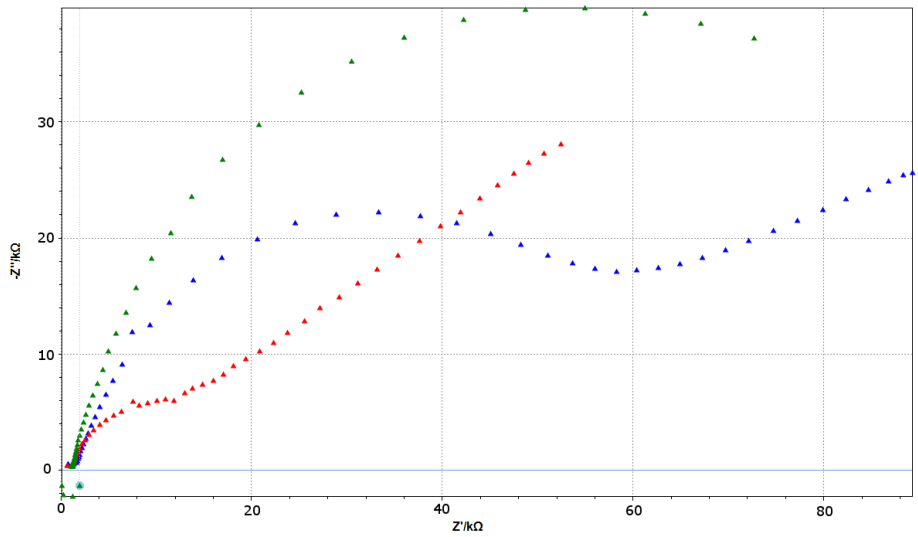

Figure 7.14: EIS of bare electrode (red), SAM of Cys (blue), and EDMs of Cys (green).

the values of roughness higher for SAM than EDMs (Tab. 7.1). After

Table 7.1: Comparison between roughness and waviness values for SAM and EDM.

	SAM (nm)	EDM (nm)
R_a(Average Roughness)	1.37	0.56
R_s (Highest Peak)	8.35	2.02
R_p (Deepest Valley)	6.48	1.91
$R_t = R_v + R_p$ (Total Roughness)	14.83	3.93

the study of the two methods of deposition on the electrodes useful to establish the advantages and disadvantages of each, the two attempts

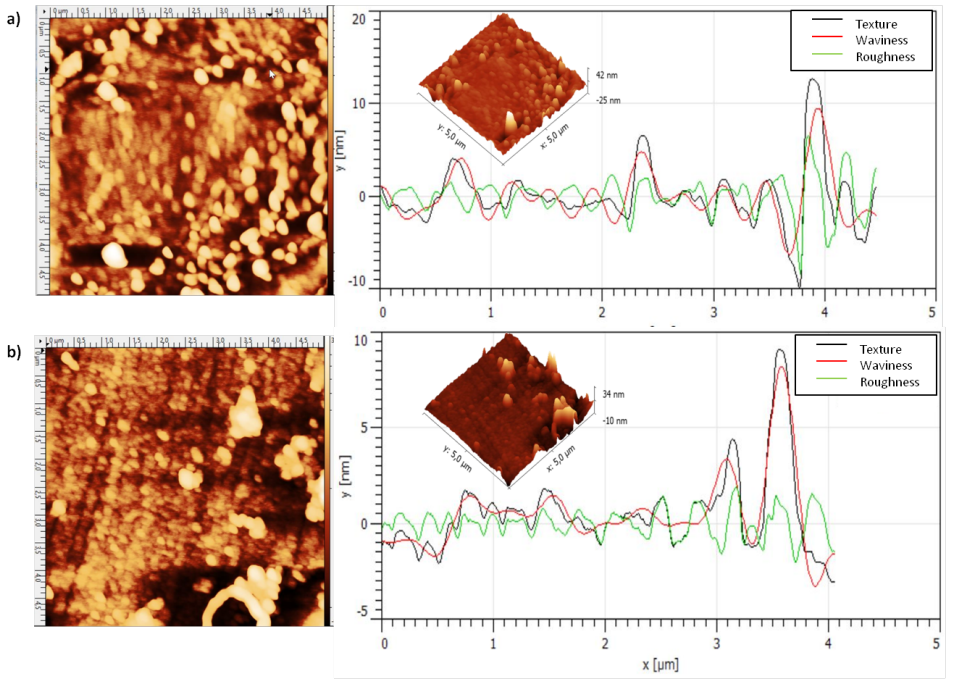

Figure 7.15: AFM scans: topographies, 3D views and roughness parameters of SAMs, a), and EDMs on AuWE, b).

to realize sensor sensitive to Hg have been made, using Poly(thymine) and Limonene.

7.3.1 Poly(thymine)-based Sensor for Hg

The Poly-T deposition was made with a 0.4 μM solution by self-assembling overnight or by chronoamperometry at +1.3 V vs RE (1200 s). Successively, a EIS of the electrode with Poly-T was performed. Some Hg treatment, which modified the Poly(thymine) configuration, were made exposing the bare electrode to a solution of $HgCl_2$ of increasing concentration (5 ppq, 10 ppq, 15 ppq) (Fig. 7.16). Although an initial decrease of impedance was evident after the first treatment

(5 ppq $HgCl_2$), did not happen an increasing impedance corresponding at increasing concentrations of $HgCl_2$, leaving to think about a rapid saturation. Moreover, it was interesting to verify a response in presence of $HgCl_2$ that confirmed the interaction with Poly(thymine). Exploring better this method, we could obtain good results, for example establishing the range of response and the limit of detection. Other experiments, i.e. reducing the Hg concentration, are in progress. Furthermore, the propriety of a good sensor should be the chance to reuse it, so the analysis to "clean" the Hg from the sensor are in progress too.

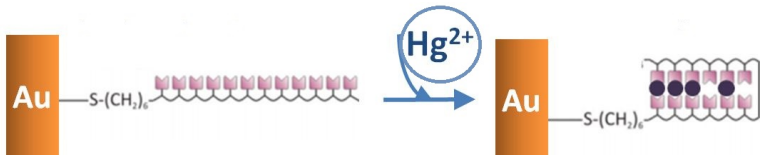

Figure 7.16: Hg treatment over active impedimetric Poly(thymine)-based sensor.

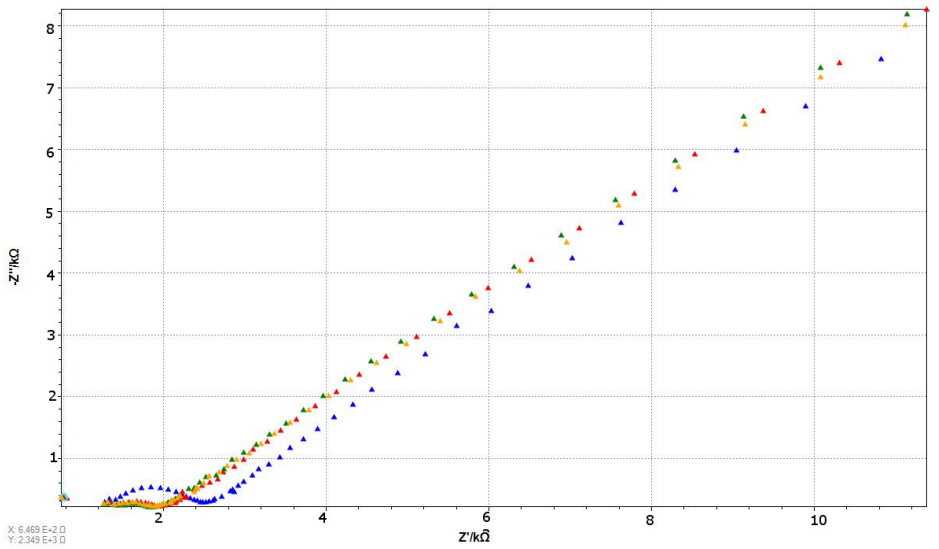

Figure 7.17: EIS for Hg treatment over active impedimetric Poly(thymine)-based sensor (blue: bare electrode; red: 5 ppq $HgCl_2$, green: 10 ppq $HgCl_2$, yellow: 15 ppq $HgCl_2$).

7.3.2 Limonene-based Sensor for Hg

Limonene was bound to the electrode after other treatment with Cysteamine and Glutaraldehyde. In fact, the Cysteamine linked to gold thanks to the -SH group. It was possible to realize the binding with both SAM or EDM. After this treatment, it was exposed to Glutaraldehyde 12.5% for 1 hour, where the group -CHO of Glu bound with $-NH_2$ of Cys. Successively, another treatment of 1 hour in Cys was performed, where the other group of Glu -CHO bound with $-NH_2$ of the new Cys, leaving free the -SH group. Then, a treatment with a drop of Limonene set under UV lamp for 3 hours was conducted. In this way, Limonene bound to -SH of free Cys (Fig. 7.18). Biosensors with Limonene showed a better impedimetric response, with a decreasing impedance increasing the Hg concentrations (Fig. 7.19). Hence, a preliminary calibration curve was realized (Fig. 7.20). This optimal

result could represent a starting point into the development of sensors for wet deposition. Moreover, further analysis are need to confirm the correct principle of operation, and eventual interferences.

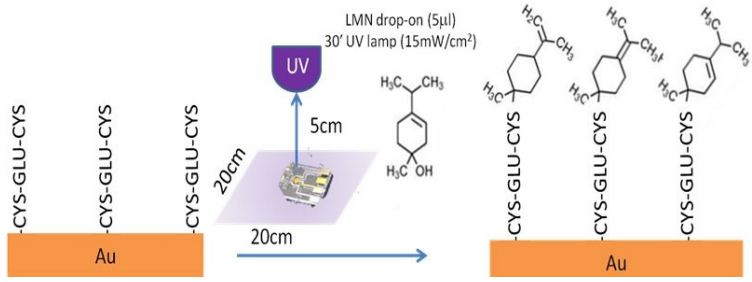

Figure 7.18: Hg treatment over active impedimetric Limonene-based sensor.

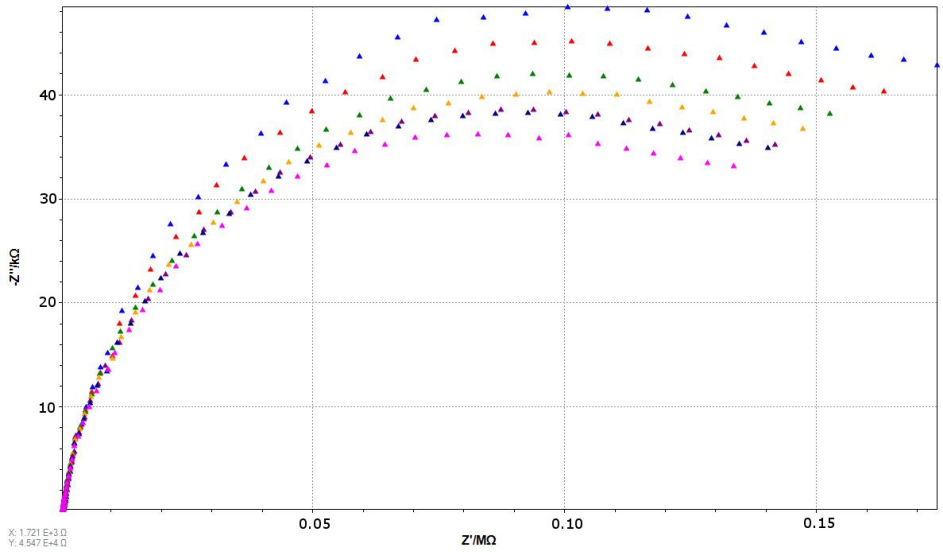

Figure 7.19: EIS for Hg treatment over active impedimetric Limonene-based sensor (pink: 0.1 ppq; purple: 0.25 ppq, darkblue:0.50 ppq, yellow: 1 ppq, green: 2 ppq, red: 4 ppq, blue: 5 ppq).

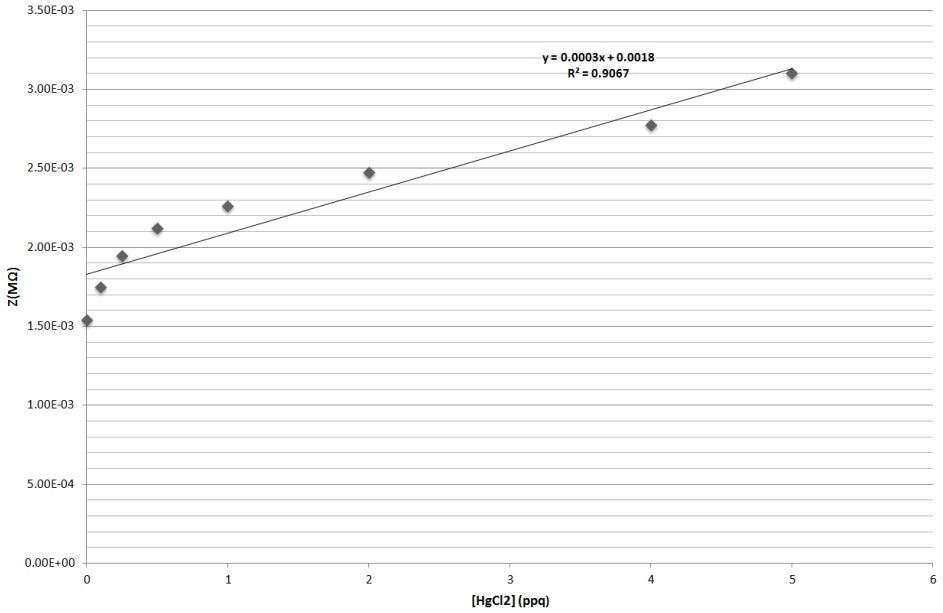

Figure 7.20: Calibration curve of limonene-based sensor.

7.4 Conclusions

The increasing need to understand the Hg processes, especially its transformation in wet deposition, is encouraging the scientific community to develop sensors that will allow a monitoring over a larger scale. The crucial problem of Hg is its presence in water, where the methylation could cause the human intoxication, in addition to the substantial damages to ecosystems. In this work, we investigated about possible user-friendly Hg sensors based on the impedance spectroscopy. The impedance spectroscopy is a technique relatively easy to implement. The idea on which are based our sensors is the observation of an impedance variation of a sensor built *ad-hoc*. We proposed two different schemes of functionalization of a gold three - electrode.
The first sensor would like to use the interaction of Poly(thymine) with Hg, which causes a change of the configuration of the DNA-chain. As expected, we recorded an impedance variation depending on the

changes of the functionalized substrate. However, the sensor seems to reach easily the saturation (after 5 ppq). Further measurements could allow establishing the limit of detection of the built sensor and its field of application depending on the detectable concentrations.
The other proposed sensor is based on the proprieties of binding of Limonene with Hg. This sensor showed promising results which allowed plotting a preliminary curve of calibration. Moreover, further measurements should demonstrate if there are potential interferents in presence of other chemical molecules and/or meteorological parameters.
In conclusions, this results could represent a starting point into the development of sensors for Hg deposition. Certainly, there is still a hard work to establish, at first, the validity and the efficiency of these sensors in our laboratories, and then, their robustness on field.

Chapter 8

Conclusions

Mercury (Hg) is a toxic heavy metal with an appreciable volatility, which causes its state in the gas phase at ambient temperature and pressure. In air, Hg could be found in three different species: the Gaseous Elemental Mercury (Hg0, GEM), the Gaseous Oxidized Mercury (GOM), which represents the oxidized form (Hg^{2+}), and Particulate Bound Mercury (Hg(p), PBM). Both species GEM and GOM are in gaseous form, and their sum is indicated as Total Gaseous Mercury (TGM). Moreover, GEM and GOM could be bind to the particulate present in air, producing the PBM. While the GOM and PBM have a short residence time in the atmosphere (about 1-7 days), during which they can be transported on local scale, GEM shows a residence time of approximately one year (Hall, 1995, Shia et al., 1999), thus allowing a GEM long-range transport on hemispheric scale.
Hg also implies negative consequences on both ecosystem and human health, hence, in the last decades, the scientific community attention is focusing on the need of a global perspective, in both research, monitoring and policy making. The first goal of the policy making is to reduce the anthropogenic emission of Hg, hence, since 2002, the UNEP (United Nations Environment Programme) Mercury Program was adopted to monitor Hg. Successively, in 2005, the UNEP Global Partnership for Mercury Air Transport and Fate Research (UNEP-MFTP) was signed and adopted by Italy, Canada, Japan, South Africa,

United States, Electric Power Research Institute (EPRI), Natural Resources Defence Council (NRDC) and UNEP. The UNEP-MFTP encourages the member states to a major collaboration, to understand the gap of knowledge about Hg emissions, and its chemical-physical processes, especially in wet deposition and in the flux between air/sea. In 2010 the Global Mercury Observation System (GMOS) Project was founded by the European Commission to create a network of global monitoring for Hg that included more of 40 ground-based stations, plus oceanographic campaign *ad-hoc* and air-craft measurements. The GMOS goal was to gather globally the information about Hg, suggesting the principal method of measurements, and verifying the quality of data. The GMOS Project recommended the use of two instruments for the TGM measurements, the Tekran and the Lumex, where the Tekran instrument is based on the Cold Vapor Atomic Fluorescence Spectrometry (CVAFS), while the Lumex is based on the Cold Vapor Atomic Absorption Spectrometry (CAAFS) with the Zeeman background correction, which eliminates the interfering impurities. The monitoring for Hg speciation (GEM, GOM, PBM) is performable only with the Integrated System of Tekran (Oxidized Tekran Speciation Module for GOM and Particulate Mercury Unit for PBM). During the GMOS Project, a team of experts of field, including the technicians of the Tekran Instrument Corporation and Lumex, established the Standard Operative Procedures, to strengthen the correct use of instruments by all technicians involved into the various monitoring stations.
Within the GMOS Project, the ground-based stations has been divided into Master and Secondary station. The Master monitoring stations perform the speciated measurement (GEM, GOM, PBM) and collect precipitations for the Hg in wet deposition, while the Secondary monitoring stations perform the only TGM/GEM monitoring, with the sampling of precipitations even for the Hg in wet deposition.

8.1 Summary of key findings

In the framework of the GMOS global network, continuous records of GEM concentrations have been measured at a ground-based monitoring Station of the GMOS network, the GMOS EMMA station, established inside Nahuel Huapi National Park, Bariloche, Argentina. In particular, for the purposes of this Thesis 4-year of GEM data (2012-2016) recorded at this Argentinean station have been statistically managed and analyzed. GEM values concentrations ranged from 0.23 and 1.43 ngm^{-3} with a mean value of 0.87 $\pm$ 0.15 ngm^{-3}. This value is lower than Hg background in the Northern Hemisphere, but included into the range until now observed for the measurements in Southern Hemisphere (0.84 -1.03 ngm^{-3}) (Sprovieri et al. 2010a,b; 2016a; Slemr et al., 2015; AMAP/UNEP, 2015; Angot et al., 2016). Moreover, a discussion of the GEM concentration distribution and its seasonal and daily pattern has been provided. We identified high values for GEM especially in spring and winter, and a daily increase of GEM during the day-time. Furthermore, we evaluated the influence of local environmental parameters on GEM behavior, and, the potential sources of the atmospheric Hg transported by air masses using backward trajectory analysis, highlighting that the air masses passing through the Andes, where several volcanoes of Cordillera are set, have been observed in conjunction with peaks in GEM levels. A manuscript has also been published in Atmospheric Chemistry and Physic Discussion (ACPD) on this issue (Diéguez, M. C., Garcia, P. E., Bencardino, M., D'Amore, F., Castagna, J., Ribeiro Guevara, S., and Sprovieri, F.: Four years of atmospheric mercury records in Northwestern Patagonia (Argentina): potential sources, concentration patterns and influence of environmental variables observed at the GMOS EMMA station, Atmos. Chem. Phys. Discuss., https://doi.org/10.5194/acp-2016-1076, 2017.).

As part also of the GMOS observational network, an oceanographic cruise campaign was carried out during summer 2015 in the Western sector of Mediterranean Sea basin, on-board the research vessel "Minerva Uno" of the Italian National Research Council (CNR). The overall

goal was to investigate the dynamic patterns of mercury in the Marine Boundary Layer (MBL) and the main factors affecting mercury behavior at both coastal and offshore locations. The mean concentrations of the recorded Hg species were $1.6 \pm 0.5\ ngm^{-3}$, $11.8 \pm 15.0\ pgm^{-3}$, and $2.4 \pm 1.1\ pgm^{-3}$, respectively for GEM, GOM, and PBM. During the measurement period typical fair-weather conditions of the Mediterranean summer were encountered with high levels of solar radiation and temperature that favored photochemical reactions. Atmospheric pollutants such as ozone, sulphur oxides and nitrogen oxides and other meteorological parameters were in addition recorded and jointly discussed with selected mercury events in terms of their spatio-temporal variations. Changes in air pollutant concentrations were also argued in the light of their likely influencing sources. We identified five events with peaks of one or plus Hg species, in combination with some chemical parameters (O_3, NO_x, SO_2). Two of the recorded events were attributable to, anthropogenic activities, such as the industrial area of the Gulf of Genoa and the mercury cell chlor-alkali complex in Tuscany, Italy. The other events have been linked with the natural influence, like the wildfires near the Sardinia, the volcanic ashes, detected around the Aeolian area and the in-situ production of reactive gaseous mercury within the Marine Boundary Layer. The results obtained during this cruise campaign has been published in Atmospheric Environment (Castagna, J., Bencardino, M., D'Amore, F., Esposito, G., Pirrone, N., Sprovieri, F., Atmospheric mercury species measurements across the Western Mediterranean region: Behaviour and variability during a 2015 research cruise campaign, Atmospheric Environment (2017), doi: 10.1016/j.atmosenv.2017.10.045.).

From a global perspective, an observational network as that provided on global scale within the GMOS project, is essential in supporting a good spatial resolution of mercury measurements worldwide to better understand the Hg cycle in the environment. On the other hand, a global network infrastructure is also complicate and expensive, especially at remote locations and in developing countries. Also for this reason, in recent years the scientific community is trying to develop technologies and new sensing systems to detect Hg at lower operating

costs. The principal need is to realize a sensor able to collect TGM, and additionally, if possible, also the two other mercury species in air (GOM and PBM). The principal proprieties of these sensors should be the robustness, the traceability, and no request of gas carrier, energy supply or highly qualified technical expertise.
Among sensors, the Passive Air Samplers (PASs) could represent the appropriate solution in the detecting of Hg, because they could be deployed in high numbers, in remote areas without source of electricity or in locations where the costs and logistic of active sampler deployments can be prohibitive.
In this Thesis work, the study performed on the development of new Hg passive samplers and the results of two seasonal sampling campaigns at selected GMOS ground-based monitoring sites is reported in order to compare the new Hg PASs samplers with active sampling system commonly used worldwide.
The sampling technique was based on the property of molecular diffusion of gases through a diffusive surface into the sampler. The sampler had a diffusive barrier that created a stagnant region over the collection surface. We investigated about the more efficient absorbing material, based on either nanofibers and nanoparticles. The proposed absorbing material was realized by electrospinning the nanofibers of titanium oxide, which successively were functionalized with gold nanocluster.
After the development of the PASs in its laboratory, the CNR-IIA proposed the test on field in five GMOS monitoring stations, where Hg was monitoring through conventional systems (Tekran or Lumex). The monitoring stations chosen were Mount Curcio, Italy (MCU), Mount Ailao, China (MAL), and Listvyanka, Russia (LIS), for the Northern Hemisphere, and Cape Point, South Africa (CPO) and Bariloche, Argentina (BAR), for the Southern Hemisphere. Except for LIS, where Lumex had monitoring TGM, in the other stations the Tekran was used. Two seasonal comparison campaign were performed; each campaign consisted of 6 weeks. Two PASs were co-exposed in parallel for two or three weeks, meanwhile, two blanks PASs were exposed with the closed caps for the whole campaign.

The two comparison campaigns between PASs and Tekran/Lumex analyzers showed acceptable results in all sites. The best results were recorded by the MCU site, with the data of the two systems in agreement for both campaigns (TK: 1.16 $\pm$0.16 ngm^{-3} and 1.37 $\pm$0.28 ngm^{-3}; PASs:1.15 $\pm$ 0.12 ngm^{-3} and 1.02 $\pm$ 0.12 ngm^{-3}). At CPO station the results were the worst, with the PASs system that has showed Hg concentration significantly higher than Tekran's data (TK: 0.92 $\pm$ 0.07 ngm^{-3} and 0.97 $\pm$ 0.08 ngm^{-3}; PASs: 1.74 $\pm$ 0.20 ngm^{-3} and 3.72 $\pm$ 0.6 ngm^{-3}). However, the CPO campaigns were not representative due to uncorrected management and closure of samplers, and the wrong storage and shipping (one Ziplock bag instead of three). Moreover, these results could be influenced by the local conditions (i.e., dust, high wind speed, etc.). In fact, several samples of CPO showed dust inside the vials that potencially influenced the diffusion over the absorbing material.
Finally, the results of the comparison in light to the meteorological condition for the MCU case have been analyzed. In fact, meteorological parameters could influence the diffusion of air during the sampling or the efficiency of absorbing and detaining Hg. The behavior of Hg PASs seemed to follow the pattern of the air temperature and of the wind speed, but the data were not enough to establish a statistical correlation.
The last part of the research work of this Thesis was about the development of new sensors for Hg in wet deposition. The Hg in wet deposition is a crucial problem, because it could be transformed in methylmercury that bioaccumulate and biomagnificate into the fishes, which will enter into the food web, reaching the mankind. Methylmercury causes a toxic effect, i.e. the damages mainly on the nervous systems, the alteration of immune systems and kidneys, the teratogen effect during the pregnancy. The proposed sensors would like to use the impedimetric analysis of three-electrode functionalized *ad-hoc*, to be sensitive to Hg in wet deposition. A preliminary study to choose the more appropriate method to deposit thiols on the gold three-electrode surface was conducted, comparing the advantages and the disadvantages of the Self Assembled Monolayer (SAM) and of the Electrochemically Deposed

Multilayers (EDMs). Although the SAM showed a thinner layer of deposition than the EDMs, for our realizations, we preferred this last method due to the short time (50 s instead of an over-night treatment) with good results of the multilayers deposited that appeared without holes and with a smooth surface. The results of this comparison were presented at the Third National Conference on Sensors (Proceedings of the Third National Conference on Sensors, February 23-25, 2016, Rome, Italy, DOI: 10.1007/978-3-319-55077-0_22). Successively, we realized two types of functionalized sensors for Hg. The first sensor developed, was based on the deposition of the Poly(thymine) that in presence of Hg^{2+} modified its configuration, passing from the straight form to an "hairpin". The conformational change corresponded to a variation of impedance, but after the first Hg treatment (5 ppq) we recorded a saturation. Further analysis could demonstrate if it is possible to obtain a linear response increasing Hg concentration, but starting from a lower value. The second proposed sensor was Limonene-based. The Limonene reacts with Hg^{2+}, and the chemical binding is evident due to the chromatic change of the solution. At the increasing of the Hg^{2+} treatments, the Limonene-based sensor showed an increase of the impedance. Moreover, thanks to the good results obtained, a preliminary calibration curve was built. The principle of operation of the Limonene-based sensor seemed to work very well, hence this result could represent an optimal start point into the development of sensor in wet deposition.

8.2 Recommendations for Future Work

The knowledge of Hg, reached until now, presents several gaps, especially into its various processes of transformation that are still unclear. Modelers are trying to simulate the cycle of Hg, but there are many open questions about the reactions that only the study of Hg measurements could resolve. In fact, the constant rates of reactions are still variable, and many processes of emission, like as the biomass burning or volcanic eruptions, and/or remission, mainly from the water basins,

are unknown. Moreover, the methylation process, which represents the most warning issue, need of further investigation.
In this work, two different interesting case studies were presented: the ground-based site in Bariloche (Argentina), and an oceanographic campaign, which allowed to give some precious information about the Hg emissions and/or process in two different contexts, the Boundary Layer in a site of the Southern Hemisphere, and the Marine Boundary Layer (MBL) in the Mediterranean Sea. However, only with further analysis of the Hg measurements, the knowledge about Hg will be extended. The GMOS Network will guarantee the Hg monitoring series recovering uniformly the globe, and including strategic sites, like as polar areas or sites with interesting air-cross.
Regarding the Passive samplers, the results obtained by the developed sensors are good and promising. However, additional field performance tests are need to confirm their robustness, especially their repeatability and precision. Further experiments could suggest the Sampling Rate (SR) in which the PASs have a better efficiency. In fact, the preliminary studies of 1st comparison campaign seemed suggest that increasing the sampling period, the PASs efficiency improved. A longer period of deployment at a monitoring site could improve the method that, although usually showed acceptable results, sometimes failed. Further measurements could allow to establish with precision the reasons of the PASs' failures, and if these influences could be avoided in future. For example, as result of these campaign, is clear that the method of sampling (i.e. the shelter) should be improved to better protect the devices from the local condition (dust, high wind speed, etc.). Moreover, further investigations are necessary to affirm if the physical parameters of the environment, such as temperature fluctuations and UV-light, as well as chemical ones, such as volatile organic compounds and gas (like halides and sulphides) could influence the PASs response, interfering with the absorption process of Hg.
Finally, the results hereinbefore of the investigated sensors for wet deposition are promising for future development. Surely, further measurements could establish the correct principle of operation, for both the proposed sensors. For the Poly(thymine)-based sensor, many work

should be done, because although a response has been observed after the Hg^{2+} treatment, its saturation could represent an impediment into the development. However, for the future, it is essential to establish the limit of detection of the Poly(thymine)-based sensor. On the other hand, the Limonene-based sensor showed already good results, allowing to graph a curve of calibration. The second step into the development of this kind of sensors, will be to experiment if there are other molecules in wet deposition that could interfere with the signal due to Hg. In fact, the fundamental propriety of this sensors is to be sensitive only to Hg^{2+}, excluding other response in presence of some interferents, as well as Fe, Cu, Zn, etc, which could be present into wet deposition. Finally, if the lab tests will be positive, some tests of comparison with the conventional method to measure Hg in wet deposition (i.e. Tekran 2700) will be need.
In conclusion, in this work of thesis, many results about possible future sensors for Hg in air and in wet deposition had been presented. Moreover, further investigations are need to confirm if they will be able to substitute the conventional methods. In this way, the monitoring for Hg will be possible also in remote areas and in sites where actually the conventional analyzers cannot work. As final results, the employment of Passive Sampler could strengthen the Hg GMOS Network increasing the number of sites of investigation chosen considering all the possible geographical and meteorological conditions.

Appendix

Abstracts for Conferences

In this appendix, I reported some abstracts for Conferences about other subject matters not dealt in the work thesis. The first work was presented at the "European Geosciences Union (EGU) 2016", the second one at the "Convegno Nazionale sul Particolato Atmosferico 2016", while the last at the "European Geosciences Union (EGU) 2017". This works showed the preliminary results successively deeped to realize an article for journal that actually is in submission.

Variability of fine and coarse aerosol over the Western Mediterranean Basin during the Minerva 2015 research cruise campaign

Jessica Castagna (1), Francesco Carbone (1), Attilio Naccarato (1), Sacha Moretti (1), Giulio Esposito (2), Mariantonia Bencardino (1), Francesco D'Amore (1), Francesca Sprovieri (1), and Nicola Pirrone (2)
(1) CNR-Institute of Atmospheric Pollution Research, Division of Rende, Italy (j.castagna@iia.cnr.it), (2) CNR-Institute of Atmospheric Pollution Research, Montelibretti, Rome, Italy (pirrone@iia.cnr.it)
The Mediterranean Basin, due to its semi-enclosed configuration, is heavily affected by air pollution and it is becoming, in the last years, a region of particular interest of study for its implications regarding both health effects and environmental impacts. The area is surrounded by a densely populated as well as industrialized coast, and even affected by

natural sources. So, it is important to know how the various sources contributes to increase air pollution levels and discriminate among them. With special regard to aerosol pollution, natural sources, like Saharan dust, volcanoes, and fires, as well as anthropogenic sources, such as industry, road and marine traffic, and fuel combustion from heating, can equally increase the values of this dangerous pollutant. While on the land we can find numerous monitoring sites, there are not continuous measurements on the sea. For this reason, since 2000 the Institute of Atmospheric Pollution of the National Research Council (CNR-IIA) is conducting regular oceanographic campaigns of measurements in the Mediterranean Sea. In this context, here we report the results obtained during the last cruise campaign, which took place in the Western Mediterranean sector and was conducted on-board the Italian research vessel Minerva during summer 2015 (from June 27th to July 13th). Fine (PM2.5) and Coarse (PM2.5-10) particulate size fractions were collected on PTFE membrane filters (Advantec MFS) and their mass concentrations determined gravimetrically. Successively, all the filters were digested with a mixture of HNO3/H2O2 in an microwaves digestion system and then analyzed by ICP-MS for the determination of the major and trace elements. Outcomes regarding the particulate mass concentration, the content and the distribution of the analyzed elements over both PM size fractions will be discussed taking into account potential contributing sources as well as different meteorological conditions.

Variability of fine and coarse aerosol over the Western Mediterranean Basin during the Minerva 2015 research cruise campaign

Jessica Castagna[1,*], Francesco Carbone[1], Attilio Naccarato[1], Sacha Moretti[1], Giulio Esposito[2], Mariantonia Bencardino[1], Francesco D'Amore[1], Francesca Sprovieri[1], and Nicola Pirrone[2]

[1]CNR-Institute of Atmospheric Pollution Research, Division of Rende, Italy, [2]CNR-Institute of Atmospheric Pollution Research, Montelibretti, Rome, Italy, *Corresponding Author: jessica.castagna@iia.cnr.it

1. The research cruise campaign

The Mediterranean Sea is surrounded by an area densely populated with a high level of industrialization, which is contributing to air pollution from anthropogenic sources in addition to already present natural sources like Saharan dust, emissions from active volcanoes and wildfires.[1]

The Institute of Atmospheric Pollution of the National Research Council (CNR-IIA) is conducting periodic measurements campaigns to understand processes and influences of various sources on the Mediterranean Basin, focusing, among others, on the Particulate Matter (PM) air pollution.[2]

The 2015 cruise campaign was conducted during the summer (26th of June to 13th of July), in the Western Mediterranean, starting from Sicily (Palermo); the route and the anchorage sites are shown in **Fig. 1**. Except for Cagliari, MA2 and B. Bonifacio, in which the anchorages were made in daytime, in all other cases, the anchorages were made at night.

2. Fine and Coarse Particulate

Measurements of *fine* ($PM_{2.5}$) and *coarse* ($PM_{2.5\text{-}10}$) were made with a sampling time of 24 hours on 47ømm Teflon filters, by using two High Volume Skypost (PM-HV). Filters were conditioned and weighted before and after sampling, the *particulate concentration* was thus obtained *gravimetrically*.

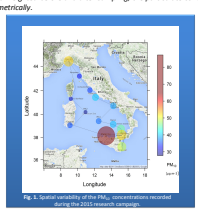

Fig. 1. Spatial variability of the $PM_{2.5}$ concentrations recorded during the 2015 research campaign.

PM_{10} ($PM_{2.5}$ + $PM_{2.5\text{-}10}$) concentrations are shown in **Fig. 1** from which it is possible to deduce that the larger concentrations (higher than the limit value of Italian Legislation, D. Lgs. 155/2010, equal to 50 μg m^{-3}) were sampled in the South of Italy and, as an exception in the North, in the Gulf of Genoa; both these areas are densely industrialized.

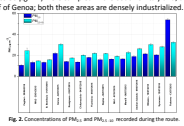

Fig. 2. Concentrations of $PM_{2.5}$ and $PM_{2.5\text{-}10}$ recorded during the route.

Measurements of $PM_{2.5}$ and $PM_{2.5\text{-}10}$, shown in **Fig. 2**, indicate a predominance of the coarser component during all the cruise, except for Palermo, where the fine particulate reached a value of 53.8 ± 1.1 μg m^{-3}.

3. Elements Concentrations

Teflon filters were digested with a mixture of HNO_3/H_2O_2 in an microwaves digestion system and then analyzed by *ICP-MS* for the determination of the *major and trace elements concentrations*.[3]

The sum of the elements concentration we analysed in $PM_{2.5}$ size fraction (**Fig. 3a**, upper) was lower than that we found for $PM_{2.5\text{-}10}$ (**Fig. 3b**, lower); we detected 0.8-6.8% and 3.1-8.9%, as elemental mass concentration, over the total mass concentration of $PM_{2.5}$ and $PM_{2.5\text{-}10}$, respectively.

$PM_{2.5}$ Elements

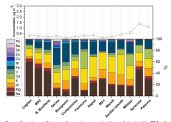

Fig. 3a. Sum of major and trace element concentrations detected in $PM_{2.5}$ (upper) and contribution of each element at the various sites (lower) (only elements with contribution >1% were reported).

A significative contribution of Fe, Zn and Pb was released in Genoa; the presence of Ba was released in Naples and an important contribution of Sb was observed near Milazzo.

$PM_{2.5\text{-}10}$ Elements

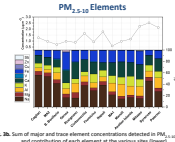

Fig. 3b. Sum of major and trace element concentrations detected in $PM_{2.5\text{-}10}$ (upper) and contribution of each element at the various sites (lower) (only elements with contribution >1% were reported).

The presence of Fe and Zn was released in Genoa and a little but important contribution of Sb was observed near Milazzo.

A receptor model, the *Positive Matrix Factorization (PMF)*, was applied to identify the principal PM contributing factors. The optimum number of factors, evaluated with Q-value, was 6. Thanks to the concentration of factors in each species (**Fig. 4a** and **Fig. 4b**), markers of possible sources were identified, establishing the nature of each factor.

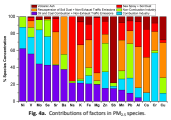

Fig. 4a. Contributions of factors in $PM_{2.5}$ species.

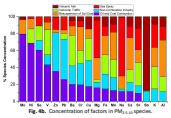

Fig. 4b. Concentration of factors in $PM_{2.5\text{-}10}$ species.

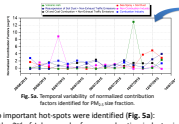

Fig. 5a. Temporal variability of normalized contribution factors identified for $PM_{2.5}$ size fraction.

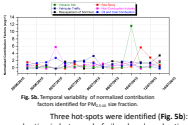

Fig. 5b. Temporal variability of normalized contribution factors identified for $PM_{2.5\text{-}10}$ size fraction.

Two important hot-spots were identified (**Fig. 5a**): on the 2nd of July, a peak of non-combustion industry in **Genoa** was detected and, on 10th of July, a peak of volcanic ash passing near **Vulcano** and staying in Milazzo was recorded. The last days (11th, 12th, 13th) an increase of sea spray and soil dust, due the rougher sea, was observed.

Three hot-spots were identified (**Fig. 5b**): on the 2nd of July, factors of non-combustion industry, and of oil and coal combustion showed a peak in **Genoa**; on the 6th of July, there was an increase of vehicular traffic factors in **Naples**; on 10th of July, a peak of volcanic ash near **Vulcano** and staying in Milazzo was recorded. Finally, on 11th of July, a peak of sea spray was aslo observed.

4. Conclusions

During the Minerva 2015 Research Campaign particulate measurements were conducted. The particulate coarser fraction ($PM_{2.5\text{-}10}$) was higher than finer component ($PM_{2.5}$). In 3 sites over 14, the particulate (PM_{10}) was higher than limit value of 50 μg m^{-3}. The major and trace elements were releaved using ICP-MS, and then the mainly influencing species at various sites were identified. Principal contributing factors were also determined with PMF and various hot-spots were highlighted, both of anthopogonic origins, like industry for Genoa or vehicular traffic for Naples, and natural sources, like volcanic ashes or sea spray. Further chemical analysis on particulate matter, like organic matter and ionic species, will allow us to better indentify the main PM contributing factors in the Mediterranean Basin.

References

1. **Bencardino, M., Sprovieri, F.** Ciliberti, S., and **Pirrone, N.** (2011) Variability of Atmospheric Aerosol and Ozone Concentrations at Marine, Urban, and High-Altitude Monitoring Stations in Southern Italy during the 2007 Summer Saharan Dust Outbreaks and Wildfire Episodes. Journal of the Air & Waste Management Association, 61, 952-967.
2. **Bencardino, M., Pirrone, N., Sprovieri, F.** (2016) Aerosol and ozone observations during ra cruise campaigns across the Mediterranean basin: temporal, spatial, and seasonal variability. Environmental Science and Pollution Research, 21, Issue 6, 4253-4268.
3. **Sprovieri, F., Bencardino, M.,** Ciliberti, S., and **Pirrone, N.** (2011) Chemical Composition of Aerosol Size Fractions at a Coastal Site in Southwestern Italy: Seasonal Variability and Transport Influence. Journal of the Air & Waste Management Association, 61, 941-951.

Particolato fine e grossolano rilevato nel corso di 10 campagne oceanografiche di ricerca nel Mar Mediterraneo

Jessica Castagna (1),*, Mariantonia Bencardino (1), Francesco Carbone (1), Attilio Naccarato (1), Valentino Mannarino (1), Sasha Moretti (1), Francesca Sprovieri (1), Nicola Pirrone (2)
(1) CNR-Istituto sull'Inquinamento Atmosferico, U.O.S di Rende, 87036
(2) CNR- Istituto sull'Inquinamento Atmosferico, Monterotondo, Roma, 00016 * Corresponding author. Tel: +39 0984 493027,
E-mail:j.castagna@iia.cnr.it
Keywords: Mediterraneo, particolato, frazione fine, frazione grossolana, variabilitÃ spaziale
Il Mar Mediterraneo è di particolare interesse sotto vari punti di vista poiché è un unico bacino che gode della combinazione di diverse caratteristiche meteorologiche, climatologiche e geografiche (1). L'atmosfera del Mediterraneo è a sua volta influenzata da masse d'aria, e dalle emissioni in esse contenute, che hanno origine non solo nell'Europa Centrale e nel Nord Africa, ma anche nell'Europa orientale e in casi eccezionali persino nel Sud Est Asiatico; a tal motivo, il Mediterraneo viene descritto come un "crocevia" di masse d'arie inquinate (2). Dal 2003, l'Istituto sull'Inquinamento Atmosferico del Consiglio Nazionale delle Ricerche (CNR-IIA), nell'ambito del progetto MEDOCEANOR, sta conducendo regolari campagne di misura, al fine di monitorare diversi inquinanti sul Mar Mediterraneo, incluso il particolato atmosferico (3,4). In questo lavoro, verranno presentati i dati relativi a 10 campagne oceanografiche condotte dal 2003 al 2015. Nello specifico, si tratta di 150 giorni complessivi di osservazione, durante i quali, insieme ad altri inquinanti atmosferici, sono state rilevate le concentrazioni di particolato fine e grossolano. I risultati mostrano un'ampia variabilità in entrambe le frazioni con un intervallo di valori misurati da 1.8 a 51.9 μgm^{-3} per le concentrazioni di particolato fine, e da 1.6 a 34.0 μgm^{-3} per quelle del particolato grossolano. I valori mediati su tutte le osservazioni svolte risultano simili e pari rispettivamente a 13.7 ± 7.9 μgm^{-3}

e a 13.6 ± 6.8 $\mu g m^{-3}$, per la frazione fine e per quella grossolana. La variabilità delle concentrazioni delle due frazioni di particolato campionate è risultata legata soprattutto alla distribuzione spaziale. Infatti, i livelli più alti di particolato grossolano sono stati registrati alle estremità del bacino, dove si verificano in particolar modo le intrusioni delle sabbie del Nord Africa e quelle derivanti dalla combustione di biomasse nell'Africa Subsahariana ed in Grecia. I livelli più alti di particolato fine, invece, sono stati osservati vicino le coste, dove maggiore è l'influenza dei poli industriali e delle aree portuali. Inoltre, il particolato fine ha mostrato un'ulteriore variabilità spaziale con valori più alti nel settore orientale del Mediterraneo, per via dei maggiori contributi delle numerose sorgenti antropogeniche ivi presenti. I risultati saranno analizzati tenendo conto della composizione chimica delle due frazioni di particolato rilevate, delle possibili sorgenti di emissione e dell'influenza delle varie condizioni meteorologiche.

Bibliografia

(1) H.J.Bolle (2003). Springer (ed), 5-86.
(2) J.Lelieved et al., (2002). Science, 298, 794-799.
(3) N.Pirrone et al., (2003). Atmospheric Environment, 37, 21-39.
(4) M.Bencardino et al., (2014). Environmental Science and Pollution Research, 21, 4044-4062.

Caratterizzazione del particolato atmosferico rilevato nel corso di 10 campagne di misura *off-shore* nel Mar Mediterraneo

Jessica Castagna[1,], Mariantonia Bencardino[1], Francesco Carbone[1], Attilio Naccarato[1], Valentino Mannarino[1], Sasha Moretti[1], Francesco D'Amore[1], Francesca Sprovieri[1], Nicola Pirrone[2]*

[1]*CNR-Istituto sull'Inquinamento Atmosferico, U.O.S di Rende, 87036*

[2]*CNR-Istituto sull'Inquinamento Atmosferico, Monterotondo, Roma, 00016*

**Corresponding author. Tel: +39 0984 493150, E-mail:j.castagna@iia.cnr.it*

1. Campagne di misure off-shore

L'Istituto sull'Inquinamento Atmosferico (IIA) del Consiglio Nazionale delle Ricerche (CNR), nell'ambito del progetto MedOceanor, sta conducendo periodiche campagne di misure per stabilire l'impatto antropogenico sul Mar Mediterraneo. Tra i vari inquinanti di interesse per la qualità dell'aria, quali, ad esempio, il mercurio, l'ozono, ossidi di azoto, è stato monitorato anche il particolato ($PM_{2.5}$ – *fine* e $PM_{2.5-10}$ – *coarse*), il quale si insidia nell'apparato respiratorio, mettendo a repentaglio la salute dell'uomo.

I campionamenti sono stati eseguiti su filtri di Teflon a 24 h.

Le rotte delle 10 campagne di misura ivi analizzate sono indicate in **Fig. 1**, mentre i periodi di svolgimento sono riportati in **Tab. 1**.

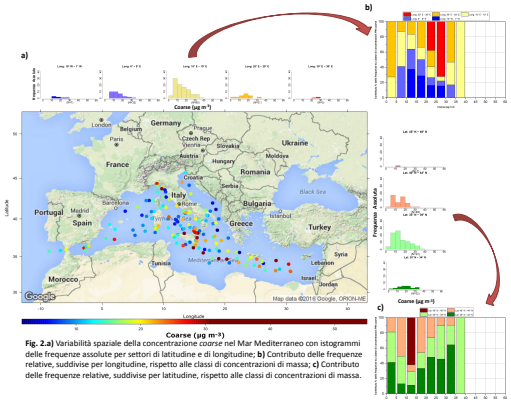

Fig. 2.a) Variabilità spaziale della concentrazione *coarse* nel Mar Mediterraneo con istogrammi delle frequenze assolute per settori di latitudine e di longitudine; **b)** Contributo delle frequenze relative, suddivise per longitudine, rispetto alle classi di concentrazioni di massa; **c)** Contributo delle frequenze relative, suddivise per latitudine, rispetto alle classi di concentrazioni di massa.

Campagna di misura	Periodo
Fenice 2003	5-28 agosto
Fenice 2004	17 marzo – 5 aprile
Fenice 2006	4-20 luglio
Fenice 2007	12 settembre – 2 ottobre
Fenice 2009	4-30 luglio
Fenice 2010	27 agosto – 12 settembre
Fenice 2011	25 ottobre – 7 novembre
Fenice 2012	11 – 28 agosto
Fenice 2013	27 luglio – 12 agosto
Fenice 2015	26 giugno – 13 luglio

Tab. 1. Campagne di misure con relativi periodi di svolgimento.

Fig. 1. Mappa delle rotte delle 10 campagne di misure.

2. Risultati - *Coarse*

La **Fig. 2.a** mostra la variabilità spaziale di tutte le misure eseguite durante le 10 campagne *off-shore*, mettendo in evidenza che nel corso di 13 anni, è stato ricoperto quasi totalmente il bacino del Mar Mediterraneo. La **Fig. 2.a**, consente inoltre di individuare, in maniera preliminare, le aree in cui si sono registrati i valori più alti del particolato *coarse*, ovvero, la zona esplorata in prossimità della Sicilia, le aree più vicine alle coste africane e qualche sito attiguo alle coste italiane (Golfo di Genova). In corrispondenza dei settori di latitudine (ogni 5°) e di longitudine (ogni 10°), sono stati riportati gli istogrammi con le frequenze assolute, mettendo in evidenza che la maggior parte delle misure sono state eseguite nella zona centrale (Lat: 35° N – 44° N, Long: 0° - 19 ° E).

La **Fig. 2.b** mostra i vari contributi delle frequenze relative nelle classi di concentrazioni di massa (ogni 5 μg m^{-3}), calcolate rispetto al singolo settore di longitudine. I valori più alti (maggiori di 30 μg m^{-3}) si addensano tra 10 ° E e 29° E.

Dalla **Fig. 2.c**, che mostra i contributi delle frequenze relative nelle classi di concentrazioni di massa, calcolate rispetto ai settori di latitudine, si deduce che le concentrazioni più elevate sono state registrate tra 30° N e 39°N.

Integrando le informazioni dedotte dalle **Fig. 2.b e Fig. 2.c**, si individuano due *hot-spots*: una regione che include la Sicilia (10° - 19° E e 35° - 39° N) e l'altra vicino l'Africa (20° - 29° E e 30° - 34° N).

3. Risultati - *Fine*

Dalla **Fig. 3.a**, si individuano le aree soggette a concentrazioni più elevate di particolato fine, e, nel caso in esame, risulta un'unica regione in prossimità della Sicilia. Analogamente al caso del particolato *coarse*, in corrispondenza dei settori di latitudine (ogni 5°) e di longitudine (ogni 10°), sono stati riportati gli istogrammi con le frequenze assolute.

La **Fig. 3.b**, che indica i vari contributi nelle classi di concentrazioni di massa (ogni 5 μg m^{-3}) delle frequenze relative, calcolate rispetto al singolo settore di longitudine, evidenzia che le concentrazioni più elevate di particolato *fine* sono state registrate tra 10 °E e 19°E.

La **Fig. 3.c**, che mostra i contributi nelle classi di concentrazioni di massa (ogni 5 μg m^{-3}) delle frequenze relative, calcolate rispetto ai settori di latitudine, nelle diverse classi di massa, indica che le più alte concentrazioni sono state riscontrate tra 35°N e 39°N.

È confermato, anche nel caso del particolato *fine*, l'*hot-spot* per la Sicilia (10° - 19°E e 35° - 39°N).

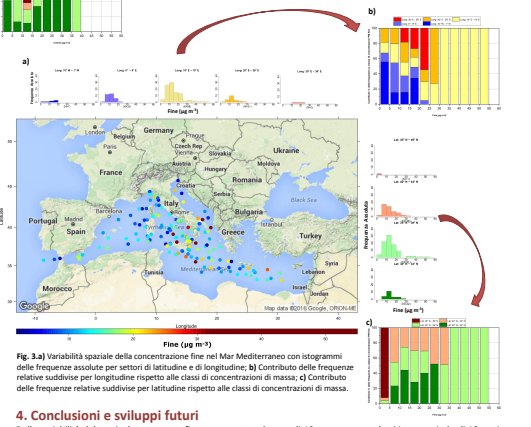

Fig. 3.a) Variabilità spaziale della concentrazione fine nel Mar Mediterraneo con istogrammi delle frequenze assolute per settori di latitudine e di longitudine; **b)** Contributo delle frequenze relative suddivise per longitudine rispetto alle classi di concentrazioni di massa; **c)** Contributo delle frequenze relative suddivise per latitudine rispetto alle classi di concentrazioni di massa.

HOT SPOTS

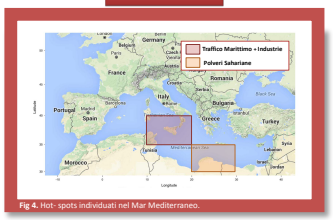

Fig 4. Hot- spots individuati nel Mar Mediterraneo.

4. Conclusioni e sviluppi futuri

Dalla variabilità del particolato *coarse* e *fine* e osservata nel corso di 10 campagne, svoltesi in un periodo di 13 anni, sono state individuate due *hot-spots* (**Fig. 4**): il primo, sia per *coarse* che per *fine*, nell'area circostante la Sicilia, probabilmente, per via del consistente traffico marino e per le attività portuali, nonché per la presenza di un elevato numero di industrie; il secondo, relativo solo a concentrazioni *coarse*, è stato individuato in prossimità delle coste africane, dove il contributo delle polveri Sahariane è significativo.

Ulteriori campagne di misure, soprattutto agli estremi del bacino, forniranno un maggior numero di dati osservativi; inoltre la caratterizzazione chimica dei vari campioni, potrà consentire in futuro di individuare con maggiore confidenza le sorgenti del particolato che insistono nel Mar Mediterraneo.

References

1. **Bencardino, M., Sprovieri, F.** Cofone, F., and **Pirrone, N.** (2011) Variability of Atmospheric Aerosol and Ozone Concentrations at Marine, Urban, and High-Altitude Monitoring Stations in Southern Italy during the 2007 Summer Saharan Dust Outbreaks and Wildfire Episodes. Journal of the Air & Waste Management Association, 61, 952-967.
2. **Bencardino, M., Pirrone, N., Sprovieri, F.** (2014) Aerosol and ozone observations during six cruise campaigns across the Mediterranean basin: temporal, spatial, and seasonal variability. Environmental Science and Pollution Research, 21, Issue 6, 4044-4062.
3. **Castagna, J., Carbone, F., Naccarato, A., Moretti, S., Esposito, G., Bencardino, M., D'Amore, F., Sprovieri, F., Pirrone N. (2016)** Variability of fine and coarse aerosol over the Western Mediterranean Basin during the Minerva 2015 research cruise campaign. Geophysical Research Abstracts, 18, EGU2016-4022-2.

VII Convegno Nazionale sul Particolato Atmosferico • Roma 17-20 maggio

Particulate Matter over the Western Mediterranean sea: new insights gained from data collected during the 2011, 2012 and 2015 CNR research cruise campaigns

Jessica Castagna (1), Francesco D'Amore (1), Attilio Naccarato (1), Sacha Moretti (1), Valentino Mannarino (1), Mariantonia Bencardino (1), Francesca Sprovieri (1), and Nicola Pirrone (2)
(1) CNR-Institute of Atmospheric Pollution Research, Division of Rende, Italy (j.castagna@iia.cnr.it), (2) CNR-Institute of Atmospheric Pollution Research, Montelibretti, Rome, Italy (pirrone@iia.cnr.it)
The Mediterranean basin, due to its unique geographic position and its peculiar meteo-climatic conditions, appears to be an area with a relevant pollution load. Significant is the contribution of dense ship traffic and highly industrialized population centres surrounding the basin itself but a large influence is also due to geological sources like Saharan dust and volcanic ashes. The transport of both natural dust and anthropogenic aerosols into the marine environment involves considerable interest, not least for its potential impact on marine ecosystems, world climate and air quality. However, whereas there is already a large monitoring database measuring air pollution at surface land-based sites and in ports, there is a relatively little information on atmospheric aerosol directly measured at sea. In order to fill in the gap of observations in the Mediterranean basin and to gain more insight into the atmospheric dynamical and chemical mechanisms leading to high surface Particulate Matter (PM) levels, the Institute of Atmospheric Pollution of the National Research Council (CNR-IIA), since 2003, has started regular ship-borne measurements over the Mediterranean Sea. In the present work we will specifically focus on PM observations obtained, travelling on the sea, during three cruise campaigns performed during autumn 2011, summer 2012 and summer 2015, along different tracks and almost covering the Western Mediterranean sector. We specifically recorded two, gravimetrically determined, PM size fraction mass concentrations (PM2.5 and PM10), whose major and trace elemental

composition was subsequently obtained by chemical analysis with an Inductively Coupled Plasma Mass Spectrometer (ICP-MS). Overall, we obtained 40 days of data observations whose analysis contributes to investigate the causes of aerosol pollution in this area. Data on PM mass concentrations showed a quite high variability ranging from 10.5 to 38.8 $\mu g.m^{-3}$ for the PM10, and from 5.5 to 29.7 $\mu g.m^{-3}$ for the PM2.5 size fraction, respectively. Meteorological conditions, at both local and synoptic scales, were jointly investigated with PM levels to highlight seasonal influence and to identify potential long-range transport events. Data on elemental composition were also used as input data for a Principal Component Analysis (PCA), whose results gave us some qualitative understanding on the sources with major impact on the investigated Mediterranean sector.

PARTICULATE MATTER OVER THE WESTERN MEDITERRANEAN SEA: NEW INSIGHTS GAINED FROM DATA COLLECTED DURING THE 2011, 2012, AND 2015 CNR RESEARCH CRUISE CAMPAIGN

Jessica Castagna1*, Francesco D'Amore1, Attilio Naccarato1, Sacha Moretti1, Valentino Mannarino1, Mariantonia Bencardino1, Francesca Sprovieri1, and Nicola Pirrone2
1CNR-Institute of Atmospheric Pollution Research, Division of Rende, Italy, 2CNR-Institute of Atmospheric Pollution Research, Montelibretti, Rome, Italy,
*Corresponding Author: jessica.castagna@iia.cnr.it

1. Research Cruise Campaigns

The Mediterranean sea is a particular area of interest for the pollution load because it is affected by geological sources, like as active volcanoes or the Sahara Desert, and, furthermore, by the massive anthropogenic emissions, due to activities of the population living in the surrounding territory, like as the industries. The airborne pollution on the sea is becoming always more troubling because it implies a negative impact on the marine ecosystems, world climate, and air quality. Since 2003, the Institute for Atmospheric Pollution of the Italian National Research Council (CNR) is conducting periodic cruise campaigns covering the whole basin, during which, the aerosol was monitored (PM2.5 and PM10).

Fig. 1 Oceanographic campaign routes in Western Mediterranean Basin.

In this work, we focused on the last 3 cruise campaigns conducted just on the Western sector onboard a Research Vessel:

a) Fenice 2011: 27/10 - 07/11;
b) Fenice 2012: 12/08 - 28/08;
c) Minerva Uno 2015: 26/06 - 13/07;

The cruise campaigns' routes were reported in Fig. 1.

2. PM and Meteorological Measurements

The PM sampling instrument used during the Fenice 2011 was the Dichotomous, while for both, Fenice 2012 and Minerva Uno 2015, the sampling instrument was the Skypost PM FG - Tecora. While the first instrument has sampled directly fine (PM2.5) and coarse (PM2.5-10) particulate, the other has sampled PM2.5 and PM10. With both instruments, the sampling was carried out on 47ømm Teflon filters, which were conditioned and weighted before and after sampling, therefore the particulate concentration was calculated gravimetrically. Meteorological measurements (Temperature and Wind Speed) were monitored by the

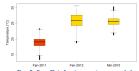

Fig. 2 Box Plot for temperature recorded during the three cruise campaigns.

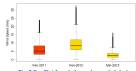

Fig. 3 Box Plot for wind speed recorded during the three cruise campaigns.

The lowest and highest temperature were recorded respectively during the autumn 2011 and the summer 2012 (Fig. 2), instead the cruise with the strongest wind was the Fenice 2012 (Fig. 3).
In this analysis, we considered PM2.5 and PM10, therefore, for Fenice 2011, we calculated PM10 like the sum of PM2.5 and PM2.5-10.

3. PM Spatial Distribution

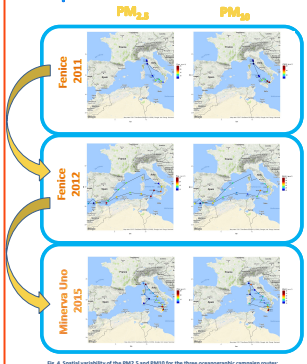

Fig. 4 Spatial variability of the PM2.5 and PM10 for the three oceanographic campaign routes: Fenice 2011, Fenice 2012 and Minerva Uno 2015.

The high values of both PM2.5 and PM10 were recorded in the southern area of Western Mediterannean sea, close to the African coasts, and in the proximity of Tuscany, where there are many industries (Fig. 4).

4. PCA Results

To identify the principal sources of aerosol sampled on the Western Mediterranean Sea, a receptor modeling, the Principal Component Analysis (PCA), has been applied to the PM10 measurements, including elements. The major and trace elements concentrations were determined by ICP-MS, after the Teflon filter digestion with a mixture of HNO3/H2O2 in a microwaves digestion system. According to the Keiser criterion, which establishes the selection of just the components characterized by the eigenvalues >1, we identified 4 Principal Components (Tab. 1). We identified and tagged some individuals with a significant contribution (Fig. 5).

	PCA1: Natural Sources	PCA2: Marine Spray + Traffic	PCA3: Volcanic ashes	PCA4: Industries + Shipping Traffic
PM10	0.74	0.26	0.06	0.24
Mg	0.92	0.00	0.01	0.07
Mg	0.90	0.47	0.23	0.14
Al	0.93	0.00	0.02	0.03
K	0.92	0.00	0.06	0.02
Ca	0.58	0.06	0.08	0.11
V	0.18	0.75	0.09	0.13
Mn	0.93	0.03	0.23	0.03
Fe	0.93	0.04	0.24	0.00
Co	0.53	0.65	0.02	0.32
Cu	0.51	0.74	0.12	0.10
Zn	0.46	0.74	0.31	0.00
Sr	0.91	0.24	0.02	0.08
Sb	0.58	0.39	0.61	0.16
Ba	0.90	0.04	0.12	0.06
Pb	0.54	0.58	0.36	0.53
%Var	50.7	20.1	7.70	6.90

Tab. 1 Results of PCA analysis.

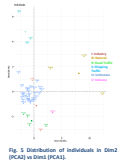

Fig. 5 Distribution of individuals in Dim2 (PCA2) vs Dim1 (PCA1).

Thanks to the Fig. 6, showing the contribution of the Principal Components for each individual, we identified some particular events:
Natural Sources (Saharan Dust) for 11s9 and 11s10; Marine Spray + Traffic (mainly shipping traffic for this individuals) for 12s3, 12s4, 12s7, and 15s5; Volcanic Ashes for 15s13; Industries + Shipping traffic for 12s7 and 15s5. The intrusions of Saharan Dust have been confirmed by NAAPS maps, on the other hand, the shipping traffic events have been confirmed by the typical V/Ni ratio (2.5 < V/Ni < 3.5).

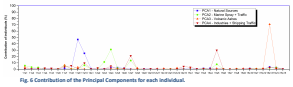

Fig. 6 Contribution of the Principal Components for each individual.

5. Conclusions

In this work, we investigated the Western Mediterranean sea by the aerosol measurements collected during three cruise campaigns (Fenice 2011, Fenice 2012, and Minerva Uno 2015). The PM2.5 and PM10 were determined gravimetrically, while the major and trace elements were determined by ICP-MS. The PM10 concentrations (total and elements concentrations) were analyzed by a model receptor, the PCA, and some events, natural and anthropogenic, were identified.

Bibliography

Hybrid single particle lagrangian integrated trajectory model, 2016. http://www.arl.noaa.gov/ready/hysplit4.html.

U.s. epa. exposure factors handbook (1997, final report). u.s. environmental protection agency, washington, dc. EPA/600/P-95/002F a-c, 1997.

E-prtr-european pollutant release and transfer register, 2016. http://prtr.ec.europa.eu/.

Firms-fire information for resource management system, 2016. http://maps.geog.umd.edu/firms.

Ncep-national centre for environmental prediction, 2016. http://www.cdc.noaa.gov/.

Nrl-naval research laboratory monterey aerosol page, 2016. http://www.nrlmry.navy.mil/aerosol.

Gmos standard operational procedure. method for the determination of total mercury in precipitation, a.

Gmos standard operational procedure. methods for the determination of speciated ambient hg, b.

Gmos standard operational procedure. methods for the determination of tgm and gem, c.

Unep gobal mercury assessment (gms) report. united nations environment programme, geneva, switzerland, 2002, a.

Unep: Excess mercury supply in latin america and the caribbean, 2010-2050. assessment report. http://www.unep.org/chemicalsandwaste/Portals/9/Mercury/Documents/%20Mercury%20Storage%20Assessment_Final_1July09.pdf, 2009, b.

Unep: Global mercury assessment 2013: Sources, emissions, releases and environmental transport. unep chemicals branch, geneva, switzerland. http://www.unep.org/PDF/PressReleases/GlobalMercuryAssessment2013.pdf, 2013, c.

AMAP/UNEP. Global mercury modelling: Update of modelling results in the global mercury assessment 2013. 2015.

Maria E Andersson, Katarina Gårdfeldt, Ingvar Wängberg, Francesca Sprovieri, Nicola Pirrone, and Oliver Lindqvist. Seasonal and daily variation of mercury evasion at coastal and off shore sites from the mediterranean sea. *Marine Chemistry*, 104(3):214–226, 2007.

Hélène Angot, Iris Dion, Nicolas Vogel, Michel Legrand, Olivier Magand, and Aurélien Dommergue. Multi-year record of atmospheric mercury at dumont d'urville, east antarctic coast: continental outflow and oceanic influences. *Atmospheric Chemistry and Physics*, 16 (13):8265–8279, 2016.

Parisa A Ariya, Alexei Khalizov, and Alexios Gidas. Reactions of gaseous mercury with atomic and molecular halogens: kinetics, product studies, and atmospheric implications. *The Journal of Physical Chemistry A*, 106(32):7310–7320, 2002.

Parisa A Ariya, Marc Amyot, Ashu Dastoor, Daniel Deeds, Aryeh Feinberg, Gregor Kos, Alexandre Poulain, Andrei Ryjkov, Kirill Semeniuk, M Subir, et al. Mercury physicochemical and biogeochemical

transformation in the atmosphere and at atmospheric interfaces: A review and future directions. *Chemical reviews*, 115(10):3760–3802, 2015.

ark L. Olson and Mark F. Rhodes. Nadp amnet standard operating procedures for field analysis of gaseous and fine particulate-bound mercury.

María Arribére, María C Diéguez, Sergio Ribeiro Guevara, Claudia P Queimalinos, Vesna Fajon, Mariana Reissig, and Milena Horvat. Mercury in an ultraoligotrophic north patagonian andean lake (argentina): concentration patterns in different components of the water column. *Journal of Environmental Sciences*, 22(8):1171–1178, 2010.

E Bagnato, A Aiuppa, F Parello, S Calabrese, W D'Alessandro, TA Mather, AJS McGonigle, DM Pyle, and I Wängberg. Degassing of gaseous (elemental and reactive) and particulate mercury from mount etna volcano (southern italy). *Atmospheric Environment*, 41 (35):7377–7388, 2007.

E Bagnato, A Aiuppa, F Parello, P Allard, H Shinohara, M Liuzzo, and G Giudice. New clues on the contribution of earth's volcanism to the global mercury cycle. *Bulletin of Volcanology*, 73(5):497–510, 2011.

Nikolai B Balabanov and Kirk A Peterson. Mercury and reactive halogens: the thermochemistry of hg+{Cl2, Br2, BrCl, ClO, and BrO}. *The Journal of Physical Chemistry A*, 107(38):7465–7470, 2003.

Mariantonia Bencardino, Francesca Sprovieri, and Nicola Pirrone. Large industrial point sources in italy: a focus on mercury concentrations resulting from three seasonal ship-borne measurements. In *E3S Web of Conferences*, 2013. doi: 10.1051/e3sconf/20130123005.

Mariantonia M Bencardino, Nicola N Pirrone, and Francesca F

Sprovieri. Aerosol and ozone observations during six cruise campaigns across the mediterranean basin: temporal, spatial, and seasonal variability. *Environmental Science and Pollution Research*, 21 (6):4044–4062, 2014.

Heinz-Jürgen Benkelberg, Olaf Böge, Ralph Seuwen, and Peter Warneck. Product distributions from the oh radical-induced oxidation of but-1-ene, methyl-substituted but-1-enes and isoprene in no x-free air. *Physical Chemistry Chemical Physics*, 2(18):4029–4039, 2000.

Emilio Bianchi, Ricardo Villalba, Maximiliano Viale, Fleur Couvreux, and Rocio Marticorena. New precipitation and temperature grids for northern patagonia: Advances in relation to global climate grids. *Journal of Meteorological Research*, 30(1):38–52, 2016.

Richard JC Brown, N Pirrone, C Van Hoek, F Sprovieri, R Fernandez, and K Toté. Standardisation of a european measurement method for the determination of total gaseous mercury: results of the field trial campaign and determination of a measurement uncertainty and working range. *Journal of Environmental Monitoring*, 12(3):689–695, 2010.

Débora Bubach, Soledad Pérez Catán, María Arribére, and Sergio Ribeiro Guevara. Bioindication of volatile elements emission by the puyehue–cordón caulle (north patagonia) volcanic event in 2011. *Chemosphere*, 88(5):584–590, 2012.

F Carbone, MS Landis, CN Gencarelli, A Naccarato, F Sprovieri, F De Simone, IM Hedgecock, and N Pirrone. Sea surface temperature variation linked to elemental mercury concentrations measured on mauna loa. *Geophysical Research Letters*, 43(14):7751–7757, 2016.

Jinfeng Chen, Juan Tang, Jun Zhou, Lan Zhang, Guonan Chen, and Dianping Tang. Target-induced formation of gold amalgamation on

dna-based sensing platform for electrochemical monitoring of mercury ion coupling with cycling signal amplification strategy. *Analytica chimica acta*, 810:10–16, 2014.

Irene Cheng, Leiming Zhang, Huiting Mao, Pierrette Blanchard, Rob Tordon, and John Dalziel. Seasonal and diurnal patterns of speciated atmospheric mercury at a coastal-rural and a coastal-urban site. *Atmospheric environment*, 82:193–205, 2014.

Jesper Heile Christensen. The danish eulerian hemispheric model a three-dimensional air pollution model used for the arctic. *Atmospheric Environment*, 31(24):4169–4191, 1997.

S Cinnirella, F D'Amore, M Bencardino, F Sprovieri, and N Pirrone. The gmos cyber (e)-infrastructure: advanced services for supporting science and policy. *Environmental Science and Pollution Research*, 21(6):4193–4208, 2014.

Colin A Cooke, Prentiss H Balcom, Harald Biester, and Alexander P Wolfe. Over three millennia of mercury pollution in the peruvian andes. *Proceedings of the National Academy of Sciences*, 106(22): 8830–8834, 2009.

Michael P Crockett, Austin M Evans, Max JH Worthington, Inês S Albuquerque, Ashley D Slattery, Christopher T Gibson, Jonathan A Campbell, David A Lewis, Gonçalo JL Bernardes, and Justin M Chalker. Sulfur-limonene polysulfide: A material synthesized entirely from industrial by-products and its use in removing toxic metals from water and soil. *Angewandte Chemie International Edition*, 55(5):1714–1718, 2016.

Romina Daga, Sergio Ribeiro Guevara, M Lidia Sánchez, and María Arribére. Tephrochronology of recent events in the andean range (northern patagonia): spatial distribution and provenance of lacustrine ash layers in the nahuel huapi national park. *Journal of Quaternary Science*, 25(7):1113–1123, 2010.

Romina Daga, Sergio Ribeiro Guevara, Daniel G Poire, and María Arribére. Characterization of tephras dispersed by the recent eruptions of volcanoes calbuco (1961), chaitén (2008) and cordón caulle complex (1960 and 2011), in northern patagonia. *Journal of South American Earth Sciences*, 49:1–14, 2014.

Romina Daga, Sergio Ribeiro Guevara, and María Arribére. New records of late holocene tephras from lake futalaufquen (42.8Â° s), northern patagonia. *Journal of South American Earth Sciences*, 66: 232–247, 2016a.

Romina Daga, Sergio Ribeiro Guevara, Majda Pavlin, Andrea Rizzo, Sonja Lojen, Polona Vreča, Milena Horvat, and María Arribére. Historical records of mercury in southern latitudes over 1600years: Lake futalaufquen, northern patagonia. *Science of the Total Environment*, 553:541–550, 2016b.

Francesco D'Amore, Mariantonia Bencardino, Sergio Cinnirella, Francesca Sprovieri, and Nicola Pirrone. Data quality through a web-based qa/qc system: implementation for atmospheric mercury data from the global mercury observation system. *Environmental Science: Processes & Impacts*, 17(8):1482–1491, 2015.

Francesco De Simone, Sergio Cinnirella, Christian N Gencarelli, Francesco Carbone, Ian M Hedgecock, and Nicola Pirrone. Particulate-phase mercury emissions during biomass burning and impact on resulting deposition: a modelling assessment. *Atmos. Chem. Phys. Discuss., http://dx. doi. org/10.5194/acp-2016-685, in review*, 2016.

Ministero dell'Ambiente ITALIA. Aia rosignano. Technical report, Ministero dell'Ambiente - ITALIA, 2010.

Stefania Di Vito, Andrea Minutolo, and Giorgio Zampetti. Mal'aria di cittÃ 2016. l'inquinamento atmosferico e acustico nelle cittÃ italiane). Technical report, Legambiente, 2016. URL http://www.legambiente.it/sites/default/files/docs/malaria2016.pdf.

Russell R Dickerson, Kevin P Rhoads, Thomas P Carsey, Samuel J Oltmans, John P Burrows, and Paul J Crutzen. Ozone in the remote marine boundary layer: A possible role for halogens. *Journal of Geophysical Research*, 104(21):385–21, 1999.

M. C. Diéguez, P. E. Garcia, M. Bencardino, F. D'Amore, J. Castagna, S. Ribeiro Guevara, and F. Sprovieri. Four years of atmospheric mercury records in northwestern patagonia (argentina): potential sources, concentration patterns and influence of environmental variables observed at the gmos emma station. *Atmospheric Chemistry and Physics Discussions*, 2017:1–18, 2017. doi: 10.5194/acp-2016-1076. URL http://www.atmos-chem-phys-discuss.net/acp-2016-1076/.

R Draxler and GD Rolph. Hysplit (hybrid single-particle lagrangian integrated trajectory) model access via noaa arl ready website. noaa air resources laboratory, silver spring. http://www. arl. noaa. gov/ready/hysplit4. html, 2003.

Charles T Driscoll, Robert P Mason, Hing Man Chan, Daniel J Jacob, and Nicola Pirrone. Mercury as a global pollutant: sources, pathways, and effects. *Environmental science & technology*, 47(10): 4967–4983, 2013.

Mark A Engle, Michael T Tate, David P Krabbenhoft, Allan Kolker, Mark L Olson, Eric S Edgerton, John F DeWild, and Ann K McPherson. Characterization and cycling of atmospheric mercury along the central us gulf coast. *Applied Geochemistry*, 23(3):419–437, 2008.

U EPA. Method 1631, revision e: Mercury in water by oxidation, purge and trap, and cold vapor atomic fluorescence spectrometry. *US Environmental Protection Agency Washington, DC*, 2002.

Buck D.G. Dalton A.K. Johnson S.M Evers, D.C. Understanding spatial patterns for biomonitoring needs of the minamata convention on

mercury. In *BRI Science Communications Series 2016-02*, page 20, 2016.

L Fantozzi, G Manca, I Ammoscato, N Pirrone, and F Sprovieri. The cycling and sea–air exchange of mercury in the waters of the eastern mediterranean during the 2010 med-oceanor cruise campaign. *Science of the total environment*, 448:151–162, 2013.

Khalil Farhadi, Mehrdad Forough, Rahim Molaei, Salahaddin Hajizadeh, and Aysan Rafipour. Highly selective hg 2+ colorimetric sensor using green synthesized and unmodified silver nanoparticles. *Sensors and Actuators B: Chemical*, 161(1):880–885, 2012.

DM Feddersen, R Talbot, H Mao, and BC Sive. Size distribution of particulate mercury in marine and coastal atmospheres. *Atmospheric Chemistry and Physics*, 12(22):10899–10909, 2012.

Jack Erric Fergusson. *Heavy elements: chemistry, environmental impact and health effects*. Pergamon, 1990.

R Ferrara, B Mazzolai, E Lanzillotta, E Nucaro, and N Pirrone. Temporal trends in gaseous mercury evasion from the mediterranean seawaters. *Science of the Total Environment*, 259(1):183–190, 2000.

Barbara J Finlayson-Pitts. Atmospheric chemistry. *Proceedings of the National Academy of Sciences*, 107(15):6566–6567, 2010.

HR Friedli, LF Radke, JY Lu, CM Banic, WR Leaitch, and JI MacPherson. Mercury emissions from burning of biomass from temperate north american forests: laboratory and airborne measurements. *Atmospheric Environment*, 37(2):253–267, 2003a.

HR Friedli, LF Radke, R Prescott, PV Hobbs, and P Sinha. Mercury emissions from the august 2001 wildfires in washington state and an agricultural waste fire in oregon and atmospheric mercury budget estimates. *Global Biogeochemical Cycles*, 17(2), 2003b.

René Garreaud, P Lopez, M Minvielle, and M Rojas. Large-scale control on the patagonian climate. *Journal of Climate*, 26(1):215–230, 2013.

David A Gay, David Schmeltz, Eric Prestbo, Mark Olson, Timothy Sharac, and Robert Tordon. The atmospheric mercury network: measurement and initial examination of an ongoing atmospheric mercury record across north america. *Atmospheric Chemistry and Physics*, 13(22):11339–11349, 2013.

Christian N Gencarelli, Ian M Hedgecock, Francesca Sprovieri, Gregor J Schürmann, and Nicola Pirrone. Importance of ship emissions to local summertime ozone production in the mediterranean marine boundary layer: A modeling study. *Atmosphere*, 5(4):937–958, 2014.

Christian N Gencarelli, Francesco De Simone, Ian M Hedgecock, Francesca Sprovieri, Xin Yang, and Nicola Pirrone. European and mediterranean mercury modelling: Local and long-range contributions to the deposition flux. *Atmospheric Environment*, 117:162–168, 2015.

Christian N Gencarelli, Johannes Bieser, Francesco Carbone, Francesco De Simone, Ian M Hedgecock, Matthias Volker, Oleg Travnikov, Xin Yang, and Nicola Pirrone. Sensitivity model study of regional mercury dispersion in the atmosphere. *Atmospheric Chemistry and Physics*, 17(1):627, 2017.

Darija Gibičar, Milena Horvat, Martina Logar, Vesna Fajon, Ingrid Falnoga, Romano Ferrara, Enrica Lanzillotta, Claudia Ceccarini, Barbara Mazzolai, Bruce Denby, et al. Human exposure to mercury in the vicinity of chlor-alkali plant. *Environmental research*, 109(4): 355–367, 2009.

Michael Evan Goodsite, JMC Plane, and H Skov. A theoretical study of the oxidation of hg0 to hgbr2 in the troposphere. *Environmental science & technology*, 38(6):1772–1776, 2004.

S Ribeiro Guevara, D Bubach, and M Arribére. Mercury in lichens of nahuel huapi national park, patagonia, argentina. *Journal of Radioanalytical and Nuclear Chemistry*, 261(3):679–687, 2004a.

S Ribeiro Guevara, D Bubach, P Vigliano, G Lippolt, and MA Arribére. Heavy metal and other trace elements in native mussel diplodon chilensis from nothern patagonia lakes, argentina. *Biological Trace Element Research*, 102(1-3):245–263, 2004b.

Mae Sexauer Gustin. Are mercury emissions from geologic sources significant? a status report. *Science of the Total Environment*, 304 (1):153–167, 2003.

Mae Sexauer Gustin, Steven E Lindberg, and Peter J Weisberg. An update on the natural sources and sinks of atmospheric mercury. *Applied Geochemistry*, 23(3):482–493, 2008.

Mae Sexauer Gustin, David C Evers, Michael S Bank, Chad R Hammerschmidt, Ashley Pierce, Niladri Basu, Joel Blum, Paco Bustamante, Celia Chen, Charlie T Driscoll, et al. Importance of integration and implementation of emerging and future mercury research into the minamata convention. *Environmental science & technology*, 50(6):2767–2770, 2016.

Barbara Gworek, Olga Bemowska-Kałabun, Marta Kijeńska, and Justyna Wrzosek-Jakubowska. Mercury in marine and oceanic waters-a review. *Water, Air, & Soil Pollution*, 227(10):371, 2016.

Björn Hall, Peter Schager, and Evert Ljungström. An experimental study on the rate of reaction between mercury vapour and gaseous nitrogen dioxide. *Water, Air, & Soil Pollution*, 81(1):121–134, 1995.

Reed C Harris, John WM Rudd, Marc Amyot, Christopher L Babiarz, Ken G Beaty, Paul J Blanchfield, RA Bodaly, Brian A Branfireun, Cynthia C Gilmour, Jennifer A Graydon, et al. Whole-ecosystem study shows rapid fish-mercury response to changes in mercury deposition. *Proceedings of the National Academy of Sciences*, 104(42): 16586–16591, 2007.

Ian M Hedgecock and Nicola Pirrone. Mercury and photochemistry in the marine boundary layer-modelling studies suggest the in situ production of reactive gas phase mercury. *Atmospheric Environment*, 35(17):3055–3062, 2001.

Ian M Hedgecock, Nicola Pirrone, Francesca Sprovieri, and Eduardo Pesenti. Reactive gaseous mercury in the marine boundary layer: modelling and experimental evidence of its formation in the mediterranean region. *Atmospheric Environment*, 37:41–49, 2003.

Ian M Hedgecock, Giuseppe A Trunfio, Nicola Pirrone, and Francesca Sprovieri. Mercury chemistry in the mbl: Mediterranean case and sensitivity studies using the amcots (atmospheric mercury chemistry over the sea) model. *Atmospheric Environment*, 39(38):7217–7230, 2005.

Ian M Hedgecock, Nicola Pirrone, Giuseppe A Trunfio, and Francesca Sprovieri. Integrated mercury cycling, transport, and air-water exchange (mecawex) model. *Journal of Geophysical Research: Atmospheres*, 111(D20), 2006.

Y-M Hermanns and H Biester. A 17,300-year record of mercury accumulation in a pristine lake in southern chile. *Journal of paleolimnology*, 49(4):547–561, 2013a.

Yvonne-Marie Hermanns and Harald Biester. Anthropogenic mercury signals in lake sediments from southernmost patagonia, chile. *Science of the Total Environment*, 445:126–135, 2013b.

Pablo Higueras, Roberto Oyarzun, Joze Kotnik, José María Esbrí, Alba Martínez-Coronado, Milena Horvat, Miguel Angel López-Berdonces, Willians Llanos, Orlando Vaselli, Barbara Nisi, et al. A compilation of field surveys on gaseous elemental mercury (gem) from contrasting environmental settings in europe, south america, south africa and china: separating fads from facts. *Environmental geochemistry and health*, 36(4):713–734, 2014.

Christopher D Holmes, Daniel James Jacob, Elizabeth Sturges Corbitt, Jingqiu Mao, Xin Yang, Robert Talbot, and Franz Slemr. Global atmospheric model for mercury including oxidation by bromine atoms. *Atmospheric Chemistry and Physics*, 10(24):12037–12057, 2010.

Anthony J Hynes, Deanna L Donohoue, Michael E Goodsite, and Ian M Hedgecock. Our current understanding of major chemical and physical processes affecting mercury dynamics in the atmosphere and at the air-water/terrestrial interfaces. In *Mercury fate and transport in the global atmosphere*, pages 427–457. Springer, 2009.

Åke Iverfeldt. Mercury in forest canopy throughfall water and its relation to atmospheric deposition. *Water, Air, & Soil Pollution*, 56 (1):553–564, 1991.

Purim Jarujamrus, Maliwan Amatatongchai, Araya Thima, Thatsanee Khongrangdee, and Chakrit Mongkontong. Selective colorimetric sensors based on the monitoring of an unmodified silver nanoparticles (agnps) reduction for a simple and rapid determination of mercury. *Spectrochimica Acta Part A: Molecular and Biomolecular Spectroscopy*, 142:86–93, 2015.

IR Jonasson et al. Mercury in the natural environment: a review of recent work. *Mercury in the natural environment: a review of recent work.*, (70-57), 1970.

CC Jorn, Edward PC Lai, and Susan Sadeghi. Surface plasmon resonance sensor for hg (ii) detection by binding interactions with polypyrrole and 2-mercaptobenzothiazole. *Sensors and Actuators B: Chemical*, 101(1):236–241, 2004.

Hadi Khani, Mohammad Kazem Rofouei, Pezhman Arab, Vinod Kumar Gupta, and Zahra Vafaei. Multi-walled carbon nanotubes-ionic liquid-carbon paste electrode as a super selectivity sensor: application to potentiometric monitoring of mercury ion (ii). *Journal of hazardous materials*, 183(1):402–409, 2010.

Pyung-Rae Kim, Young-Ji Han, Thomas M Holsen, and Seung-Muk Yi. Atmospheric particulate mercury: Concentrations and size distributions. *Atmospheric environment*, 61:94–102, 2012.

Rong-Mei Kong, Xiao-Bing Zhang, Liang-Liang Zhang, Xiao-Yong Jin, Shuang-Yan Huan, Guo-Li Shen, and Ru-Qin Yu. An ultrasensitive electrochemical "turn-on" label-free biosensor for hg2+ with aunp-functionalized reporter dna as a signal amplifier. *Chemical Communications*, (37):5633–5635, 2009.

J Kotnik, M Horvat, N Ogrinc, V Fajon, D Žagar, D Cossa, F Sprovieri, and N Pirrone. Mercury and its species in the adriatic sea. *Mar Chem (in review)*, 2013.

Jože Kotnik, Milena Horvat, Nives Ogrinc, Vesna Fajon, Dušan Žagar, Daniel Cossa, Francesca Sprovieri, and Nicola Pirrone. Mercury speciation in the adriatic sea. *Marine pollution bulletin*, 96(1):136–148, 2015.

Sae Yun Kwon and Noelle E Selin. Uncertainties in atmospheric mercury modeling for policy evaluation. *Current Pollution Reports*, 2 (2):103–114, 2016.

Matthew S Landis, Robert K Stevens, Frank Schaedlich, and Eric M Prestbo. Development and characterization of an annular denuder methodology for the measurement of divalent inorganic reactive gaseous mercury in ambient air. *Environmental science & technology*, 36(13):3000–3009, 2002.

Fabien Laurier and Robert Mason. Mercury concentration and speciation in the coastal and open ocean boundary layer. *Journal of Geophysical Research: Atmospheres*, 112(D6), 2007.

Fabien JG Laurier, Robert P Mason, Lindsay Whalin, and Shungo Kato. Reactive gaseous mercury formation in the north pacific ocean's marine boundary layer: A potential role of halogen chemistry. *Journal of Geophysical Research: Atmospheres*, 108(D17), 2003.

Che-jen Lin and Simo O Pehkonen. Aqueous free radical chemistry of mercury in the presence of iron oxides and ambient aerosol. *Atmospheric Environment*, 31(24):4125–4137, 1997.

Che-Jen Lin and Simo O Pehkonen. Aqueous phase reactions of mercury with free radicals and chlorine: implications for atmospheric mercury chemistry. *Chemosphere*, 38(6):1253–1263, 1999.

Steve Lindberg, Russell Bullock, Ralf Ebinghaus, Daniel Engstrom, Xinbin Feng, William Fitzgerald, Nicola Pirrone, Eric Prestbo, and Christian Seigneur. A synthesis of progress and uncertainties in attributing the sources of mercury in deposition. *AMBIO: a Journal of the Human Environment*, 36(1):19–33, 2007.

Xueping Liu, Chenhu Sun, Huiwang Wu, Yifang Zhang, Jianhui Jiang, Guoli Shen, and Ruqin Yu. Label-free electrochemical biosensor of mercury ions based on dna strand displacement by thymine–hg (ii)–thymine complex. *Electroanalysis*, 22(17-18):2110–2116, 2010.

Elizabeth G Malcolm, Gerald J Keeler, and Matthew S Landis. The effects of the coastal environment on the atmospheric mercury cycle. *Journal of Geophysical Research: Atmospheres*, 108(D12), 2003.

J Maly, C Di Meo, M De Francesco, A Masci, J Masojidek, M Sugiura, A Volpe, and R Pilloton. Reversible immobilization of engineered molecules by ni-nta chelators. *Bioelectrochemistry*, 63(1):271–275, 2004.

J Maly, M Ilie, V Foglietti, E Cianci, A Minotti, L Nardi, A Masci, W Vastarella, and R Pilloton. Continuous flow micro-cell for electrochemical addressing of engineered bio-molecules. *Sensors and Actuators B: Chemical*, 111:317–322, 2005.

Yaacov Mamane, Cinzia Perrino, Osnat Yossef, and Maria Catrambone. Source characterization of fine and coarse particles at the east mediterranean coast. *Atmospheric Environment*, 42(24):6114–6130, 2008.

Gómez Martín. Enhanced production of oxidised mercury over the tropical pacific ocean: a key missing oxidation pathway. *Atmos. Chem. Phys*, 1680:7324, 2014.

Robert P Mason. Mercury emissions from natural processes and their importance in the global mercury cycle. In *Mercury fate and transport in the global atmosphere*, pages 173–191. Springer, 2009.

Robert P Mason and G-R Sheu. Role of the ocean in the global mercury cycle. *Global biogeochemical cycles*, 16(4), 2002.

Robert P Mason, William F Fitzgerald, and Francois MM Morel. The biogeochemical cycling of elemental mercury: anthropogenic influences. *Geochimica et Cosmochimica Acta*, 58(15):3191–3198, 1994.

Robert P Mason, Michael L Abbott, RA Bodaly, O Russell Bullock, Jr Jr, Charles T Driscoll, David Evers, Steven E Lindberg, Michael Murray, and Edward B Swain. Monitoring the response to changing mercury deposition, 2005.

Michelle G Nerentorp Mastromonaco, Katarina Gårdfeldt, and Ingvar Wängberg. Seasonal and spatial evasion of mercury from the western mediterranean sea. *Marine Chemistry*, 2017.

M Mermoz, C Úbeda, D Grigera, C Brion, C Martín, E Bianchi, and H Planas. El parque nacional nahuel huapi: sus características ecológicas y estado de conservación. *Administración de Parques Nacionales, Parque Nacional Nahuel Huapi, San Carlos de Bariloche, Argentina*, 2009.

Yoko Miyake, Humika Togashi, Mitsuru Tashiro, Hiroshi Yamaguchi, Shuji Oda, Megumi Kudo, Yoshiyuki Tanaka, Yoshinori Kondo, Ryuichi Sawa, Takashi Fujimoto, Tomoya Machinami, and Akira Ono. Mercuryii-mediated formation of thymine-hgii-thymine base pairs in dna duplexes. *Journal of the American Chemical Society*, 128(7):2172–2173, 2006. doi: 10.1021/ja056354d.

Michael Mozurkewich. Mechanisms for the release of halogens from sea-salt particles by free radical reactions. *Journal of Geophysical Research: Atmospheres*, 100(D7):14199–14207, 1995.

J Munthe, F Sprovieri, M Horvat, and R Ebinghaus. *SOPs and QA/QC protocols regarding measurements of TGM, GEM, RGM, TPM and mercury in precipitation in cooperation with WP3, WP4 and WP5.* GMOS deliverable 6.1, CNR-IIA, IVL, 2011.

José A Naranjo and Charles R Stern. Holocene tephrochronology of the southernmost part (42 30'-45 s) of the andean southern volcanic zone. *Revista geológica de Chile*, 31(2):224–240, 2004.

Xiangheng Niu, Yili Ding, Chen Chen, Hongli Zhao, and Minbo Lan. A novel electrochemical biosensor for hg 2+ determination based on hg 2+-induced dna hybridization. *Sensors and Actuators B: Chemical*, 158(1):383–387, 2011.

Jerome Nriagu and Christian Becker. Volcanic emissions of mercury to the atmosphere: global and regional inventories. *Science of the Total Environment*, 304(1):3–12, 2003.

Jerome O Nriagu, Jozef M Pacyna, et al. Quantitative assessment of worldwide contamination of air, water and soils by trace metals. *Nature*, 333(6169):134–139, 1988.

Daniel Obrist, Hans Moosmüller, Roger Schürmann, L-W Antony Chen, and Sonia M Kreidenweis. Particulate-phase and gaseous elemental mercury emissions during biomass combustion: controlling factors and correlation with particulate matter emissions. *Environmental science & technology*, 42(3):721–727, 2007.

Daniel Obrist, Eran Tas, Mordechai Peleg, Valeri Matveev, Xavier Faïn, David Asaf, and Menachem Luria. Bromine-induced oxidation of mercury in the mid-latitude atmosphere. *Nature Geoscience*, 4 (1):22–26, 2011.

Biswajit Pal and Parisa A Ariya. Gas-phase ho^* -initiated reactions of elemental mercury: Kinetics, product studies, and atmospheric implications. *Environmental science & technology*, 38(21):5555–5566, 2004.

European Parliament and of the Council. Directive 2008/50/ce of the european parliament and of the council of 21 may 2008 on ambient air quality and cleaner air for europe, 2008.

José M Paruelo, Adriana Beltran, Esteban Jobbagy, Osvaldo E Sala, and Rodolfo A Golluscio. The climate of patagonia: general patterns and controls on biotic processes. *Ecología Austral*, 8(2):85–101, 1998.

N Pirrone, P Costa, JM Pacyna, and R Ferrara. Mercury emissions to the atmosphere from natural and anthropogenic sources in the mediterranean region. *Atmospheric Environment*, 35(17):2997–3006, 2001.

N Pirrone, R Ferrara, IM Hedgecock, G Kallos, Y Mamane, J Munthe, JM Pacyna, I Pytharoulis, F Sprovieri, A Voudouri, et al. Dynamic processes of mercury over the mediterranean region: results from the mediterranean atmospheric mercury cycle system (mamcs) project. *Atmospheric Environment*, 37:21–39, 2003.

Nicola Pirrone and Kathryn R Mahaffey. *Dynamics of mercury pollution on regional and global scales: atmospheric processes and human exposures around the world*. Springer Science & Business Media, 2005.

Nicola Pirrone, Gerald J Keeler, and Jerome O Nriagu. Regional differences in worldwide emissions of mercury to the atmosphere. *Atmospheric Environment*, 30(17):2981–2987, 1996.

Nicola Pirrone, Ivo Allegrini, Gerald J Keeler, Jerome O Nriagu, Ronald Rossmann, and John A Robbins. Historical atmospheric mercury emissions and depositions in north america compared to

mercury accumulations in sedimentary records. *Atmospheric Environment*, 32(5):929–940, 1998.

Nicola Pirrone, Sergio Cinnirella, Xinbin Feng, Robert B Finkelman, Hans R Friedli, Joy Leaner, Rob Mason, Arun B Mukherjee, Glenn Stracher, David G Streets, et al. Global mercury emissions to the atmosphere from natural and anthropogenic sources. In *Mercury fate and transport in the global atmosphere*, pages 1–47. Springer, 2009.

David M Pyle and Tamsin A Mather. The importance of volcanic emissions for the global atmospheric mercury cycle. *Atmospheric Environment*, 37(36):5115–5124, 2003.

GV Ramesh and TP Radhakrishnan. A universal sensor for mercury (hg, hgi, hgii) based on silver nanoparticle-embedded polymer thin film. *ACS applied materials & interfaces*, 3(4):988–994, 2011.

Katie A Read, Anoop S Mahajan, Lucy J Carpenter, Mathew J Evans, Bruno VE Faria, Dwayne E Heard, James R Hopkins, James D Lee, Sarah J Moller, Alastair C Lewis, et al. Extensive halogen-mediated ozone destruction over the tropical atlantic ocean. *Nature*, 453(7199):1232–1235, 2008.

S Ribeiro Guevara, Markus Meili, A Rizzo, R Daga, and M Arribére. Sediment records of highly variable mercury inputs to mountain lakes in patagonia during the past millennium. *Atmospheric Chemistry and Physics*, 10(7):3443–3453, 2010.

A Rizzo, M Arcagni, MA Arribére, D Bubach, and S Ribeiro Guevara. Mercury in the biotic compartments of northwest patagonia lakes, argentina. *Chemosphere*, 84(1):70–79, 2011.

Andrea Rizzo, Marina Arcagni, Linda Campbell, Neža Koron, Majda Pavlin, María A Arribére, Milena Horvat, and Sergio Ribeiro Guevara. Source and trophic transfer of mercury in plankton from an

ultraoligotrophic lacustrine system (lake nahuel huapi, north patagonia). *Ecotoxicology*, 23(7):1184–1194, 2014.

Matilde Rusticucci, Natalia Zazulie, and Graciela B Raga. Regional winter climate of the southern central andes: Assessing the performance of era-interim for climate studies. *Journal of Geophysical Research: Atmospheres*, 119(14):8568–8582, 2014.

Isao Sanemasa. The solubility of elemental mercury vapor in water. *Bulletin of the Chemical Society of Japan*, 48(6):1795–1798, 1975.

William H Schroeder and John Munthe. Atmospheric mercury an overview. *Atmospheric Environment*, 32(5):809–822, 1998.

William H Schroeder, Greg Yarwood, and Hiromi Niki. Transformation processes involving mercury species in the atmosphere-results from a literature survey. *Water, Air, & Soil Pollution*, 56(1):653–666, 1991.

Paul F Schuster, David P Krabbenhoft, David L Naftz, L Dewayne Cecil, Mark L Olson, John F Dewild, David D Susong, Jaromy R Green, and Micheal L Abbott. Atmospheric mercury deposition during the last 270 years: a glacial ice core record of natural and anthropogenic sources. *Environmental Science & Technology*, 36 (11):2303–2310, 2002.

Christian Seigneur, Jacek Wrobel, and Elpida Constantinou. A chemical kinetic mechanism for atmospheric inorganic mercury. *Environmental science & technology*, 28(9):1589–1597, 1994.

Christian Seigneur, Krish Vijayaraghavan, and Kristen Lohman. Atmospheric mercury chemistry: Sensitivity of global model simulations to chemical reactions. *Journal of Geophysical Research: Atmospheres*, 111(D22), 2006.

Noelle E Selin. Global biogeochemical cycling of mercury: a review. *Annual Review of Environment and Resources*, 34, 2009.

David Simpson. Hydrocarbon reactivity and ozone formation in europe. *Journal of Atmospheric Chemistry*, 20(2):163–177, 1995.

Franz Slemr, Hélène Angot, Aurélien Dommergue, Olivier Magand, Manuel Barret, Andreas Weigelt, Ralf Ebinghaus, E-G Brunke, Katrine Aspmo Pfaffhuber, Grant Edwards, et al. Comparison of mercury concentrations measured at several sites in the southern hemisphere. *Atmospheric Chemistry and Physics*, 15(6):3125–3133, 2015.

Rebecca N Sliger, John C Kramlich, and Nick M Marinov. Towards the development of a chemical kinetic model for the homogeneous oxidation of mercury by chlorine species. *Fuel Processing Technology*, 65:423–438, 2000.

Anne L Soerensen, Henrik Skov, Daniel J Jacob, Britt T Soerensen, and Matthew S Johnson. Global concentrations of gaseous elemental mercury and reactive gaseous mercury in the marine boundary layer. *Environmental science & technology*, 44(19):7425–7430, 2010.

J Sommar, ME Andersson, and H-W Jacobi. Circumpolar measurements of speciated mercury, ozone and carbon monoxide in the boundary layer of the arctic ocean. *Atmospheric Chemistry and Physics*, 10(11):5031–5045, 2010.

Jonas Sommar, Mattias Hallquist, Evert Ljungström, and Oliver Lindqvist. On the gas phase reactions between volatile biogenic mercury species and the nitrate radical. *Journal of Atmospheric Chemistry*, 27(3):233–247, 1997.

Jonas Sommar, Katarina Gårdfeldt, Dan Strömberg, and Xinbin Feng. A kinetic study of the gas-phase reaction between the hydroxyl radical and atomic mercury. *Atmospheric Environment*, 35(17):3049–3054, 2001.

F Sprovieri, N Pirrone, K Gärdfeldt, and J Sommar. Mercury speciation in the marine boundary layer along a 6000km cruise path around the mediterranean sea. *Atmospheric Environment*, 37:63–71, 2003.

F Sprovieri, N Pirrone, MS Landis, and RK Stevens. Atmospheric mercury behavior at different altitudes at ny alesund during spring 2003. *Atmospheric Environment*, 39(39):7646–7656, 2005a.

F Sprovieri, IM Hedgecock, and N Pirrone. An investigation of the origins of reactive gaseous mercury in the mediterranean marine boundary layer. *Atmospheric Chemistry and Physics*, 10(8):3985–3997, 2010a.

F Sprovieri, N Pirrone, R Ebinghaus, H Kock, and A Dommergue. A review of worldwide atmospheric mercury measurements. *Atmospheric Chemistry and Physics*, 10(17):8245–8265, 2010b.

F Sprovieri, N Pirrone, M Bencardino, F D'Amore, H Angot, C Barbante, EG Brunke, F Arcega-Cabrera, W Cairns, S Comero, et al. Five-year records of total mercury deposition flux at gmos sites in the northern and southern hemispheres. *Atmos. Chem. Phys. Discuss., doi*, 10, 2016a.

Francesca Sprovieri and Nicola Pirrone. Spatial and temporal distribution of atmospheric mercury species over the adriatic sea. *Environmental Fluid Mechanics*, 8(2):117–128, 2008.

Francesca Sprovieri, Nicola Pirrone, Matthew S Landis, and Robert K Stevens. Oxidation of gaseous elemental mercury to gaseous divalent mercury during 2003 polar sunrise at ny-alesund. *Environmental science & technology*, 39(23):9156–9165, 2005b.

Francesca Sprovieri, Nicola Pirrone, Mariantonia Bencardino, Francesco D'Amore, Francesco Carbone, Sergio Cinnirella, Valentino Mannarino, Matthew Landis, Ralf Ebinghaus, Andreas Weigelt, et al. Atmospheric mercury concentrations observed at ground-based monitoring sites globally distributed in the framework of the gmos network. *Atmospheric Chemistry and Physics*, 16(18): 11915–11935, 2016b.

Alexandra Steffen, Tina Scherz, Mark Olson, David Gay, and Pierrette Blanchard. A comparison of data quality control protocols for atmospheric mercury speciation measurements. *Journal of Environmental Monitoring*, 14(3):752–765, 2012.

Joseph JS Tokos, Bjorn Hall, Julie A Calhoun, and Eric M Prestbo. Homogeneous gas-phase reaction of hg with h2o2, 03, ch3i, and (ch3) 2s: Implications for atmospheric hg cycling. *Atmospheric Environment*, 32(5):823–827, 1998.

JA Tossell. Calculation of the energetics for oxidation of gas-phase elemental hg by br and bro. *The Journal of physical chemistry A*, 107(39):7804–7808, 2003.

Oleg Travnikov, Hélène Angot, Paulo Artaxo, Mariantonia Bencardino, Johannes Bieser, Francesco D'Amore, Ashu Dastoor, Francesco De Simone, María del Carmen Diéguez, Aurélien Dommergue, et al. Multi-model study of mercury dispersion in the atmosphere: Atmospheric processes and model evaluation. *Atmospheric Chemistry and Physics*, 17(8):5271, 2017.

Lisa Van Loon, Elizabeth Mader, and Susannah L Scott. Reduction of the aqueous mercuric ion by sulfite: Uv spectrum of hgso3 and its intramolecular redox reaction. *The Journal of Physical Chemistry A*, 104(8):1621–1626, 2000.

Walter Vastarella, Livia Della Seta, Amedeo Masci, Jan Maly, Manuela De Leo, Ligia Maria Moretto, and Roberto Pilloton. Biosensors based on gold nanoelectrode ensembles and screen printed electrodes. *International Journal of Environmental and Analytical Chemistry*, 87(10-11):701–714, 2007.

K Velchev, F Cavalli, J Hjorth, E Marmer, E Vignati, F Dentener, and F Raes. Ozone over the western mediterranean sea–results from two years of shipborne measurements. *Atmospheric Chemistry and Physics*, 11(2):675–688, 2011.

Rainer Vogt, Paul J. Crutzen, and Rolf Sander. *A Mechanism for Halogen Release from Sea-Salt Aerosol in the Remote Marine Boundary Layer*, pages 189–196. Springer International Publishing, Cham, 2016. ISBN 978-3-319-27460-7. doi: 10.1007/978-3-319-27460-7_8. URL http://dx.doi.org/10.1007/978-3-319-27460-7_8.

Andreas Volz-Thomas, Matthias Beekmann, Dick Derwent, Kathy Law, Anne Lindskog, André Prévôt, Michiel Roemer, Martin Schultz, Ulrich Schurath, Sverre Solberg, et al. Tropospheric ozone and its control. *Towards Cleaner Air for Europe–Science, Tools and Applications. Part*, 1:73–122, 2003.

Roland von Glasow. Atmospheric chemistry in volcanic plumes. *Proceedings of the National Academy of Sciences*, 107(15):6594–6599, 2010.

Roland von Glasow, Rolf Sander, Andreas Bott, and Paul J Crutzen. Modeling halogen chemistry in the marine boundary layer 1. cloud-free mbl. *Journal of Geophysical Research: Atmospheres*, 107(D17), 2002.

Chunjie Wang, Zhijia Ci, Zhangwei Wang, Xiaoshan Zhang, and Jia Guo. Speciated atmospheric mercury in the marine boundary layer of the bohai sea and yellow sea. *Atmospheric Environment*, 131: 360–370, 2016.

Guang-Li Wang, Xiao-Ying Zhu, Huan-Jun Jiao, Yu-Ming Dong, and Zai-Jun Li. Ultrasensitive and dual functional colorimetric sensors for mercury (ii) ions and hydrogen peroxide based on catalytic reduction property of silver nanoparticles. *Biosensors and Bioelectronics*, 31(1):337–342, 2012.

I Wängberg, J Munthe, N Pirrone, Å Iverfeldt, E Bahlman, P Costa, R Ebinghaus, X Feng, R Ferrara, K Gårdfeldt, et al. Atmospheric mercury distribution in northern europe and in the mediterranean region. *Atmospheric Environment*, 35(17):3019–3025, 2001.

Peter Warneck. *Chemistry of the natural atmosphere*, volume 71. Academic press, 1999.

Peter Weiss-Penzias, Daniel A Jaffe, Anna McClintick, Eric M Prestbo, and Matthew S Landis. Gaseous elemental mercury in the marine boundary layer: Evidence for rapid removal in anthropogenic pollution. *Environmental science & technology*, 37(17):3755–3763, 2003.

Danhong Wu, Qing Zhang, Xia Chu, Haibo Wang, Guoli Shen, and Ruqin Yu. Ultrasensitive electrochemical sensor for mercury (ii) based on target-induced structure-switching dna. *Biosensors and Bioelectronics*, 25(5):1025–1031, 2010.